

# Simulation of the $^{83\text{m}}\text{Kr}$ Mode of the Tritium Source of the KATRIN Experiment

Master's thesis of

Moritz Machatschek

at the Department of Physics  
Institute of Experimental Nuclear Physics (IEKP)

Reviewer: Prof. Dr. Guido Drexlin  
Second reviewer: Prof. Dr. Ulrich Husemann  
Advisor: Dr. Kathrin Valerius  
Second advisor: Dr. Marco Kleesiek  
Third advisor: M.Sc. Hendrik Seitz-Moskaliuk

01. May 2015 – 12. May 2016

Karlsruher Institut für Technologie  
Fakultät für Physik  
Institut für Experimentelle Kernphysik (IEKP)  
Hermann-von-Helmholtz-Platz 1  
76344 Eggenstein-Leopoldshafen

---

I declare that I have developed and written the enclosed thesis completely by myself, and have not used sources or means without declaration in the text.

**PLACE, DATE**

.....  
(Moritz Machatschek)



# Introduction

The topic of this thesis is the simulation of the  $^{83\text{m}}\text{Kr}$  mode of the tritium source of the KARlsruhe TRItium Neutrino (KATRIN) experiment, which will be used for the studying of critical systematic effects.

The KATRIN experiment, currently in its final construction and commissioning phase, will perform a kinematic measurement of the electron neutrino mass  $m_{\nu_e}$  by precision spectroscopy of the tritium  $\beta$  decay spectrum at its kinematic endpoint with an energy of 18.6 keV. KATRIN aims to reach an unprecedented sensitivity of 200 meV (90 % C. L.) [KAT04], which can be accomplished using a high luminosity tritium source and a large scale spectrometer of the MAC-E filter type, while keeping stringent limits on the systematic uncertainty budget.

To reduce systematic effects while providing high luminosity KATRIN will use a Windowless Gaseous Tritium Source WGTS, in which the tritium gas gets continuously cycled. One of the major possible sources of systematic errors is the energy calibration of the experiment, requiring a 60 meV precision of the potential difference of main spectrometer and tritium source. The absolute potential of the tritium source is strongly influenced by the radioactive decay of the tritium, which entails the formation of a low density plasma. It is expected, that the mean of the plasma potential is related to a shift of the measured tritium endpoint, whereas the inhomogeneity of the plasma potential produces a Gaussian fluctuation  $\sigma_\beta$  in the electron spectrum, ultimately leading to a neutrino mass shift of [RK88]

$$\Delta m_\nu^2 = -2\sigma_\beta^2 . \quad (1)$$

For the studying of the plasma effects the usage of the  $^{83\text{m}}\text{Kr}$  mode of the gaseous tritium source is proposed. Mesomeric krypton-83m exhibits several mono-energetic electron conversion lines in the favourable KATRIN energy range, it is gaseous at feasible KATRIN conditions and it can therefore be dispersed along with the tritium gas inside the tritium source. It is expected that the influence of the plasma potential on the krypton-83m conversion electron spectrum and the  $\beta$  spectrum is very much comparable. In particular, an energy shift of the krypton-83m conversion electron spectrum should be related to the mean plasma potential and a broadening  $\sigma_g$  of the krypton-83m conversion electron lines to the plasma potential inhomogeneity. Thus, it is planned to use the estimate for  $\sigma_g$  obtained in  $^{83\text{m}}\text{Kr}$  mode measurements to quantify the plasma potential induced neutrino mass shift, a procedure which has successfully been used by the predecessor Troitsk Neutrino-Mass Experiment [Bel+08].

Furthermore, previous works have shown, that in principle an approximated model for the shape of the plasma potential is obtainable out of  $^{83\text{m}}\text{Kr}$  mode measurements [Hua10].

This information on the shape of the potential could even be used to correct the plasma potential induced neutrino mass shift.

Consequently, it is the subject of this thesis to embed a comprehensive simulation model of the  $^{83\text{m}}\text{Kr}$  mode into the KATRIN simulation framework and to use this model to predict the sensitivity of KATRIN  $^{83\text{m}}\text{Kr}$  mode measurements on the coefficients of different models of the plasma potential.

This thesis is divided into four chapters:

In chapter 1 a brief introduction to neutrino physics is given. It covers the history of the discovery of the neutrino, as well as the experimental evidence that neutrinos have a non-vanishing mass.

Chapter 2 gives a short overview of the KATRIN experiment, which aims to measure the neutrino mass with unprecedented sensitivity. The basic components of the experiment as well as its comprehensive analysis and simulation framework is explained.

In chapter 3 follows a detailed discussion of the KATRIN  $^{83\text{m}}\text{Kr}$  mode. It covers the operational parameters in  $^{83\text{m}}\text{Kr}$  mode, as well as the enhancements of the KATRIN software framework, which are necessary to simulate the  $^{83\text{m}}\text{Kr}$  mode measurements.

Finally, in chapter 4 the sensitivity studies on the coefficients of different plasma potential models are presented. The chapter starts with a detailed discussion on the chosen input parameters for the simulation studies. Furthermore, the relevant physical processes concerning the sensitivity of  $^{83\text{m}}\text{Kr}$  mode measurements are explained. This is followed by the presentation of the simulation results and a comprehensive discussion. Based on this discussion, the chapter is concluded with concrete recommendations for  $^{83\text{m}}\text{Kr}$  mode measurements.

The thesis ends with a summary and an outlook on possible, reasonable enhancements of the  $^{83\text{m}}\text{Kr}$  mode simulation, which are based on the findings of this work.

# Contents

<b>Introduction</b>	<b>i</b>
<b>1. Neutrino Physics</b>	<b>1</b>
1.1. The Discovery of Neutrinos . . . . .	1
1.2. Massive Neutrinos - Neutrino Oscillations . . . . .	3
1.3. Complementary Methods for Determining the Neutrino Mass . . . . .	6
1.3.1. Neutrino Mass Limits from Cosmology . . . . .	7
1.3.2. Neutrino Mass Limits from Neutrinoless Double Beta Decay . . . . .	8
1.3.3. Neutrino Mass Limits from Single Beta Decay . . . . .	10
<b>2. The KARlsruhe TRItium Neutrino Experiment KATRIN</b>	<b>13</b>
2.1. Measurement Principle and Setup . . . . .	13
2.2. Neutrino Mass Analysis with KATRIN . . . . .	22
2.2.1. $\chi^2$ Analysis with KATRIN . . . . .	22
2.2.2. Spectrum Simulation . . . . .	24
2.2.3. Sensitivity of KATRIN on the Neutrino Mass . . . . .	28
<b>3. <math>^{83m}\text{Kr}</math> Mode of the Windowless Gaseous Tritium Source for Investigation of Systematics</b>	<b>31</b>
3.1. Operational Parameters of the Gaseous Source in $^{83m}\text{Kr}$ Mode . . . . .	32
3.2. Modelling and Implementation . . . . .	34
3.2.1. $^{83m}\text{Kr}$ Conversion Electron Spectrum . . . . .	34
3.2.2. $^{83m}\text{Kr}$ Gas Dynamics . . . . .	41
3.3. Systematic Studies with the $^{83m}\text{Kr}$ Mode . . . . .	45
<b>4. Simulation Studies of the <math>^{83m}\text{Kr}</math>-Mode Sensitivity on the Tritium Source Plasma Potential</b>	<b>49</b>
4.1. Discussion of the Source Plasma Potential and its Modelling . . . . .	50
4.1.1. Voigt Profile of the $^{83m}\text{Kr}$ Conversion Electron Lines . . . . .	51
4.1.2. Ellipse Potential Model . . . . .	54
4.1.3. Polynomial Potential Model . . . . .	55
4.2. Input Parameters for the Simulation Studies . . . . .	57
4.2.1. The Inelastic Scattering Cross Section . . . . .	57
4.2.2. Influence of the Tritium Column Density on $^{83m}\text{Kr}$ -Mode Studies . . . . .	58
4.2.3. The Amount of $^{83m}\text{Kr}$ inside the Source . . . . .	60
4.2.4. Measured Conversion Lines and Measurement Time Distribution . . . . .	62
4.3. Sensitivity on Axial Effects in the WGTS in the Presence of Inelastic Scattering . . . . .	66
4.4. Statistical Sensitivities of the Parameters of Different Potential Models . . . . .	69

4.5. Systematic Uncertainties . . . . .	77
4.5.1. Uncertainty of the WGTS Cryostat Temperature . . . . .	77
4.5.2. Uncertainty of the Inelastic Cross Section . . . . .	79
4.6. Discussion . . . . .	81
4.6.1. Impact of Inelastic Scattering on Krypton-83m Measurements . .	84
4.6.2. Minimal Scattering Potential Model . . . . .	85
4.6.3. Impact on Neutrino Mass Analysis . . . . .	91
4.7. Recommendations for $^{83\text{m}}\text{Kr}$ Mode Measurements . . . . .	93
<b>5. Conclusion and Outlook</b>	<b>95</b>
<b>Bibliography</b>	<b>97</b>
<b>A. Appendix</b>	<b>103</b>
A.1. Shape Deformation of Lorentzian Lines with the WGTS Plasma Potential	103
A.2. Towards an Optimised Measurement Time Distribution in Krypton-83m Mode . . . . .	103

# List of Figures

1.1.	Theory of $\beta$ decay . . . . .	2
1.2.	Standard Model (SM) of particle physics . . . . .	3
1.3.	Limits on the sum of the neutrino mass eigenstates from cosmology . . . . .	8
1.4.	Feynman diagram of $0\nu\beta\beta$ decay . . . . .	9
1.5.	Spectra of $2\nu\beta\beta$ and $0\nu\beta\beta$ decay . . . . .	10
1.6.	Tritium Beta Spectrum . . . . .	11
2.1.	The experimental setup of KATRIN . . . . .	14
2.2.	Working principle of the MAC-E filter . . . . .	15
2.3.	Windowless Gaseous Tritium Source . . . . .	18
2.4.	Differential and cryogenic pumping section . . . . .	19
2.5.	Focal plane detector system . . . . .	20
2.6.	Structure of the KATRIN analysis tool KaFit . . . . .	25
2.7.	Mapping of source regions to the detector and voxelisation . . . . .	26
2.8.	Energy loss function, describing the inelastic energy loss of electrons due to scattering on tritium molecules . . . . .	27
2.9.	Response function for nominal KATRIN conditions . . . . .	27
2.10.	Sensitivity on $m_\nu$ as a function of the total measurement time for different MTDs . . . . .	29
3.1.	Creation of the $^{83\text{m}}\text{Kr}$ isomer and its deexcitation . . . . .	35
3.2.	Differential krypton-83m conversion electron spectrum . . . . .	39
3.3.	Integrated krypton-83m conversion electron spectrum . . . . .	40
3.4.	Close-up on a region of interest around the integrated krypton-83m $L_2$ and $L_3$ conversion electron lines . . . . .	40
3.5.	Tritium and krypton gas profiles for $T = 110$ K . . . . .	42
3.6.	Tritium and krypton bulk velocity profiles for $T = 110$ K . . . . .	43
3.7.	Relative column density deviation of krypton in radial direction . . . . .	44
3.8.	Plasma formation inside the WGTS . . . . .	45
3.9.	Simulated plasma potential inside the WGTS for 30 K . . . . .	46
3.10.	Simulated $z$ -profile of the central plasma potential inside the WGTS for 30 K and 110 K . . . . .	48
3.11.	Effect of the WGTS plasma potential on the krypton-83m $L_3$ line . . . . .	48
4.1.	Effect of a Gaussian broadening of the krypton-83m $L_3$ conversion line with standard deviation $\sigma_g$ . . . . .	52
4.2.	Shift of the krypton-83m $L_3$ conversion line with $E_{\text{shift}}$ . . . . .	52
4.3.	Fit of the 110 K plasma potential simulation with a single mean $V_0$ . . . . .	53

4.4.	Fit of the 110 K plasma potential simulation with the 6 parameter ellipse model . . . . .	55
4.5.	Fit of the 110 K plasma potential simulation with independent means for rear and front part . . . . .	56
4.6.	Linear fit of the 110 K plasma potential simulation . . . . .	56
4.7.	Krypton-83m $K$ conversion line measured on a tritium $\beta$ background . .	58
4.8.	Integrated rate on the plateau of unscattered electrons of the krypton-83m $L_3$ conversion line . . . . .	60
4.9.	Retarding potentials in different MTDs for the $L_3$ conversion line . . . .	64
4.10.	Scattering probabilities for nominal column density . . . . .	68
4.11.	Scattering probabilities for reduced column density . . . . .	68
4.12.	Two dimensional negative log-likelihood of the linear model . . . . .	70
4.13.	Voigt profile: statistical sensitivities - $L_3$ - 110 K potential . . . . .	72
4.14.	Voigt profile: statistical sensitivities - $L_3$ - vanishing potential . . . . .	73
4.15.	Voigt profile: statistical sensitivities - $L_3$ - 110 K potential - reduced column density . . . . .	74
4.16.	Rectangular model: statistical sensitivities - $L_3$ - 110 K potential . . . . .	75
4.17.	Linear model: statistical sensitivities - $L_3$ - 110 K potential . . . . .	76
4.18.	Systematic shift of the Gaussian broadening parameter $\sigma_g$ with an uncertainty in the temperature of the WGTS cryostat . . . . .	78
4.19.	Sensitivity of the rectangular model with inelastic cross section as additional free parameter . . . . .	80
4.20.	Response as function of the surplus energy $E - qU$ for the retarding potential of $U = 30475$ kV and MSPM approximation . . . . .	86
4.21.	Weighted 110 K plasma potential . . . . .	88
A.1.	Shape deformation of Lorentzian lines . . . . .	104
A.2.	Plasma potential induced deviation of integrated $L_3$ rates . . . . .	104

# List of Tables

1.1. Neutrino mixing parameters . . . . .	7
2.1. KATRIN systematic uncertainties. . . . .	28
3.1. WGTS krypton-83m and tritium mode parameters. . . . .	33
3.2. $^{83\text{m}}\text{Kr}$ conversion spectrum - main lines . . . . .	37
3.3. $^{83\text{m}}\text{Kr}$ conversion spectrum - effective satellite lines . . . . .	37
4.1. Ellipse model: table of simulation parameters. . . . .	54
4.2. Simulation parameters and their corresponding ranges . . . . .	57
4.3. Signal to Noise Ratio for the krypton-83m conversion lines in the $E \approx 30$ keV range . . . . .	63
4.4. Signal to Noise Ratio of the krypton-83m $K$ conversion line for different tritium column densities . . . . .	63
4.5. $z$ -averaged scattering probabilities for electrons in the 30 keV range . . . . .	66
4.6. Voigt profile: statistical sensitivities - $L_3$ - 110 K potential . . . . .	72
4.7. Voigt profile: statistical sensitivities - $L_3$ - vanishing potential . . . . .	73
4.8. Voigt profile: statistical sensitivities - $L_3$ - 110 K potential - reduced column density . . . . .	74
4.9. Rectangular model: statistical sensitivities - $L_3$ - 110 K potential . . . . .	75
4.10. Linear model: statistical sensitivities - $L_3$ - 110 K potential . . . . .	76
4.11. Potential model parameter estimates and true values for the 110 K plasma potential simulation . . . . .	83
4.12. Voigt profile parameter estimates and true values for the 110 K plasma potential simulation . . . . .	83
4.13. Measurable mean and standard deviation of the 110 K plasma potential. . . . .	89
4.14. Measurable parameter estimates of the potential models . . . . .	90
4.15. Means and standard deviations of the plasma simulation, simulated at 30 K, for different weights . . . . .	92
4.16. Total measurement time - 10 mV sensitivity - rectangular model . . . . .	93
4.17. Total measurement time - 30 mV sensitivity - rectangular model . . . . .	93



# 1. Neutrino Physics

In this chapter a brief introduction to neutrino physics is given. Section 1.1 provides a short summary on the discovery of the three neutrino flavours known today. In section 1.2 neutrino oscillations are discussed, which provide an evidence, that neutrinos are not massless. Finally, in section 1.3 complimentary methods for determining the neutrino mass are presented.

## 1.1. The Discovery of Neutrinos

A natural starting point for neutrino physics history are the intense studies of radioactive decays around the end of the 19th century. In 1914 Chadwick observed a continuous energy spectrum of electrons emitted in  $\beta$  decay [Cha14], which tightened the deficits in the theoretical understanding of this process. Since at this time only two decay products (an electron/positron and the daughter nucleus) could be measured, the  $\beta$  decay was believed to be a two body problem. Consequently, due to energy momentum conservation a monochromatic fermion energy was expected. In addition, the perception of  $\beta$  decay as a two body problem also violates the conservation of angular momentum, since the spin-statistics of mother and daughter atom was measured to be equal.

With his postulation of the neutrino in 1930 Pauli could resolve both problems [Pau30]. As this particle never had been observed, Pauli claimed it to be neutral and named it neutron. Two years later a heavier, neutral particle, today's neutron, was discovered by Chadwick [Cha32]. As a result Pauli's particle was called neutrino, a name introduced by Enrico Fermi, who also gave the first theory of  $\beta$  decay [Fer34].

### Fermi theory of $\beta$ decay in 1933

Fermi's theory essentially involves the neutrino. He introduced a point like interaction of the four particles participating in  $\beta$  decay, which enabled him to give the first theoretical explanation of the continuous  $\beta$  spectrum. This theory is still valid today in a low energy limit, when the inner structure of the vertex and the hadrons can not be observed (figure 1.1).

However, it took another 23 years, only 2 years before Pauli's death, until neutrinos were finally proved to exist in the Savannah River Experiment [Cow+56].

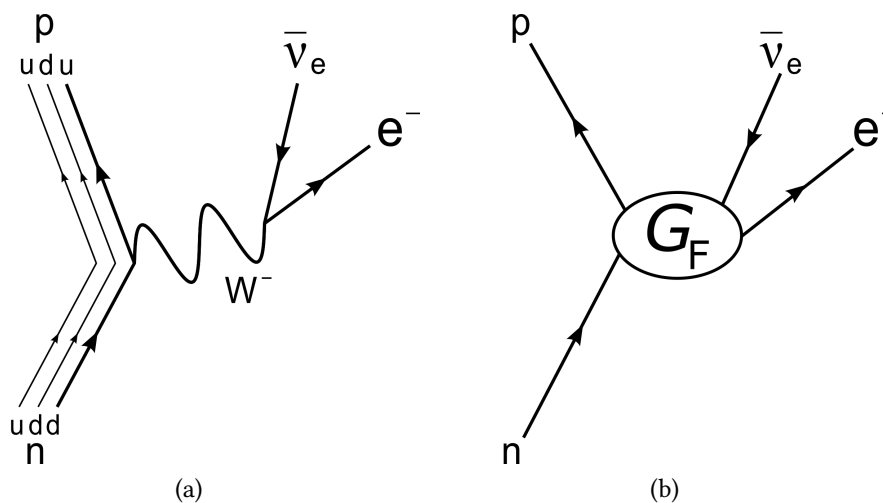


Figure 1.1.: Theory of  $\beta$  decay, here  $\beta^-$ , in today's theory of weak interaction. a) A neutron (n) changes into a proton (p) due to the conversion of a down quark (d) into an up quark (u). Thereby a  $W^-$  boson gets emitted, which decays into an electron ( $e^-$ ) and an electron antineutrino ( $\bar{\nu}_e$ ). In Fermi theory b), the interaction is described as point-like, with proton, neutron, neutrino and electron interacting in one vertex in time and place. The substructure of this vertex is condensed into a phenomenological coupling constant, the Fermi constant  $G_F$ .

### The Savannah River Experiment

In 1956 a team around C.L. Cowan and F. Reines succeeded in proving a neutrino-induced reaction, the inverse  $\beta$  decay

$$\bar{\nu}_e + p \rightarrow e^+ + n . \quad (1.1)$$

To maximise the signal, their experiment was built close to a nuclear power plant at Savannah River Cite, which produced a great deal of electron antineutrinos. For the detection they used two chambers of an aqueous solution of cadmium chloride ( $\text{CdCl}_2$ ), accompanied by three liquid scintillators and photo multipliers to measure a coincidence signal of two photons. The latter provides a strong reduction of background events.

Since the hydrogen in water provides weak bound protons, it is an optimal candidate to start the above reaction. The thereby created positron will quickly annihilate with an electron into two characteristic photons with the energy  $E_\gamma = m_e = 511 \text{ keV}$ . In the timespan of a few  $\mu\text{s}$  after that, the neutron will be moderated by interactions with the water, thus being captured by a cadmium nucleus. Thereby the nucleus will get excited, emitting the excitation energy by means of another photon, which then can be detected.

Considering the incoming antineutrino rate given by the power of the reactor and the handful of detected events, a cross section for this reaction of  $\sigma = 6.3 \cdot 10^{-44} \text{ cm}^2$  was obtained [Cow+56], which is in good agreement with Fermi's theory.

6 years after the proof of existence of the electron neutrino, evidence for another neutrino flavour, the muon neutrino  $\nu_\mu$ , was given at the Brookhaven National Laboratory [Dan+62].

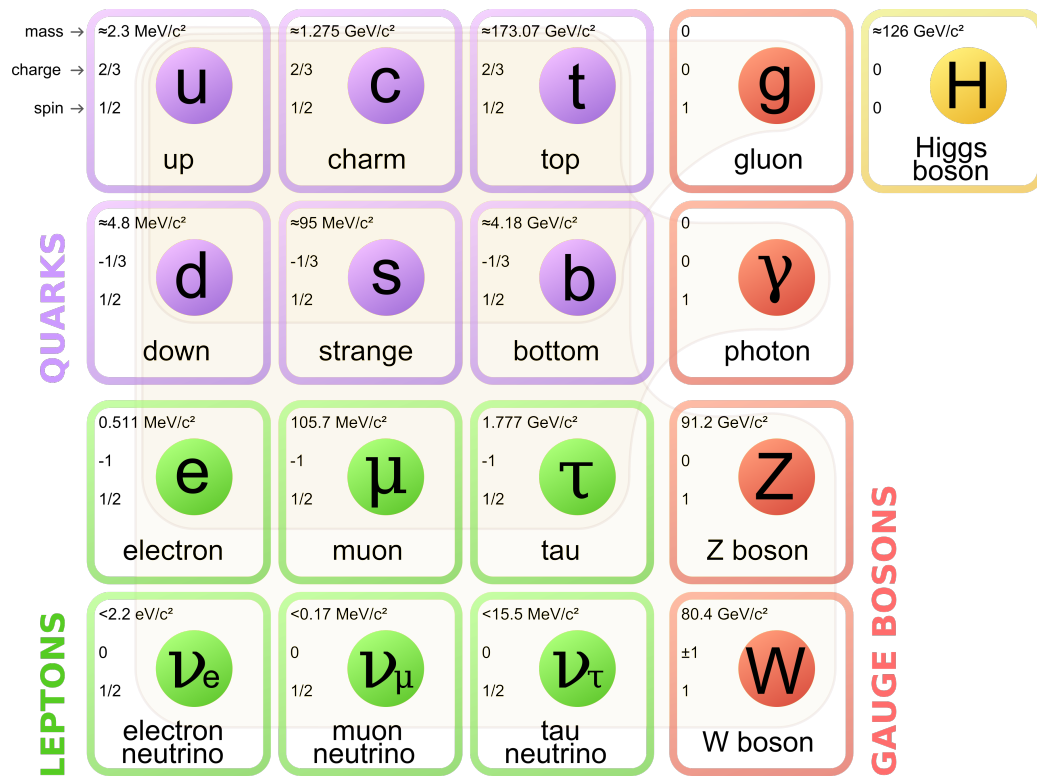


Figure 1.2.: Standard Model (SM) of particle physics: The SM comprises 17 particles, grouped in 12 fermions (violet and green) and 5 bosons (red and yellow). The fermions are additionally divided into quarks and leptons (taken from [Wik06]).

Yet another neutrino flavour was expected to exist, when the tau lepton was discovered in 1975. It took another 25 years until the tau neutrino  $\nu_\tau$  was observed at the DONUT experiment at the Fermi Lab [Kod+01].

By measuring the decay width  $\Gamma_{Z^0}$  of the  $Z^0$  boson at the Large Electron Positron Collider at CERN, the number of neutrino flavours is determined to  $N_\nu = 2.98 \pm 0.01$  [LG06], which holds for light neutrinos (for which  $2m_\nu < m_{Z^0} = 91 \text{ GeV}/c^2$ ) participating in weak interactions. This result is in perfect agreement with today's fundamental theory of particle physics, the Standard Model.

## 1.2. Massive Neutrinos - Neutrino Oscillations

The Standard Model provides a comprehensive theory of particles and particle interactions, giving the most precise theoretical predictions ever made in physics. A chart of its particles can be seen in figure 1.2.

In the time of its formulation no evidence for massive neutrinos existed and consequently the standard model was formulated with the assumption of a vanishing neutrino mass.

However, neutrino oscillation experiments in the 90's of the last century led to the conclusion, that this assumption is wrong.

## Neutrino Oscillations

In the Homestake experiment [Cle+98], a team around Raymond Davis aspired to confirm John Bahcall's theoretical prediction [Bah64] on the solar electron neutrino flux produced by hydrogen fusion inside the sun. The measurement required a low energy threshold, which could be achieved by counting of argon atoms produced in an inverse beta decay:



The argon atoms were extracted via helium bubbles out of more than 600 t perchloroethylene, purified and counted in a separate tank. For the latter an electron capture process to excited  ${}^{37}\text{Cl}^*$  was exploited, which produced a characteristic auger electron by deexcitation. After 24 years of measurement (1970-1994) this resulted in an average of  $\approx 0.5$  captured electron neutrinos per day, which can be translated to a solar neutrino flux of

$$\dot{N}_{\text{exp}} = (2.56 \pm 0.16 \pm 0.16) \text{ SNU} . \quad (1.3)$$

Here SNU denotes the solar neutrino unit, specifying the neutrino flux which leads to  $10^{-36}$  captures per target atom per second.

Compared to Bahcall's theoretical prediction, the result of the Homestake experiment was a factor 1/3 too low. The experiment was followed by others (Kamiokande, SAGE, GALLEX, Super Kamiokande [Suz95; Abd+94; Ham+99; Fuk+01]), neither of them falsifying Davis' measurement. The theory of the standard solar model was repeatedly checked but a discrepancy of 1/3 to 1/2 remained. It turned out, that no adjustment in the solar model could simultaneously explain the total neutrino flux and the measured energy spectrum. Hence, the solution of the solar neutrino problem was not an effect related to neutrino production, but to propagation. This was firstly introduced by B. Pontecorvo [GP69], who stated that neutrinos can change their flavour while propagation, thus introducing the concept of neutrino oscillations. However, a necessary requirement for the existence of neutrino oscillations is, that neutrinos have a non-vanishing mass.

The first experimental evidence for neutrino oscillations was given in the Sudbury Neutrino Observatory (SNO) experiment, which was able not only to measure electron neutrinos, but in addition the sum of all neutrino fluxes by the unique usage of 1000 t of heavy water [SNO+02]. In addition to charged-current (CC) reactions like in equation 1.2, this enables the detection of the following neutral-current (NC) reaction:



in which d labels the deuteron and  $\alpha \in \{e, \mu, \tau\}$  the neutrino flavour. The resulting free neutron will be captured, thereby ultimately producing fast electrons, which were detected through Cherenkov radiation. Thus, in 2001 the SNO collaboration published the following fluxes for the CC and NC reactions:

$$\begin{aligned} \phi_{\text{CC}}^{\text{SNO}} &= 1.76_{-0.05}^{+0.06}(\text{stat.})_{-0.09}^{+0.09}(\text{syst}) \cdot 10^6 \text{ cm}^{-2} \text{ s}^{-1} , \\ \phi_{\text{NC}}^{\text{SNO}} &= 5.09_{-0.43}^{+0.44}(\text{stat.})_{-0.43}^{+0.46}(\text{syst}) \cdot 10^6 \text{ cm}^{-2} \text{ s}^{-1} . \end{aligned} \quad (1.5)$$

This is in a perfect agreement with the expectation, that approximately only 1/3 of the total flux is contributed by electron neutrinos.

Meanwhile the existence of neutrino oscillations has been proven by a great many of experiments not only for solar neutrinos, but also for neutrinos produced in nuclear reactors and the atmosphere. Two of them, the SNO and the Super-Kamiokande Collaboration, were honoured with 2015th Nobel Prize of physics "for the discovery of neutrino oscillations, which shows that neutrinos have mass" [Nob15].

## Theory of Neutrino Oscillations

The key assumption for the theoretical explanation of neutrino oscillations is, that the flavour eigenstates  $|v_\alpha\rangle$  ( $\alpha \in \{e, \mu, \tau\}$ , i.e. the states of weak interaction) are not equal to the mass eigenstates  $|v_k\rangle$  ( $k \in \mathbb{N}$ , i.e. the states of propagation). Here, in general  $k$  can take values larger than 3, if sterile neutrinos<sup>1</sup> exist, mixing with the known flavours. Introducing a mixing matrix  $U$ , the different states can be linked via [Zub11]:

$$|v_\alpha(t)\rangle = \sum_k U_{\alpha k}^* e^{-iE_k^{\text{tot}}t} |v_k\rangle . \quad (1.6)$$

The phase factor  $e^{-iE_k^{\text{tot}}t}$  is obtained on the assumption, that the interaction length is much smaller than the length of free propagation, thus the time evolution is the one of a free particle<sup>2</sup>.

Since the phase velocity is given by the propagation states' energies  $E_k$ , the mixing will not stay constant in time, if the states obey different masses. Hence, mass is a necessary requirement for the existence of neutrino oscillations.

Deriving the probability  $P$  to detect a neutrino that was created in a flavour state  $\alpha$  in a flavour state  $\beta$  after propagating a distance  $L$  results in

$$\begin{aligned} P(v_\alpha \rightarrow v_\beta) &= |\langle v_\beta | v_\alpha(t) \rangle|^2 \\ &= \delta_{\alpha\beta} - 4 \sum_{k>j} \text{Re}(U_{\alpha k}^* U_{\beta k} U_{\alpha j} U_{\beta j}^*) \sin^2 \frac{\Delta m_{kj}^2 L}{4E} . \end{aligned} \quad (1.7)$$

For the sake of readability, charge particle CP invariance has been assumed, which leads to a real  $U$ .  $\Delta m_{kj}^2 = m_k^2 - m_j^2$  is the difference of the squared masses of the propagation states  $k, j$ . Therefore, oscillation experiments cannot probe absolute neutrino masses, but only mass differences.

In the case of  $k \leq 3$ ,  $U$  is called the Pontecorvo–Maki–Nakagawa–Sakata (PMNS) matrix. Due to its unitarity, it can be decomposed into three mixing angles  $\theta_{ij}$ , denoting the mixing

<sup>1</sup>Neutrinos, which do not participate in weak interaction, thus interacting only gravitationally. There are theoretical arguments in favour of an existence as well as experimental hints [Ham+11].

<sup>2</sup>This reasoning is not strictly true in the presence of very dense matter (like for example in the core of the sun), where additional effects can appear (i.e. the Mikhajlov–Smirnov–Wolfenstein-Effekt effect [Wil+88; MS86]). In general, finding the correct time evolution will involve quantum field theoretical methods.

between the mass states  $i, j$  and three phases  $\delta, \alpha_1, \alpha_2$ , such that it reads:

$$\begin{aligned}
 U = & \begin{pmatrix} 1 & 0 & 0 \\ 0 & \cos \theta_{23} & \sin \theta_{23} \\ 0 & -\sin \theta_{23} & \cos \theta_{23} \end{pmatrix} \times \begin{pmatrix} \cos \theta_{13} & 0 & \sin \theta_{13} \cdot e^{-i\delta} \\ 0 & 1 & 0 \\ -\sin \theta_{13} \cdot e^{-i\delta} & 0 & \cos \theta_{13} \end{pmatrix} \\
 & \times \begin{pmatrix} \cos \theta_{12} & \sin \theta_{12} & 0 \\ -\sin \theta_{12} & \cos \theta_{12} & 0 \\ 0 & 0 & 1 \end{pmatrix} \times \begin{pmatrix} 1 & 0 & 0 \\ 0 & e^{i\alpha_1} & 0 \\ 0 & 0 & e^{i\alpha_2} \end{pmatrix}
 \end{aligned} \tag{1.8}$$

Here  $\delta$  is often called a CP violating phase, and  $\alpha_1, \alpha_2$  denote Majorana phases.

This representation is particularly useful, since the oscillations are separated by their mass-difference scales, so that only the oscillation between two neutrino flavours can be taken into account in an approximate description. In this picture, the transition probability, for example in the case of  $\nu_\mu$ - $\nu_\tau$ -mixing, reads:

$$P(\nu_\mu \rightarrow \nu_\tau) = \sin^2 2\theta \sin^2 \frac{\Delta m_{23}^2 L}{4E} . \tag{1.9}$$

Hereby  $L_{\text{osc}} = \frac{4E}{\Delta m_{ij}^2}$  specifies the oscillation length.

Depending on the accessible length scales and energies variable experiments can be made to probe the mass differences and mixing angles, including atmospheric, accelerator, nuclear and solar neutrinos. The difference of the squared masses of  $m_1$  and  $m_2$  has been determined in experiments observing the oscillations of solar neutrinos.  $m_1^2 - m_3^2$  is known from atmospheric neutrino oscillation experiments. However, the hierarchy of the mass eigenvalues is not known.  $m_1 < m_2 < m_3$  is called the normal and  $m_3 < m_1 < m_2$  the inverted hierarchy. The latest results of a combined analysis are shown in table 1.1, for both scenarios.

Since oscillation experiments cannot provide the absolute values of the mass eigenstates, different experimental approaches are necessary for setting the scale of the absolute neutrino mass.

### 1.3. Complementary Methods for Determining the Neutrino Mass

The existence of neutrino oscillations is an evidence for massive neutrinos. Hence, strong efforts in measuring the neutrino mass are made today and the most important in the respective field is presented in the next sections. However, the existence of neutrino oscillations also demands some attention on the definition of "the neutrino mass", since every laboratory experiment in this field will somehow exploit the weak interaction and thus be sensitive to a certain combination of mass eigenvalues and PMNS matrix elements. The decomposition of this observables into their primal parts relies on a combination of experimental results, while only the mixing angles in the PMNS matrix are known today, provided by oscillation experiments.

Table 1.1.: **Neutrino mixing parameters**

Combined values from a global  $3\nu$  oscillation analysis. The following definitions are used:  $\delta m^2 = m_2^2 - m_1^2$ ,  $\Delta m^2 = m_3^2 - (m_1^2 + m_2^2)/2$  for normal and  $\Delta m^2 = (m_1^2 + m_2^2)/2 - m_3^2$  for inverted hierarchy (from [Cap+16]).

Parameter	Hierarchy	Best fit	$3\sigma$ range
$\delta m^2/(10^{-5} \text{ eV}^2)$	Both	7.37	6.93-7.97
$\Delta m^2/(10^{-3} \text{ eV}^2)$	normal	2.50	2.37-2.63
	inverted	2.46	2.33-2.60
$\sin^2 \theta_{12}/10^{-1}$	Both	2.97	2.50-3.54
$\sin^2 \theta_{13}/10^{-2}$	normal	2.14	1.85-2.46
	inverted	2.18	1.86-2.48
$\sin^2 \theta_{23}/10^{-1}$	normal	4.37	3.79-6.16
	inverted	5.69	3.83-6.37
$\delta/\pi$	normal	1.35	0-2
	inverted	1.32	0-2

### 1.3.1. Neutrino Mass Limits from Cosmology

The state of the art theory in cosmology is the  $\Lambda$  *Concordance Dark Matter*  $\Lambda$ CDM model, in which  $\Lambda$  is the cosmological constant. Following the assumption of a mainly gravitationally driven cosmological evolution and consequently being based on Einstein's general theory of relativity, it is unrivalledly successful in describing four major cosmological observations [Per03]: first, the existence and the small anisotropy of the *Cosmic Microwave Background* CMB, second, the expansion of the universe and the corresponding observable redshift, third, the abundance of light elements and fourth, the formation of large scale structures (structures larger than galaxies).

Neutrinos can play an important role in the latter, since they can escape overdense regions due to their weak interaction, thereby washing out density contrasts. This is only possible for length scales smaller than the free-streaming length, which is in inverse proportion to their mass [Per03]. The basic ingredient in this process is the smallness of the weak interaction, resulting in a mainly gravitational impact of neutrinos. Consequently, the cosmological observable is the direct sum of the mass eigenstates:

$$m_{\text{cosm}} = \sum m_i . \quad (1.10)$$

In its basic form, the  $\Lambda$ CDM model uses a minimum of 6 free parameters, but it can be supplemented to give a detailed description of the observations of cosmological experiments. In particular, the Planck collaboration lists over 15 free parameters which can be fitted to their data, based on a precision measurement of the CMB anisotropy [Ade+14]. In the Planck base  $\Lambda$ CDM model the neutrino mass only enters as a fixed parameter of  $m_{\text{cosm}} \approx 0.06 \text{ eV}$  [Pla15]. In the Planck CMB data alone, this is a rather insignificant parameter, as long as it is below  $\approx 1.0 \text{ eV}$ . Only when combined with further cosmological studies, strict limits can be given, as can be seen in figure 1.3. However, the Planck collaboration

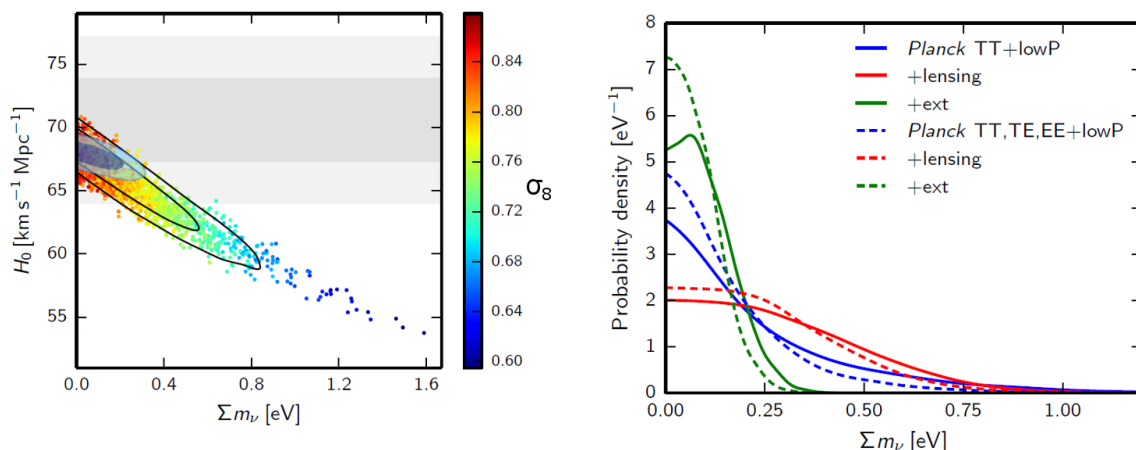


Figure 1.3.: Limits on the sum of the neutrino mass eigenstates from combinations of different cosmological studies: The plot on the left shows, that strong correlations can be present in cosmological studies, here between  $m_{\text{cosm}}$ , the Hubble constant  $H_0$  (range indicated by the grey, horizontal bars) and the matter fluctuation amplitude  $\sigma_8$ . As additional data is applied, some of the correlations can be broken and stricter limits can be obtained (contours and filled contours). The resulting probability densities for  $m_{\text{cosm}}$  can be seen on the right for different combinations of data (from [Pla15]).

itself lists several values for  $m_{\text{cosm}}$  in the range of 0.17 eV to 0.72 eV, since this procedure suffers from tension in the results of different cosmological studies.

Therefore, a neutrino mass limit from a laboratory experiment could break correlations in cosmological models and help to deduce better estimates for the remaining parameters.

### 1.3.2. Neutrino Mass Limits from Neutrinoless Double Beta Decay

Another possibility of providing information on the neutrino mass is the (hypothetical) neutrinoless double beta decay ( $0\nu\beta\beta$ ). The corresponding process can be seen in figure 1.4. It involves an exchange of a virtual neutrino, hence requires Majorana neutrinos (neutrinos which are their own antiparticle  $\nu = \bar{\nu}$ ) and does not conserve lepton number. Due to the latter it is forbidden in the Standard Model.

Since this process is of higher order, it is only expected with a very long half-life time ( $T_{1/2} > 10^{20}$  yr). Thus, detecting  $0\nu\beta\beta$  requires low background as well as large target masses. Furthermore, this implies that it is only measurable, when single beta decay is strongly suppressed. In any case, the possibility of two neutrino double beta decay ( $2\nu\beta\beta$ ) remains as background, which in a simple picture can be thought of as two simultaneous beta decays. Like in single beta decay, the electrons of  $2\nu\beta\beta$  will have a continuous energy spectrum. Since in  $0\nu\beta\beta$  only two electrons are emitted and the nucleus carries negligible energy, it is a two body decay. Hence, the  $0\nu\beta\beta$  decay would produce a discrete line at the endpoint of the  $2\nu\beta\beta$  spectrum, which is shown in figure 1.5.

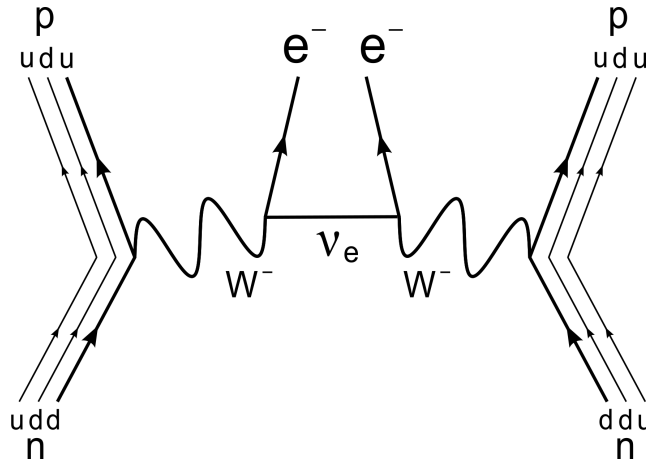


Figure 1.4.: Feynman diagram of  $0\nu\beta\beta$  decay: Two neutrons decay into two protons by creating two  $W^-$  bosons. They emit two electrons by exchange of a virtual Majorana neutrino.

$0\nu\beta\beta$  can provide information on the *effective Majorana mass*  $m_{\beta\beta}$  of the electron neutrino [GP12]:

$$\langle m_{\beta\beta} \rangle = \left| \sum_i U_{ei}^2 m_i \right| = \left| \sum_i e^{i\xi_i} |U_{ei}|^2 m_i \right|. \quad (1.11)$$

Here the  $U_{ei}$  can be identified with the electronic parts of the mixing matrix in equation 1.8. However, the Majorana phases  $\xi_i$  also have to be included here, but only two of them are physical. Correspondingly, the effective Majorana mass can provide additional information on the combination of the Majorana phases, but it might be smaller than the mass eigenvalues or the incoherent sum. Hence, it can only provide complimentary information on the mass in combination with the results from other experiments. However, in any case an important contribution of  $0\nu\beta\beta$  experiments is, that they might give evidence, that neutrinos are in fact Majorana particles.

In contrast to single beta decay or  $2\nu\beta\beta$ , in which the neutrino mass modifies the shape of the spectrum, the neutrino contributes directly to the vertex of  $0\nu\beta\beta$ , thus the effective mass enters in the rate (or half-life time) [Del+16]:

$$(T_{1/2}^{0\nu})^{-1} \propto \langle m_{\beta\beta} \rangle^2. \quad (1.12)$$

Correspondingly, the measurement strongly relies on the calculation of the proportionality constant, which involves the matrix element of the transition. This entailed major uncertainties in the last years (factors of 2-4).

There are several experiments trying to measure  $0\nu\beta\beta$  with different materials (the most sensitive at the moment use germanium-76, tellurium-130 or xenon-136), with typical sensitivities lying in the range of  $T_{1/2}^{0\nu} \propto 10^{25}$  yr. The best limits on the Majorana mass stem from xenon experiments, which give [Aug+12]

$$m_{\beta\beta} < 140 - 380 \text{ meV}, \quad (1.13)$$

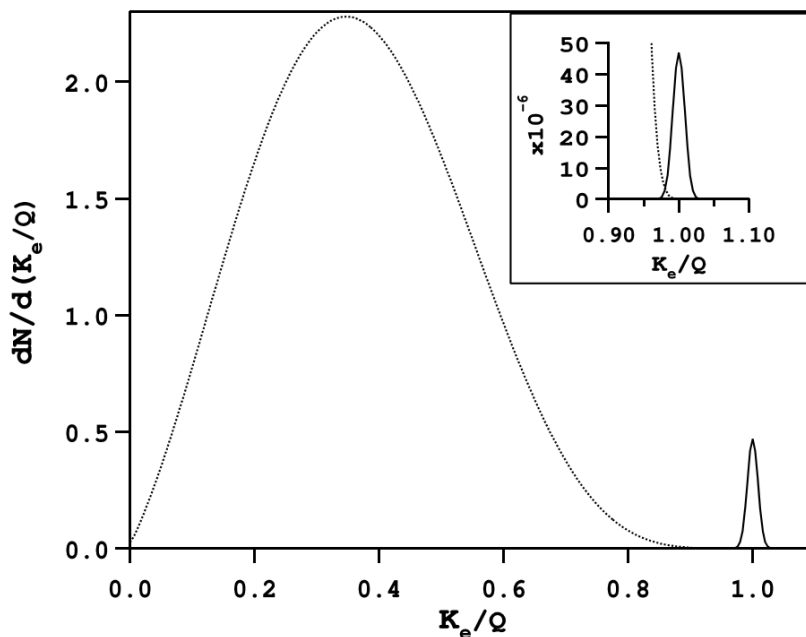


Figure 1.5.: Spectra of  $2\nu\beta\beta$  and  $0\nu\beta\beta$  decay:  $K_e$  is the energy of the electrons and  $Q$  the total energy of the decay. For illustration, the  $0\nu\beta\beta$  peak at the endpoint of the  $2\nu\beta\beta$  spectrum is largely amplified, while a more realistic ratio of rates  $\propto 10^{-6}$  is shown in the inset (from [Vog06]).

depending on the underlying theoretical calculation of the matrix element. It has to be emphasised that no event contributing to  $0\nu\beta\beta$  has been confirmed yet, leaving the question on the type (Majorana or Dirac) of neutrinos still open.

### 1.3.3. Neutrino Mass Limits from Single Beta Decay

(Inverse) single beta decay was the key process in neutrino physics since its start over 80 years ago. The main advantage is that it is of first order. Consequently single beta decay is also a key contribution when it comes to deriving information on the neutrino mass.

Single beta decay experiments are often denoted as "model independent" measurements of the neutrino mass, which seems likely, when comparing the direct laboratory approach of such experiments to the multiparameter analysis in cosmology. In the case of measurements connected to Majorana masses, for example double beta decay experiments, there is always the need of complimentary information or assumptions to decompose the contributing phases and mass eigenvalues. However, in single beta decay experiments these phases do not enter the observable, making them in principle directly sensitive to the mass eigenvalues of the neutrinos.

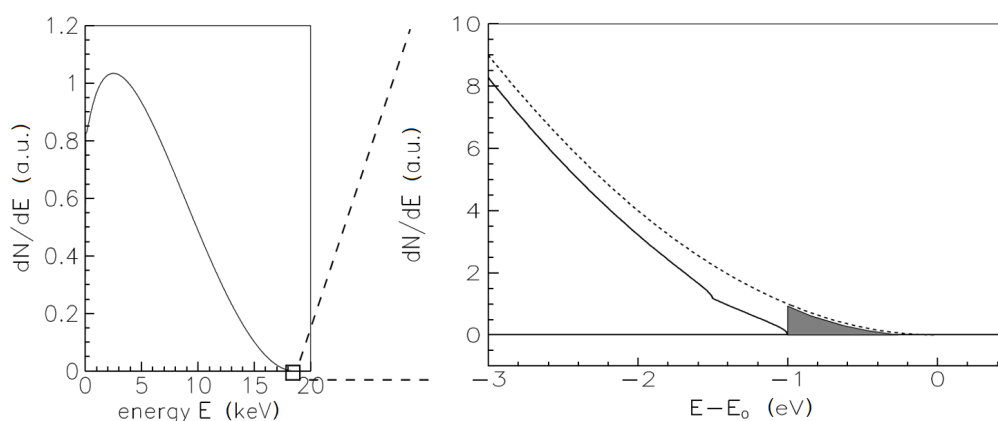


Figure 1.6.: Single beta decay spectrum of tritium: On the left the total spectrum with the endpoint of  $E_0 = 18.6$  keV is shown. Due to coulomb interaction, the lower part of the spectrum appears to be cut. The close-up on the right shows the 3 eV region below the endpoint, here for arbitrary mass eigenvalues of 1.0 eV ( $|U|^2 = 0.7$ ) and 1.5 eV ( $|U|^2 = 0.3$ ). At these masses two kinks are visible in comparison to the spectrum with zero mass (dotted). The fraction of the shaded area contains  $2 \cdot 10^{-13}$  of the total decays (from [Wei03]).

The main idea in single beta decay experiments is a precise analysis of the electron spectrum [OW08]:

$$\frac{d\dot{N}}{dE} = A(E) p_e E \underbrace{(E_0 - E)}_{E_\nu} \sum_i |U_{ei}|^2 \underbrace{\sqrt{(E_0 - E)^2 - m_i^2}}_{p_\nu} \theta(E_0 - E - m_i). \quad (1.14)$$

Here  $A(E)$  represents the amplitude, which depends on the matrix elements of the leptonic and hadronic transitions as well as the coupling constant. The rest of the product is a phase space factor including the kinetic energy  $E$  and momentum  $p_e$  of the electron, as well as the corresponding quantities for the neutrino. The  $\theta$  function ensures energy conservation. The endpoint energy  $E_0$  is given by the Q value (the released kinetic energy in the decay) corrected for the nuclear recoil energy which is constant near the endpoint. For simplicity a sum over the final states of the daughter atom or molecule has been left out.

Due to the energy momentum conservation, the neutrino mass eigenvalues modify the shape of the electron energy spectrum in the vicinity of the endpoint, most prominent in limiting the maximum electron energy. Due to the summation over the mass eigenvalues  $m_i$  this results in three distinct kinks at the end of the spectrum, which is shown in figure 1.6. However, no planned beta decay experiment will be able to actually render this features, due to the very low statistics in the endpoint region and due to the endpoint uncertainty itself.

In contrast, the observable which can be extracted by a very precise measurement of the shape of the electron spectrum in the endpoint region is an incoherent sum over the light

neutrino mass eigenvalues, which is given by [OW08]

$$m_{\nu_e}^2 = \sum_i^3 |U_{ei}|^2 m_i^2 . \quad (1.15)$$

The kinematic analysis of the electrons can be carried out in different ways, the most prominent being the usage of cryogenic bolometers [Gas+14] and spectrometry. In the latter case tritium is most frequently used as beta emitter, exhibiting several advantages, favourable for neutrino mass searches [OW08]:

- It combines a short half life time of  $T_{1/2} = 12.3$  yr with a low endpoint of  $E_0 = 18.6$  keV, which guarantees comparably high rates near the endpoint. Statistics plays a major role in this experiments, since even for tritium only a fraction of  $10^{-13}$  of the total decays occurs in the region 1 eV below the endpoint.
- It obeys a small nuclear charge  $Z = 1$ , which makes coulomb interactions of  $\beta$  electrons with tritium considerably small, while allowing generally easier calculations.
- The transition from parent to daughter nucleus in tritium beta decay is super-allowed, since both are mirror-nuclei. This makes the corresponding matrix element energy-independent and easier to calculate.

The most stringent limits on the neutrino mass from laboratory experiments have been obtained by the Mainz and the Troitsk neutrino mass experiments, both using a tritium source and a spectrometer combining Magnetic Adiabatic Collimation with an Electrostatic filtering (MAC-E). A combined analysis of the Particle Data Group results in the currently best limit of [OG14]:

$$m_{\bar{\nu}_e} < 2.0 \text{ eV (95 \% C.L.)} . \quad (1.16)$$

The Karlsruhe TRITium Neutrino KATRIN experiment aims to improve this limit by one order of magnitude, while exploiting the established tritium endpoint spectroscopy. The improvement is achieved by drastically increasing the source strength and dimensions of the experiment while on the same time lowering the systematic effects, thereby pushing the technology to its limits.

## 2. The Karlsruhe TRItium Neutrino Experiment KATRIN

The Karlsruhe TRItium Neutrino experiment, currently in its final construction and commissioning phase, will perform a kinematic measurement of the neutrino mass by precision spectroscopy of tritium beta decay electrons at the endpoint of 18.6 keV. Huge efforts are made to reach the planned sensitivity of 200 meV (90 % C. L.), exceeding the sensitivity of the predecessor experiments in Mainz and Troitsk by one order of magnitude [KAT04].

In section 2.1 the measurement principle and setup of the experiment are discussed. Section 2.2 is focused on the simulation and data analysis part of KATRIN.

### 2.1. Measurement Principle and Setup

To measure the neutrino mass, KATRIN performs a high-precision spectroscopy of the tritium  $\beta$  decay spectrum close to the endpoint. According to equation 1.14 the observable which can be extracted from this data, is the squared effective electron antineutrino mass (equation 1.15).

Improving the sensitivity on  $m_{\nu_e}$  by a factor of 10 compared to the predecessor Mainz and Troitsk experiments [Lob+01] requires an improvement of a factor 100 on  $m_{\nu_e}^2$ . This is achieved by increasing the dimensions of the experiment and source activity, while decreasing the requirements on systematic influences. A drawing of the whole, over 70 m long setup can be seen in figure 2.1. Molecular tritium  $T_2$  decays inside the *Windowless Gaseous Tritium Source* WGTS (figure 2.1b)) according to the following reaction:



The tritium gas is provided by the Tritium Laboratory Karlsruhe TLK in a nearly closed gas loop [Bor11]. Continuous filtering of the gas removes the daughter molecule  $HeT^+$  as well as other impurities, ensuring an isotopic tritium purity inside the source of more than 95%. The electron-anti-neutrinos  $\bar{\nu}_e$  rarely interact and leave the WGTS without a possibility to detect them directly. However, their mass is extractable from the electron energy spectrum due to energy momentum conservation. The spectrum is obtained by energy spectroscopy in the spectrometer section (figure 2.1d)+e)) and counting of the corresponding events at the detector (figure 2.1f)). To prevent the tritium from entering the spectrometers a pumping section (figure 2.1c)) connects the WGTS and the spectrometer section which

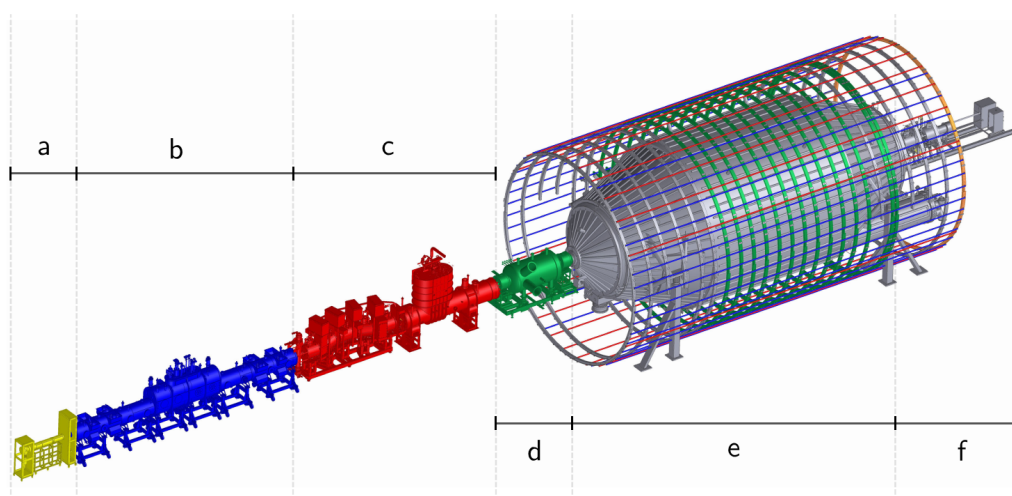


Figure 2.1.: The experimental setup of KATRIN, comprising:

- a) Rear Section, monitoring and calibration,
- b) Windowless Gaseous Tritium Source,
- c) Differential and Cryogenic Pumping Section, removal of the tritium,
- d) Pre spectrometer, filtering of low energy electrons,
- e) Main spectrometer, high resolution spectroscopy,
- f) Detector section, position resolved electron counting  
(from [Kle14]).

drastically reducing the tritium partial pressure. The rear section (figure 2.1a)) is used for calibration and monitoring.

Inside the WGTS the electrons are emitted isotropically. To guide them to the detector strong magnetic fields (in the range of a few tesla) are applied along the entire beam line by superconducting solenoids. However, the magnetic field setting is not only used to map the high source activity to the detector, but it is an integral part of the working principle of spectrometers of the Magnetic Adiabatic Collimation combined with an Electrostatic MAC-E filter type, which are used at KATRIN.

### The MAC-E Filter

The application of a certain magnetic field setting allows for a conversion of the initial isotropic electron momentum spectrum into a highly collimated one. Subsequently, when the motion of the electrons is mainly restricted into one direction, the energy spectroscopy can be carried out using an electrostatic retarding voltage  $U$ , working as a high pass filter.

This principle will be explained in the following, while an illustration of the MAC-E filter and the involved field settings can be found in figure 2.2.

Due to the Lorentz force the electrons will follow a cyclotron motion, in which their kinetic energy  $E_{\text{kin}}$  can be decomposed into a transversal  $E_{\perp}$  and a parallel component  $E_{\parallel}$  with

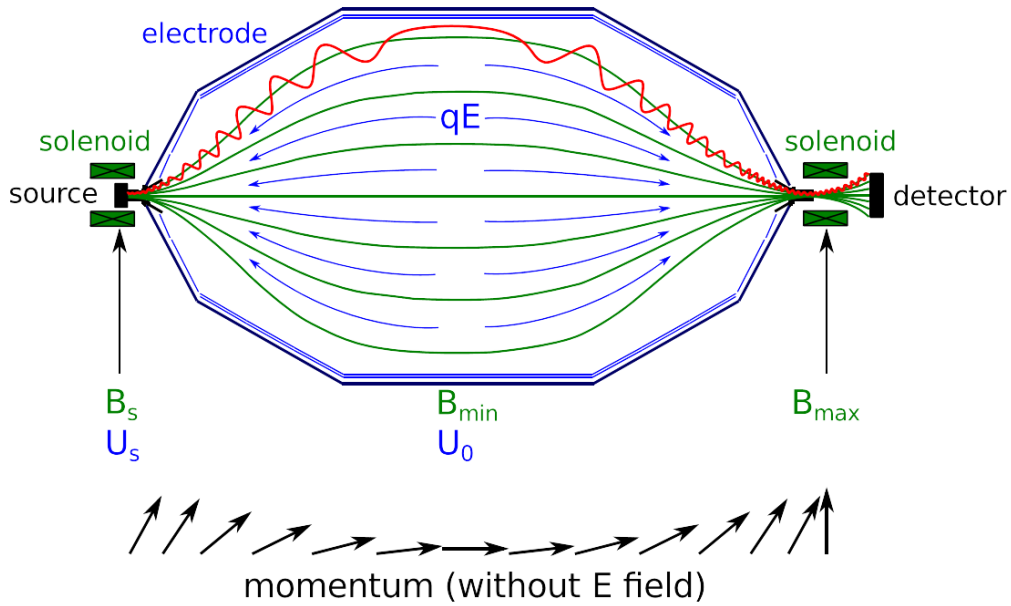


Figure 2.2.: Working principle of the MAC-E filter: A guiding field (green) is produced by superconducting solenoids, which takes its minimal values at the center of the spectrometer. Due to the conservation of the magnetic moment this converts the momentum of the electrons to be parallel to the magnetic field. Only those electrons with energies higher than the applied retarding potential  $qU$  can pass the center of the spectrometer (from [KAT04]).

respect to the magnetic field lines:

$$E_{\text{kin}} = E_{\perp} + E_{\parallel} . \quad (2.2)$$

The angle between the parallel component of the momentum and the total momentum will be denoted as the polar angle  $\theta$ .

Naturally the motion of the electrons is adiabatic ( $\delta E_{\text{kin}} = 0$ ) for vanishing electrical fields and for low magnetic field gradients:

$$\frac{\Delta B}{B} \ll 1 . \quad (2.3)$$

The corresponding adiabatic invariant under the assumption of non relativistic motion is the magnetic moment:

$$\mu = \frac{E_{\perp}}{B} = \text{const} . \quad (2.4)$$

Consequently, the transversal energy can be adjusted as a function of the magnetic field, where  $B_S$  denotes the magnetic field at the point of electron creation:

$$E_{\perp}(B) = E_{\perp}(B_S) \cdot \frac{B}{B_S} . \quad (2.5)$$

This relation is particularly useful, since it shows the possibility of transferring transversal to parallel energy by lowering the magnetic field. By additionally applying a retarding voltage  $U$ , the electrons will get reflected according to the following condition:

$$E_{\parallel}(\vec{r}) = E_{\text{kin}} - qU(\vec{r}) - \mu B(\vec{r}) \stackrel{!}{=} 0. \quad (2.6)$$

Thus, for a small magnetic field  $B_{\text{min}}$  only electrons with energies larger than  $qU$  can pass the spectrometer. MAC-E filters therefore perform an integrated energy measurement.

### Maximum Acceptance Angle

Following equation 2.5 the electrons should be created in the maximal magnetic field, to ensure the best collimation. It is however favourable to exclude electrons with large starting angles from the analysis, since they obey a larger path length inside the source tube. This leads to an enhanced energy loss due to scattering with the gas inside the WGTS and due to synchrotron radiation. A detection of these electrons can be avoided by exploiting the magnetic mirror effect, which applies, when charges propagate into an increasing magnetic field, thus by using equation 2.5 the other way around: if the maximum magnetic field is not in the source ( $B_{\text{max}} > B_{\text{S}}$ ), the transversal energy can increase to a point, where the parallel energy is zero. Subsequently the electron will get reflected, when it is created with an angle larger than the maximum acceptance angle of:

$$\theta_{\text{max}} = \arcsin \sqrt{\frac{B_{\text{S}}}{B_{\text{max}}}}. \quad (2.7)$$

### Filtering Width

The smallness of  $B_{\text{min}}$  is limited due to the finite size of the vacuum vessel and due to the conservation of the magnetic flux: When the magnetic field strength is reduced, the field lines expand, eventually colliding with the vacuum vessel for too low fields. This is a key condition when planing the radius of the spectrometer, since it limits the energy resolution.

Compared to an electron with starting angle  $\theta = 0^\circ$  and energy  $E = qU$ , which can just pass the potential, an electron starting with the maximal acceptance angle  $\theta = \theta_{\text{max}}$  needs the following surplus energy  $\Delta E$  to be detected:

$$\Delta E = E \cdot \frac{B_{\text{min}}}{B_{\text{max}}}. \quad (2.8)$$

$\Delta E$  is called the filtering width (or sometimes energy resolution) of the spectrometer. It should be noted that it scales linearly with the energy of the particles.

### Transmission Function

The filtering width has been derived considering two special, extreme polar angles, thereby representing the width of the step function which describes the transmission probability

of the particles for general angles and energies. This function is the so called transmission function  $T(E, qU)$ . In first order it can be described analytically, where for isotropically generated electrons it holds [KAT04]:

$$T(E, qU) = \begin{cases} 0 & E - qU < 0 \\ \frac{1 - \sqrt{1 - \frac{E - qU}{E} \cdot \frac{B_S}{B_{\min}}}}{1 - \sqrt{1 - \frac{B_S}{B_{\max}}}} & 0 \leq E - qU \leq \Delta E \\ 1 & E - qU > \Delta E \end{cases} . \quad (2.9)$$

Due to additional effects, mainly inelastic scattering of the electrons on the gas inside the WGTS, the transmission function gets convoluted into the response function, which is shown in section 2.2.2.

### Spectrometer and Field Setting at KATRIN

The KATRIN setup comprises three spectrometers of MAC-E filter type:

- the main spectrometer (figure 2.1e)), which will be used for the high resolution spectroscopy in an approximately 30 eV interval below the tritium  $\beta$  spectrum endpoint,
- the pre-spectrometer (figure 2.1d)), which can be used to free the main spectrometer from the huge background of the whole tritium  $\beta$  spectrum, by setting its retarding voltage to a few hundred eV below the endpoint
- and the monitor spectrometer (not shown), which will be used to monitor the retarding voltage stability of the main spectrometer section, by analysing a krypton-83m conversion electron spectrum.

The design values for the magnetic field configuration of KATRIN are  $B_S = 3.6$  T,  $B_{\min} = 3 \cdot 10^{-4}$  T and  $B_{\max} = 6$  T, leading to a maximum acceptance angle and filtering width at the tritium endpoint ( $E_0 \approx 18.6$  keV) of:

$$\theta_{\max} \approx 50.8^\circ \quad \text{and} \quad \Delta E \approx 0.93 \text{ eV} . \quad (2.10)$$

Correspondingly, the length of the main spectrometer vacuum vessel is about 23 m, with a maximum diameter of about 10 m.

According to equation 2.6 the magnetic field at its minimal value has to be very well controlled in terms of homogeneity. Therefore the main spectrometer is concluded by a large volume air coil system, which is used for compensation of the earth magnetic field and fine shaping of the field configuration. High precision of the retarding voltage is among others achieved by a complex wire electrode system on the inside of the tank, which also provides a significant background reduction concerning electrons ejected from the  $690 \text{ m}^2$  surface of the vessel.

It is worth mentioning, that the finite filtering width, which is much larger than the envisaged neutrino mass sensitivity of 200 meV, does not prevent the latter to be achieved.

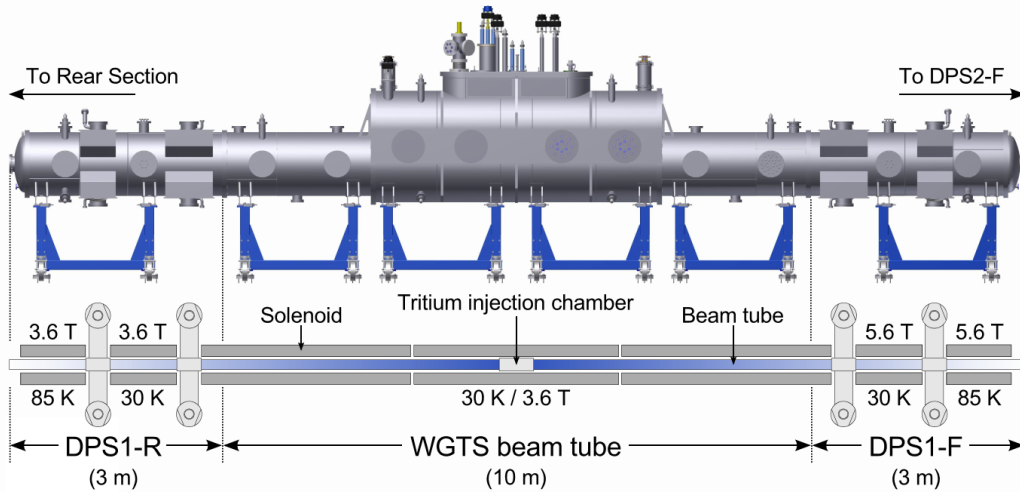


Figure 2.3.: Windowless Gaseous Tritium Source: The central part of the WGTS is the 10 m long, temperature stabilized cryostat. High-purity tritium is injected in the central injection chamber. The tritium gas is removed at each end of the beam tube in differential pumping sections (DPS1-R and DPS1-F). On left and right the setup is connected to the Rear and Transport Section respectively (from [Har15]).

This can be explained, since the shape of the transmission function is precisely known and the spectral distortion due to the non-vanishing neutrino mass is observable at larger scales than  $\Delta E$  [Kle14].

### The Windowless Gaseous Tritium Source

The Windowless Gaseous Tritium Source (WGTS, figure 2.3) provides the tritium gas for the  $\beta$  spectrum measurement, combining high luminosity with small systematic uncertainties. The pipe of approximately 10 m length and 90 mm diameter is embedded in a complex two-phase neon cryostat, ensuring a constant temperature of around 30 K with a stability of 30 mK. The low temperature has been chosen to reduce the Doppler effect and plasma formation and to ensure a high tritium density, while keeping low tritium pressures and flow rate [KAT04]. The stability is crucial, since it is directly related to the stability of the column density, which is of utmost importance considering the low signal rates at the endpoint. The tritium column density itself will be  $\rho d \approx 5 \cdot 10^{21} \text{ m}^{-2}$ , which is a compromise between a high signal rate and low electron gas scattering, hence reducing systematic effects due to energy loss. Avoiding systematic effects is also the main reason for keeping the tritium source windowless, which implies that the whole system from the source to the detector is a closely connected vacuum system without any solid barriers.

To prevent the tritium gas from entering the spectrometer section, various measures are applied. In particular the tritium source is on both sides connected to *Differential Pumping Sections* (DPS1-R and DPS1-F), which reduce the pressure from  $p_{\text{inj}} \approx 3 \cdot 10^{-3} \text{ mbar}$  at the injection in the middle by around 2 orders of magnitude. In direction to the spectrometer,

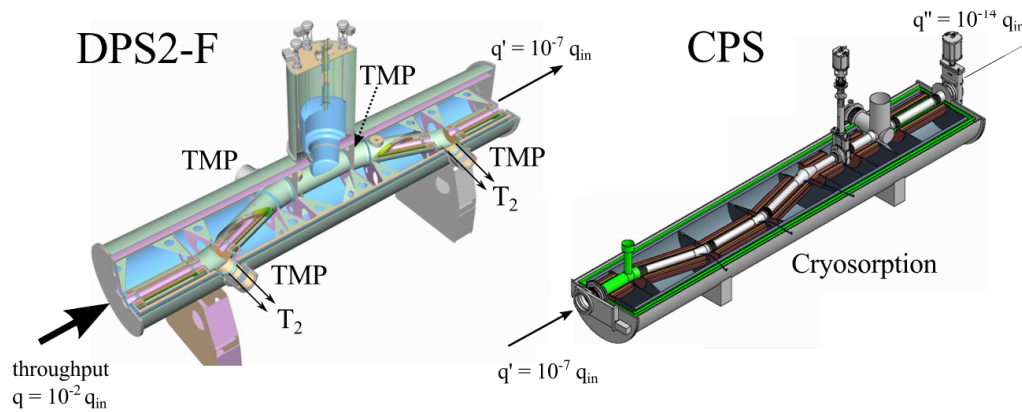


Figure 2.4.: Differential and cryogenic pumping section: The DPS2-F (left) reduces the tritium gas throughput  $q$  by 5 orders of magnitude with the usage of turbo molecular pumps. The CPS provides another 7 order of magnitude reduction by using cryosorption. In both components the beam tubes are tilted against each others, maximizing the pumping speed (from [Höt12]).

the setup is followed by the transport section, which ensures a further reduction of the gas density, while transporting the electrons to the spectrometer section adiabatically via magnetic field lines.

## The Transport Section

Keeping the gas pressure inside the main spectrometer below  $10^{-11}$  mbar is crucial to minimize electron scattering processes [KAT04]. An even stricter limit applies for the partial pressure of tritium compounds, which should not exceed  $10^{-20}$  mbar for safety and background reasons. This can only be reached by the combination of two different pumping principles, realised in a second differential pumping section DPS2-F and the *Cryogenic Pumping Section* CPS. At the same time the adiabatic transport of the electrons from the WGTS to the spectrometer section has to be guaranteed.

The DPS2-F consists of five connected tubes each with a tilt of  $20^\circ$  (figure 2.4 left) to avoid a direct line of sight to the spectrometer section for neutral particles like tritium molecules. At the connections 4 *Turbo Molecular Pumps* TMP are mounted, which altogether reduce the incoming tritium gas flow by 5 orders of magnitude. The system is complemented by superconducting solenoids with a maximum field of up to 5.5 T, which ensures an adiabatic transport of the electrons through the 7 m long unit.

The CPS (figure 2.4 right) provides another reduction of the tritium flow by 7 orders of magnitude by using the principle of cryosorption. Thereby the tubes are arranged to form a chicanery for neutral particles, which get adsorbed on a 4 K argon frost when colliding with the walls.

Since charged ions will not be affected by these pumping processes they will be removed using a system of dipole electrodes installed in the DPS2-F [Jan15].

## The Detector Section

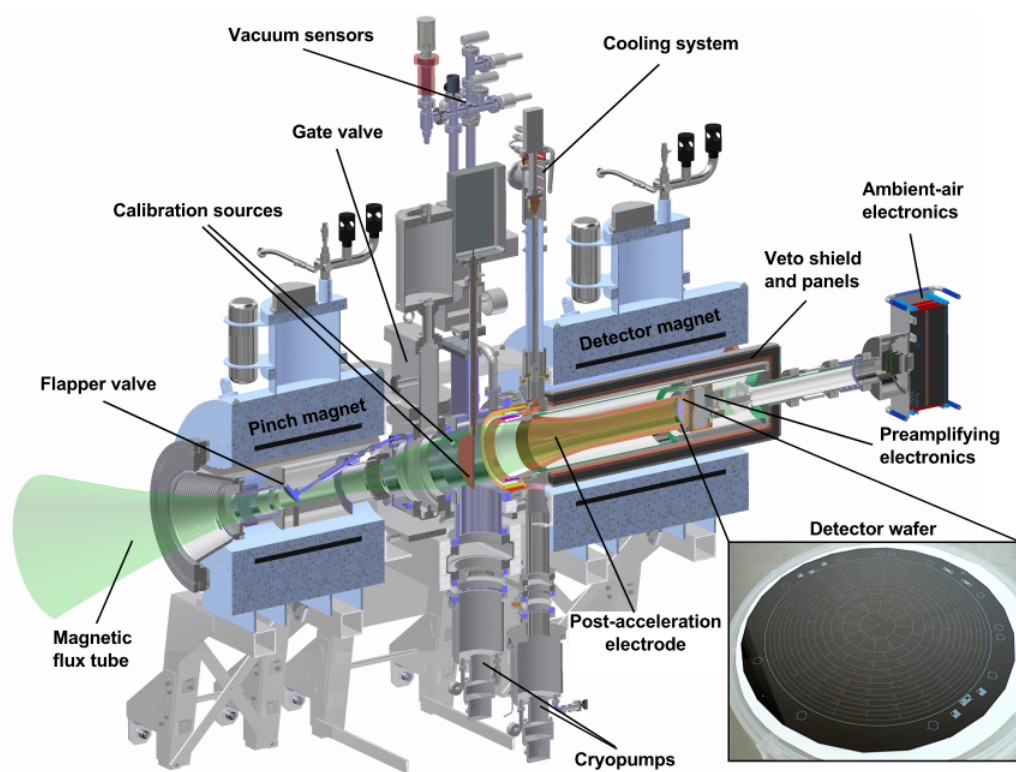


Figure 2.5.: Focal plane detector system: in addition to two magnets, the vacuum system and the shielding, the setup comprises calibration sources. Furthermore the electrons can be post-accelerated to an energy region with a preferable signal-to-background ratio. The inset shows the segmented silicon wafer (from [Har15]).

Electrons which have passed the main spectrometer will be re-accelerated and guided to the *Focal Plane Detector* FPD system (figure 2.5). Its main component is a 90 mm silicon PIN diode array which is divided into 148 pixels, thus enabling a radial analysis of the signal. Since the electron spectroscopy takes place at the main spectrometer, the energy resolution of the FPD of about 1 keV (depending on the wafer) is only important for background discrimination. Due to the low signal rate a proper shielding against background is necessary, which is achieved combining passive copper and lead shells with an active plastic scintillator veto system. Consequently the detector is optimized for efficiency rather than maximum rate and its current limit in recordable rate lies in the 10 kcps range per pixel <sup>1</sup> [Ber+12]. Although this is completely sufficient for measurements at the  $\beta$  spectrum endpoint, the limit might be strongly enhanced in the near future by an improved analysis method [Eno13], which will be very useful for deeper  $\beta$  spectrum and calibration measurements.

<sup>1</sup>This depends on the mode which is used as well as on the number of pixels, which are readout simultaneously. Further reading for example in [Sch14].

## The Rear Section

At the rear side of the DPS1-R, the Rear Section is located, which provides several calibration and monitoring devices:

- An angular-resolved electron gun for the measurement of the electron energy loss function and frequent column density measurements, making use of inelastic scattering [Bab14].
- Defining of the electrical potential of the source with a gold plate perpendicularly to the magnetic field lines.
- Monitoring of the source activity with  $\beta$  *Induced X-ray Spectroscopy* BIXS, utilizing X-rays which are emitted from the gold plate due to electron impact [Röl15].

## 2.2. Neutrino Mass Analysis with KATRIN

The KATRIN experiment involves a great many of components yielding a huge amount of operating parameters and sensor data. Hence, the result for the neutrino mass is no simple reading value of any physical instrument, but it is subjected to a complex measurement setup, which requires for a statement on the conducted analysis. This will be discussed in 2.2.1.

The organisation and evaluation of the data is only feasible due to a sophisticated software framework. A mandatory part of the analysis is the possibility to precisely simulate the expected outcome of the experiment in dependency of its observables. The corresponding tools will be explained in 2.2.2.

Finally the simulation combined with the analysis strategy can be used to predict the sensitivity of KATRIN on the neutrino mass, which will be discussed in chapter 2.2.3.

### 2.2.1. $\chi^2$ Analysis with KATRIN

This section gives a quick overview of a simple way of analysing methods used at KATRIN. The methods described are not settled for the final analysis with actual measurement data, but they are very useful in primarily predicting KATRIN sensitivities. Further reading can be found in [Kle14].

The data which will be ultimately taken by KATRIN in each run is the total number of integrated counts  $N_{\text{obs},i}$  for  $i$  settings of retarding potentials  $qU_i$  with corresponding measurement times  $t_i$ . This will be accompanied by a huge amount of sensor and monitoring data as well as operating parameters of all the components of the over 70 m long experiment, which will have an influence on the measured  $N_{\text{obs},i}$ .

Therefore, the parameter of interest  $m_\nu$  is no direct outcome or reading value of any measurement device, but it is only accessible via a model, which predicts the expected number of counts  $N_{\text{theo},i}(m_\nu^2)$  for every setting of retarding potentials  $qU_i$  with measurement times  $t_i$ .

In practice, the theoretical prediction of  $N_{\text{theo},i}$  will never be exact due to incomplete modelling and to uncertainties of observed quantities. One possible solution is to make  $N_{\text{theo},i}$  dependent on further free parameters  $x \in X$ . In the case of KATRIN neutrino mass measurement this so called nuisance parameters comprise the  $\beta$  spectrum endpoint  $E_0$ , the background rate  $R_{\text{bg}}$  and the spectrum intensity  $I$  <sup>2</sup>.

A way of dealing with systematic uncertainties is to determine how much they affect the estimates of the free parameters and to interpret the resulting shift as a systematic error  $\sigma_{\text{syst}}(X)$  <sup>3</sup>.

---

<sup>2</sup>The parameters may very well be phenomenological corrections. This is obvious for the intensity, which compensates for inaccuracies in the prediction of the integrated rate.

<sup>3</sup>There is no immediate rule to decide which group of uncertainties is treated which way. However, uncertainties with a large influence on the result are more likely to be treated as nuisance parameters.

The extraction of the true values of the  $X$  out of the measurement data is however even theoretically impossible: Since the data is the result of a radioactive decay, the signal  $N_{\text{theo},i}$  will naturally obey a statistical character, i.e. a Poissonian distribution. This means, that if the experiment was repeated several times, each time it would yield a different arrangement of the  $X$  due to statistical fluctuations. When the statistical process (here the Poissonian distribution) is known, it is however possible to predict the frequency distribution of the  $X$  after an infinite amount of measurements, even if only one is actually made. The corresponding probability distribution is referred to as the likelihood  $L$ .

For a sufficiently large number of signal events ( $\gtrsim 25$ ), the poissonian distribution of the individual number of counts  $N_{\text{obs},i}$  can be approximated by a Gaussian. Consequently, the likelihood is a product of Gaussian distributions for every measurement point [Kle14]:

$$L(N_{\text{obs}}, N_{\text{theo}}) = \prod_i \exp -\frac{1}{2} \left( \frac{N_{\text{obs},i} - N_{\text{theo},i}}{\sigma_i} \right)^2. \quad (2.11)$$

Due to the Poissonian nature of the observed count the weights  $\sigma_i$  can be written as:

$$\sigma_i = \sqrt{N_{\text{theo},i}}. \quad (2.12)$$

It is common not to search for the maximum likelihood, but to minimize the (double) negative log likelihood, the  $\chi^2$  function:

$$\chi^2 \equiv -2 \log L = \sum_{i(qU)} \left( \frac{N_{\text{obs},i} - N_{\text{theo},i}(X)}{\sigma_i} \right)^2. \quad (2.13)$$

Hence,  $\chi^2$  minimization is sometimes referred to as weighted least squares [Jam04].

The result of the experiment will than be the arrangement of the  $X$  yielding the maximum likelihood (or minimum  $\chi^2$ ) combined with the declaration of a confidence interval, which reflect the width of the systematic  $\sigma_{\text{syst}}(X)$  and statistical error  $\sigma_{\text{stat}}(X)$ .

## Sensitivity in the Case of Gaussian Distributed Observables

The  $\sigma_{\text{stat}}$  and  $\sigma_{\text{syst}}$  only provide meaningful information, if the distribution of the respective parameter is known. The distribution of a fit parameter  $x$  is obtained by interpreting the likelihood as a function of  $x$ . It is exactly a gaussian, when  $\chi^2$  as a function of  $x$  obeys a parabolic shape in the vicinity of the minimum, which is related to a linear scaling of  $N_{\text{theo},i}$  with  $x$  [Jam04].

This linear scaling may very well be prohibited by the physical model, however it can also be a matter of parametrisation: In the case of KATRIN, where the neutrino mass is thought to enter the physical model to the second,  $m_\nu^2$  (and not  $m_\nu$ ) obeys a Gaussian distribution.

---

For example this is true in the case of the tritium endpoint. Further reading can be found for example in [Bar02].

Since the counts in 2.13 are directly proportional to the total measurement time  $t_{\text{tot}}$ , for Gaussian distributed variables an anti proportionality of the statistical error and the square root of  $t_{\text{tot}}$  can be expected:

$$\sigma_{\text{stat}}(X) \propto \frac{1}{\sqrt{t_{\text{tot}}}} . \quad (2.14)$$

This is a direct consequence of the Poissonian nature of the signal. In case of Gaussian distributions, the exact relationship is connected to the second derivative of the  $\chi^2$  function.

In a complex experiment like KATRIN there are many sources of experimental and theoretical uncertainties. Thanks to the central limit theorem, the total systematic error can be considered Gaussian, with the individual contributions (and possible correlation terms) added in quadrature. Thus, since systematic and statistical errors are by definition uncorrelated, it holds

$$\sigma_{\text{tot}} = \sqrt{\sigma_{\text{stat}}^2 + \sigma_{\text{sys,tot}}^2} . \quad (2.15)$$

For Gaussian distributions the level of confidence can be easily calculated by the multiplication of  $\sigma$  with constant factors, where for example a  $1.645 \sigma$  interval covers 90 % of the total area of a Gaussian and  $1.0 \sigma$  interval only comprises 68.3 %.

The sensitivity can be transformed to other parametrisations of a Gaussian distributed quantities by means of the transformation rule. In the case of the neutrino mass, this means that the sensitivity can be obtained by taking the square root of the result for the neutrino mass squared.

## Non Physical Values due to Statistical Fluctuations

Due to statistical fluctuations it is very well possible that the likelihood distribution extends to non physical regions of a parameter. A common solution is to use a mathematical continuation of the model, which yields a symmetrised likelihood with respect to the boundary. In case of  $m_\nu^2$  this means, that the model has to be continued to regions with  $m_\nu^2 < 0$ , where the respective equations can be found in [Kle14].

### 2.2.2. Spectrum Simulation

For an experiment with the complexity of KATRIN the  $N_{\text{theo},i}$  in equation 2.11 as well as the likelihood calculation itself can only be carried out within a comprehensive software framework. For the latter KATRIN uses the software package KaFit, which is based on the C++ package Root. The structure can be seen in figure 2.6. The likelihood analysis can be carried out using different approaches, with classical minimizers (Minuit and Minos, further reading in [Jam04]) and Markov Chain methods. These two ways represent different analysis strategies (frequentist or bayesian), where it has been shown in [Kle14] that the results correspond to each other for KATRIN<sup>4</sup>. A key role plays the component

---

<sup>4</sup>The distinction between a frequentist and a bayesian analysis is in particular important in the way how systematic errors can be treated. In a bayesian analysis every systematic can be treated as a nuisance

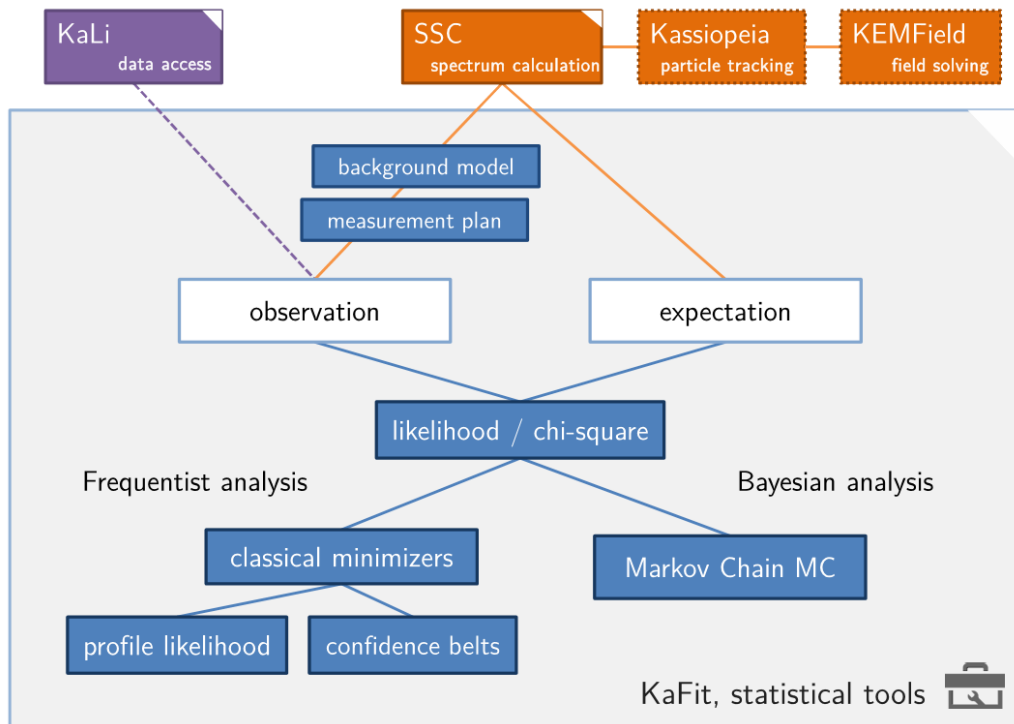


Figure 2.6.: Structure of the KATRIN analysis tool KaFit: the central task of KaFit is a likelihood/chi-square analysis comprising the observed and expected measurement. The latter is supplied by SSC, the second central tool of the KATRIN software framework. For the purpose of pre-measurement simulation studies, SSC can also supply pseudo data. The analysis itself can be realized with different algorithms, reflecting either the frequentist or bayesian statistical approach (picture from [Kle14]).

*Source Spectrum Calculation* SSC, which can supply both the expectation  $N_{\text{theo},i}$  and the expected observation, for pre measurement studies.

## Source Spectrum Calculation

SSC offers the possibility to calculate the expected integrated count rate  $\dot{N}(qU)$  at the detector separately for every of its 148 pixels. Consequently KATRIN analysis can include radial dependencies concerning the background, the transmission properties and the source model. The latter is possible, since the magnetic field maps a certain region of the WGTS to a distinct pixel of the detector, which can be seen in figure 2.7. To include axially ( $z$ ) dependencies in the source model, SSC performs a further segmentation into slices of the WGTS, where in every slice the corresponding physical quantities are taken to be constant. Hence, the total spectrum at one pixel is modelled as the sum over independent

---

parameter, where guesses on the size of this errors can be included as a prior. The frequentist analysis does not accept strong priors, correspondingly it has to rely on the usage of systematic uncertainties rather than nuisance parameters.

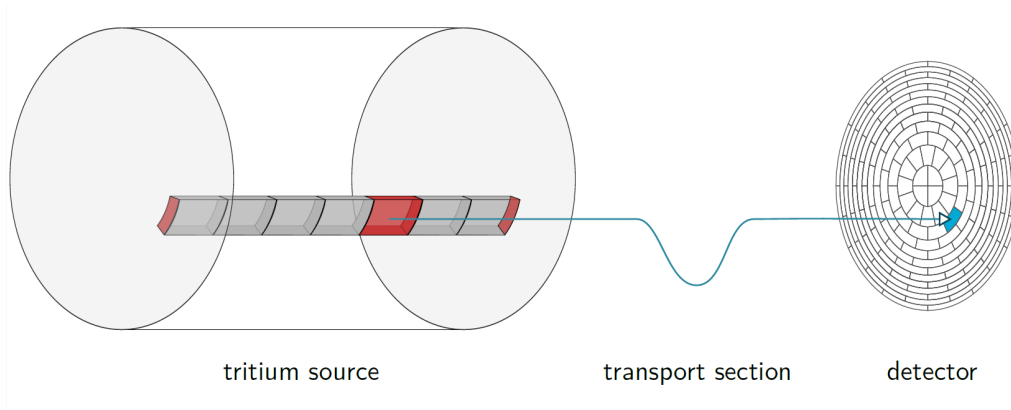


Figure 2.7.: Mapping of source regions to the detector and voxelisation: The magnetic field forces electrons created on the same field line to the same detector pixel. The measured spectrum of this pixel consists of a summation over all source regions along this field line (indicated in grey). The analysis can be carried out for every pixel separately by dividing the source into corresponding voxels (after [Kle14] and [Höt12]).

WGTS slices, which is reflected in the following, basic equation:

$$\dot{N}(qU) = \sum_i^{\text{slices}} \epsilon_{\text{det}} \frac{\Omega_i}{4\pi} \int_{-\infty}^{\infty} N_i \left( \frac{d\dot{N}}{dE} \right) R(E, qU + V_i) dE . \quad (2.16)$$

Here  $\epsilon_{\text{det}}$  is the detector efficiency,  $\frac{\Omega}{4\pi}$  the accepted solid angle,  $N$  the number of tritium atoms,  $\frac{d\dot{N}}{dE}$  the differential tritium spectrum and  $R(E, qU)$  the response function of the experiment. The latter includes every external influence on the electrons energy distribution from their emission inside the WGTS to their detection at the focal plane detector, for example the transmission function of the spectrometer, scattering with gas or potentials  $V$  inside the WGTS. Every of the constituents in equation 2.16 is subjected to a detailed modelling, giving a precise description of the physical process, where for example the differential spectrum will include a (relativistic) Doppler broadening, excitations of the daughter molecule or the nuclear recoil.  $z$  dependent quantities from the source model like the number of tritium atoms or the potential in a slice are taken from corresponding profiles, where for example the density profile is provided by gas dynamical computations. The entire structure of SSC is highly flexible, since every of the constituents is represented by a distinct C++ class, which enables easy additions both in terms of more comprehensive descriptions and new experimental setups. The latter comprises for example the search for sterile neutrinos with KATRIN or the WGTS krypton-83m mode, which has been implemented in this work (chapter 3).

Two essential parts of the above equation are shortly rendered in the following. In figure 2.8 and figure 2.9 the energy loss function and the response function for nominal tritium conditions can be seen. Since the minimal inelastic energy loss due to excitation processes is in the range of 13 eV, the transmission edge in the response function is followed by a plateau region of constant transmission probability. This is followed by consecutive

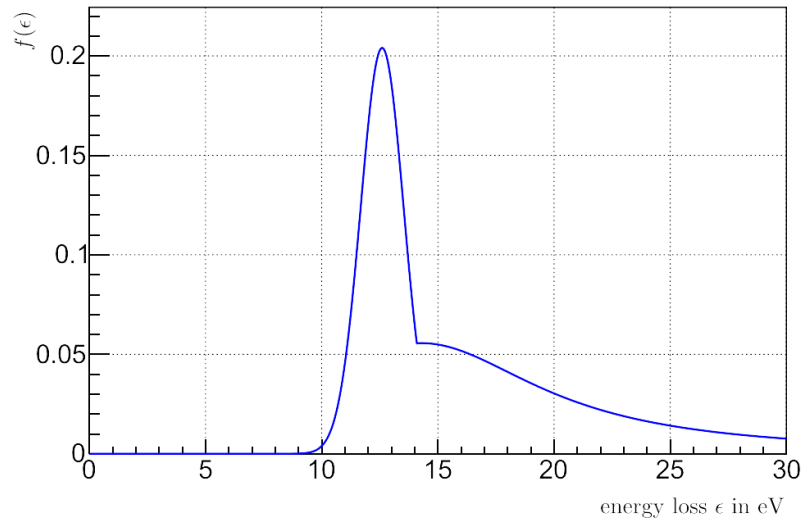


Figure 2.8.: Energy loss function, describing the inelastic energy loss of electrons due to scattering on tritium molecules: The minimal possible energy loss is in the range of 13 eV, reflected in the visible peak. Due to the width in the few eV range and the large tails, the electron spectrum gets smeared as a consequence of the energy loss (data from [Ase+00], plot from [Gro15]).

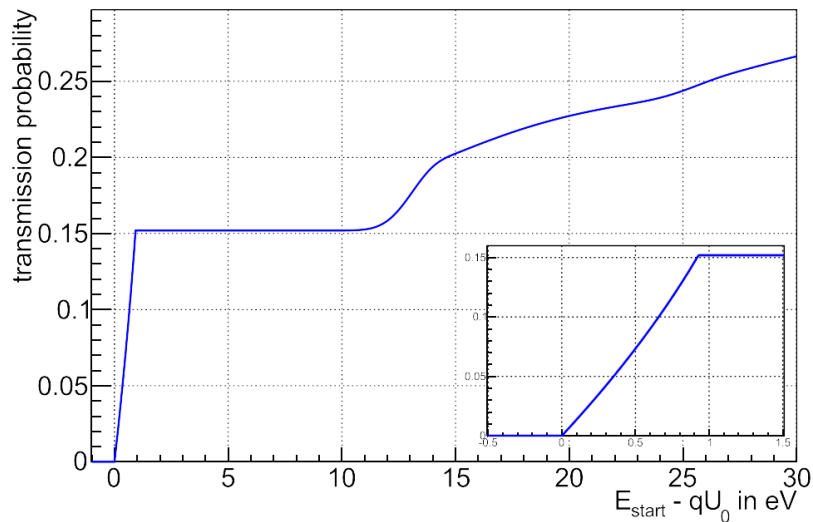


Figure 2.9.: Response function for nominal KATRIN conditions: below 1 eV, the response function is dominated by the transmission function, where a close-up can be seen in the inset. Small deviations to the analytical form presented in section 2.1 can be observed. The overall form for higher energies is dominated by multiple energy losses (picture from [Gro15]).

Table 2.1.: **KATRIN systematic uncertainties.**

Identified sources of systematic errors in the KATRIN experiment, with upper limit for the absolute induced neutrino mass shift and accuracy requirements (from [KAT04]).

source of systematic shift	achievable / projected accuracy	systematic shift $\sigma_{\text{syst}}(m_\nu^2)$ ( $10^{-3}$ eV <sup>2</sup> )
description of final states	$f < 1.01$	$< 6$
T <sup>-</sup> ion concentration	$< 2 \cdot 10^{-8}$	$< 0.1$
unfolding of energy loss func. $f(\epsilon)$		$< 6$
monitoring of column density $\rho d$	$\Delta T/T < 2 \cdot 10^{-3}$	$< \frac{\sqrt{5} \cdot 6.5}{10}$
	$\Delta \Gamma/\Gamma < 2 \cdot 10^{-3}$	
	$\Delta \epsilon_T/\epsilon_T < 2 \cdot 10^{-3}$	
	$\Delta p_{\text{inj}}/p_{\text{inj}} < 2 \cdot 10^{-3}$	
	$\Delta p_{\text{ex}}/p_{\text{ex}} < 0.06$	
background slope	$< 0.5$ mHz/keV (Troitsk)	$< 1.2$
HV variations	$\Delta \text{HV}/\text{HV} < 3$ ppm	$< 5$
WGTS potential variations	$\Delta U < 10$ meV	$< 0.2$
WGTS mag. field variations	$\Delta B_S/B_S < 2 \cdot 10^{-3}$	$< 2$
elastic e <sup>-</sup> - T <sub>2</sub> scattering		$< 5$
<b>identified syst. uncertainties</b>	$\sigma_{\text{syst,tot}} = \sqrt{\sum \sigma_{\text{syst}}^2} \approx 0.01$ eV <sup>2</sup>	

steps with a separation of 13 eV, representing multiple scattered electrons. Due to the width of the peak and the continuous tail in the energy loss function, the steps of scattered electrons get broadened.

### 2.2.3. Sensitivity of KATRIN on the Neutrino Mass

The sensitivity of KATRIN on  $m_\nu$  as defined in [KAT04] is actually a statement on the ability of excluding the null hypothesis of vanishing neutrino mass with a certain level of confidence. Following the considerations in 2.2.1, it is given by:

$$S_{m_\nu}(90\%) = \sqrt{1.645 \cdot \sigma_{\text{tot}}(m_\nu^2)} = \sqrt{1.645 \cdot \sqrt{\sigma_{\text{stat}}^2(m_\nu^2) + \sigma_{\text{syst}}^2(m_\nu^2)}}. \quad (2.17)$$

The determination of  $\sigma_{\text{stat}}(m_\nu^2)$  has been the subject of many analyses in the recent years. It will strongly depend on certain assumptions like the background rate, the *Measurement Time Distribution* MTD and on the radial analysis of the detector pixels. With the reference MTD from the design report [KAT04], a total measurement time of 3 years data taking and the assumption of a 10 mcps background, the most recent analysis yields [Kle14]:

$$\sigma_{\text{stat}}(m_\nu^2) = 0.0165 \text{ eV}^2. \quad (2.18)$$

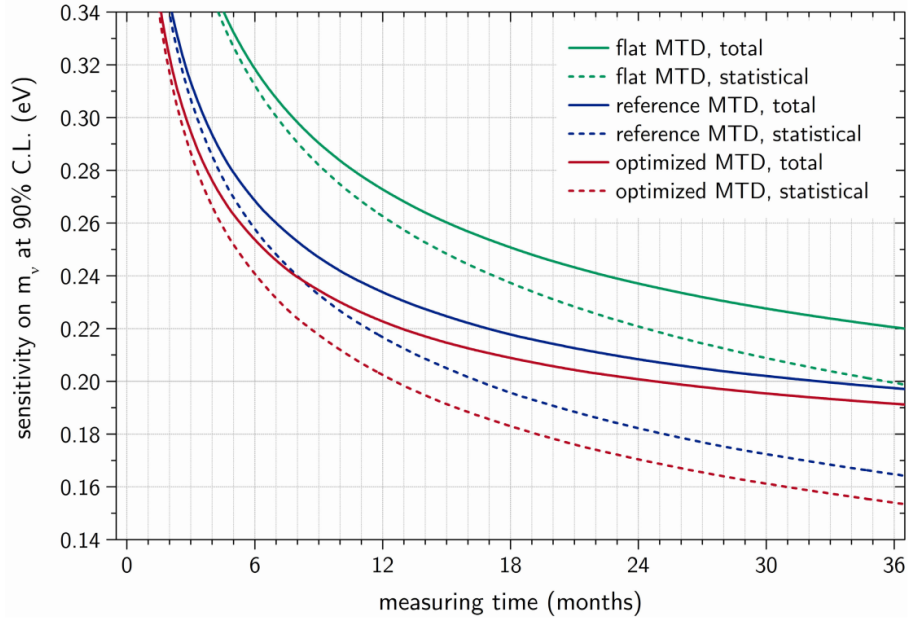


Figure 2.10.: Sensitivity on  $m_\nu$  as a function of the total measurement time for different MTDs: the statistical error on  $m_\nu$  scales with  $\sqrt[4]{t}$ , where the proportionality constant is influenced by the details of the MTD. The systematical error of  $\sigma_{\text{sys,tot}}(m_\nu) = 130 \text{ meV}$  asymptotically limits the total sensitivity (from [Kle14]).

The determination of  $\sigma_{\text{syst}}(m_\nu^2)$  requires a comprehensive list of all the identified, relevant systematics, which can be found in table 2.1.

The total sum of identified systematic uncertainties is found to be  $\sigma_{\text{sys,tot}} = 0.01 \text{ eV}^2$ . Since no individual systematic shifts the neutrino mass more than  $\Delta m_\nu^2 = 0.0075 \text{ eV}^2$ , the total systematic budget of KATRIN has been chosen in a way, that it might include unidentified effects and that it is on the same level as the statistical error, to:

$$\sigma_{\text{sys,tot}} \lesssim 0.017 \text{ eV}^2 . \quad (2.19)$$

Hence, when added up in quadrature following equation 2.17, the following sensitivity of KATRIN is obtained:

$$S_{m_\nu}(90\%) = 197 \text{ meV} . \quad (2.20)$$

In 2.10 the sensitivity as a function of the total measurement time can be seen, for the scenario of different MTDs. The total sensitivity is fundamentally limited by the systematic uncertainty, to which it asymptotically converges. Hence, identifying, understanding and quantifying systematic errors as well as the calibration of the measurement devices is a key ingredient of physical experiments.

For a high precision, large scale experiment like KATRIN this requires for numerous calibration and measurement tools, enabling a detailed monitoring of the components as well as investigations on potential error sources.

This work is focused on the  $^{83\text{m}}\text{Kr}$  mode of the gaseous source, which will be used to revise the electrical potential of KATRIN not only at the spectrometer section, but essentially at the point of electron creation inside the WGTS. This is related to the item *WGTS potential variations* in table 2.1. The usage of the  $^{83\text{m}}\text{Kr}$  mode requires an incorporation into the KATRIN analysis framework SSC, which also involves a comprehensive understanding of the related physics. This will be the topic of the following chapter.

### 3. $^{83\text{m}}\text{Kr}$ Mode of the Windowless Gaseous Tritium Source for Investigation of Systematics

In this chapter, the  $^{83\text{m}}\text{Kr}$  mode of the gaseous tritium source is introduced, which in principle provides the possibility of identifying and to some extent quantifying several of the source-related systematics affecting the tritium  $\beta$  spectrum. The basic idea is to inject a well-characterised gaseous electron source into the WGTS where systematic effects will be observable as changes in the spectral shape [Wil03; Bon03]. Conversion electrons from  $^{83\text{m}}\text{Kr}$  as a calibration standard have successfully been used in neutrino experiments [Rob+91; Wil+87; Pic+92; SD95; FP12], as well as in dark matter searches [LUX+14]. In case of KATRIN the  $^{83\text{m}}\text{Kr}$  mode is the favourable way of analysing WGTS plasma related effects, which are at the centre of the studies presented in this work.

The reasoning leading to the choice of  $^{83\text{m}}\text{Kr}$  as electron source is the following [KAT04]: The measurement principle of KATRIN relies on the difference of the electrostatic potential at the electron source with respect to the point of measurement in the analysing surface. This potential difference has to be carefully calibrated and monitored, satisfying three major requirements: Since the KATRIN sensitivity lies in the sub-eV range, the potential difference has to be calibrated with a precision in the sub-volt range <sup>1</sup>. Meeting this requirement is achievable with a quasi monoenergetic calibration source. Moreover, the only method to be sensitive to the electrical potential of the WGTS consists of a calibration source dispersed *inside* the WGTS along with the tritium gas. In addition, KATRIN is a low background experiment, meaning that the calibration source should be removable on short time scales, to avoid interferences with the tritium measurement mode or a contamination of the experiment.

Gaseous  $^{83\text{m}}\text{Kr}$  is an optimal candidate fulfilling these requirements [KAT04]. It offers several inner conversion electron lines with natural widths in the eV range. It is gaseous at conditions viable for KATRIN operation and can therefore be admixed to the tritium gas inside the WGTS. Also, it decays with a half-life of  $T_{1/2} = 1.83$  h [McC15] and therefore does not affect the tritium measurement mode. The energies of the conversion lines lie in the range of 5-35 keV which corresponds to the absolute energy scale that KATRIN is designed for, set by the tritium endpoint of  $E_0 \approx 18.6$  keV.

---

<sup>1</sup>The energy calibration makes up one of the 5 major systematics of KATRIN, to each of which a budget of  $\sigma_{\text{sys}} < 0.0075$  eV<sup>2</sup> is assigned. It can be calculated that Gaussian fluctuations of the potential difference should not exceed 60 meV [KAT04].

In case of the neutrino mass measurement the sub-eV sensitivity using a  $\approx 1$  eV energy resolution spectrometer can only be achieved by an accurate observation of the tritium  $\beta$  spectrum shape near the endpoint, requiring a high-activity source to reduce the statistical error. The same holds for the krypton-83m measurements, in which the activity of the krypton generating parent nuclide rubidium-83 may very well exceed 100 MBq [Vén+14]. The rubidium-83 has a half-life of  $T_{1/2} = 86.2$  d, which ensures a continuous supply of mesomeric krypton-83m during one measurement, without having to exchange or refresh the generator.

To enable these measurements, the gaseous source has to be driven in a different mode of operation, with the operational parameters, such as beam-tube temperature, differing from those of nominal  $T_2$  operation. This is discussed in section 3.1. For data analysis and simulation studies the expected krypton-83m conversion electron spectrum, which are measured by the main detector, has to be simulated, which requires an understanding of both the conversion spectrum and of the behaviour of the gaseous krypton inside the source. The modelling and implementation of these ingredients into the existing KATRIN simulation framework SSC are presented in section 3.2. Finally the usage of the krypton mode for investigation of systematics is discussed in section 3.3.

## 3.1. Operational Parameters of the Gaseous Source in $^{83m}\text{Kr}$ Mode

Ideally calibration measurements should be performed with comparable operational parameters as during neutrino mass data taking. In case of the krypton-83m mode this is, however, not possible due to several experimental constraints:

Previous experiments have determined that krypton measurements require temperatures of about 100 K for establishing significant observed integrated krypton-83m conversion electron rates [Bel+08]. The origin of this effect is not easily understood quantitatively, since it presumably can be attributed to the conductance of the krypton-containing pipes, which scales linearly with the mean pressure of the pipes and thus with the temperature [Pfe09]. Furthermore, krypton is expected to freeze out on the tube walls for too low temperatures, depending on the vapour pressure in the gas system. Most likely those effects are also relevant for the KATRIN krypton-83m mode measurements, which consequently requires significantly higher temperatures than the tritium mode measurements at about 30 K.

However, the two-phase neon cooling system, which is used in tritium mode, is only specified for temperatures between 27 K and 38 K, since at higher temperatures the maximal allowed pressure is exceeded. Therefore the coolant can be exchanged by argon, which is specified for a temperature range of 87 K to 118 K. It is still under discussion which temperature (or temperatures) will be used for the krypton-83m measurements. In this work it is taken to be 110 K.

Table 3.1.: **WGTS krypton-83m and tritium mode parameters.**

For the krypton-83m mode a higher operating temperature of the WGTS cryostat will be necessary. As a consequence, several other parameters concerning the gas can also differ from their nominal values. The specific operating values are not known yet.

parameter	nominal (tritium) mode	krypton + tritium mode
Temperature (K)	30	87-118, this work: 110
Injection pressure (mbar)	$3.4 \cdot 10^{-3}$	$\lesssim 12.6 \cdot 10^{-3}$
Column density ( $\text{m}^{-2}$ )	$5 \cdot 10^{21}$	$\lesssim 5 \cdot 10^{21}$
Tritium purity (%)	$\gtrsim 95$	$\gtrsim 95$

In this higher temperature regime an absolute calibration of the temperature sensors along the beam tube are not possible. This introduces an overall temperature uncertainty of about  $\sigma_{\text{sys}}(T) \lesssim 2 \text{ K}$ .

The higher beam tube temperature also directly influences the pressure profile inside the WGTS. For the laminar flow regime, which is applicable in the WGTS center, the pressure inside the source scales linearly with temperature, hence a factor of  $\approx 4$  in central WGTS pressure (injection pressure) is necessary to provide the standard tritium column density of  $\rho d_{\text{Tr}} = 5 \cdot 10^{21} \frac{1}{\text{m}^2}$ . The maximum achievable injection pressure is limited by the pumping system and the conductance of the pipes, while the latter is dominated by the injection capillary. Using a capillary with a larger diameter in krypton-83m mode allows for a higher gas throughput. Therefore it is assumed, that the nominal tritium column density or slightly less can be reached [Stu16].

Even for the same total column density, the shapes of the density profiles for different temperatures show slight deviations. This is even more important for the distribution of the krypton inside the source, since it is well known that a separation of tritium and krypton occurs [KS10].

Ultimately, in the normal tritium mode, the gas mixture is continuously purified in the permeators of the tritium laboratory, which would filter out the krypton. For this reason, parts of the tritium loop have to be bypassed, which also excludes the buffer vessel normally used for pressure stabilisation. How this affects the pressure and composition (purity) of the gas mixture can only be tested during measurements with krypton. The effect, however, is expected to be small, yet it might introduce systematics due to changes of the gas profile and the tritium purity.

It can be concluded that the findings in krypton mode require a transfer to tritium conditions, especially in the case when the investigated systematics are temperature dependent. Table 3.1 gives an overview of the source-related parameters in nominal tritium and in krypton-83m mode.

## 3.2. Modelling and Implementation

Following the discussion in section 2.2, the analysis of <sup>83m</sup>Kr conversion spectra to reveal WGTS-related systematic effects requires accurate simulations of the expected integrated rates. These simulations are carried out in the framework of the KATRIN analysis software *Source Spectrum Calculation* (SSC), which has been presented in section 2.2. SSC allows to perform a calculation of the integrated  $\beta$  spectrum according to equation 2.16. In the presence of krypton this equation is complemented by a <sup>83m</sup>Kr conversion electron spectrum and a krypton gas profile, such that it reads

$$\dot{N}(qU) = \sum_i^{\text{slices}} \epsilon_{\text{det}} \frac{\Omega_i}{4\pi} \int_{-\infty}^{\infty} \left\{ N_i^K \left( \frac{d\dot{N}}{dE} \right)_K + N_i^T \left( \frac{d\dot{N}}{dE} \right)_T \right\} R(E, qU + V_i) dE. \quad (3.1)$$

A model for the differential krypton-83m conversion spectrum  $\left( \frac{d\dot{N}}{dE} \right)_K$  has been added in this work, in the form of a new class *SSCKryptonSpectrum*. The corresponding modelling is discussed in section 3.2.1.

Furthermore, the number  $N_i^K$  and velocity of krypton-83m atoms in each slice  $i$  of the source has to be calculated. The required krypton-83m density and velocity profiles are calculated in the class *SSCGasDynamicsKrypton*. The corresponding modelling is addressed in section 3.2.2.

### 3.2.1. <sup>83m</sup>Kr Conversion Electron Spectrum

#### Process of Inner Conversion

A simplified decay scheme, which covers only the processes relevant for this work, can be seen in figure 3.1. A more detailed picture is provided for example in [McC15].

Excited krypton-83m is created by an electron capture process of the mother isotope rubidium-83 with an excitation energy of  $E_{\text{exc}} \approx 41$  keV. The deexcitation to the ground state involves an intermediate state, which splits the total excitation energy into a transition of  $E_{\text{exc}}^{32} \approx 32.2$  keV and  $E_{\text{exc}}^{9.4} \approx 9.4$  keV. Both transitions  $t$  can either occur via  $\gamma$  emission or inner conversion. In the latter case the excitation energy is transferred to one or more shell electrons through Coulomb interaction. In the case where  $E_{\text{exc}}^t$  exceeds the binding energy  $E_B^s$  of the electron in shell  $s \in \{K, L_1, M_{l_2}, N_{l_3}, \dots\}$  with sub shells  $l_i$ , it is emitted with a net kinetic energy of

$$E_{\text{kin}}^{t,s} = E_{\text{exc}}^t - E_B^s. \quad (3.2)$$

Hence, the energy of the emitted electron depends on the shell it originates from as well as on the involved transition energy. Therefore, several lines will be observed in a conversion spectrum, which conventionally are denoted as: *Shell*<sub>subshell</sub> Transition (i.e.  $K32$ ,  $L_19.4$ , ...).

The ratio of the emitted electron rate to the emitted photon rate is denoted as the conversion coefficient  $\alpha^{t,s} = \dot{N}_{e^-}^{t,s} / \dot{N}_\gamma^t$ . Thus, the decay rate  $\dot{N}_K^t$  of the excited krypton-83m by means of the transition  $t$  with half-life  $T_{1/2}^t$  can be written as follows, using the law of radioactive

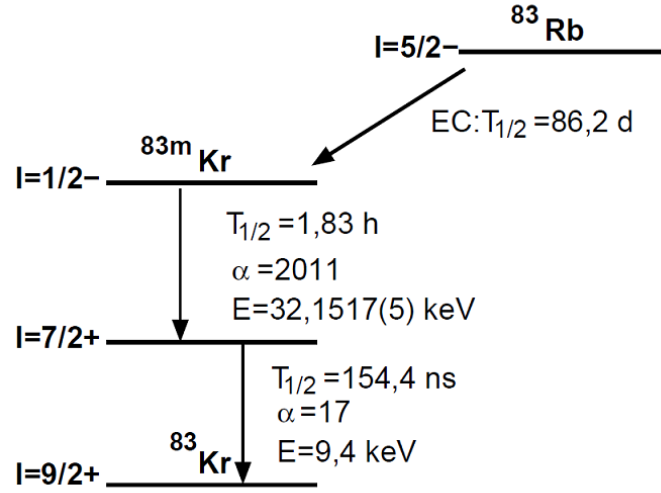


Figure 3.1.: Creation of the  $^{83\text{m}}\text{Kr}$  isomer and its deexcitation: The mother isotope  $^{83}\text{Rb}$  decays by electron capture to  $^{83\text{m}}\text{Kr}$ , which deexcitates to the ground state by  $\gamma$  emission or inner conversion, involving an intermediate state.  $I$  specifies the corresponding angular momentum and  $\alpha$  the conversion coefficient (diagram from [Ost08]).

decay:

$$\dot{N}_K^t = \frac{\ln 2}{T_{1/2}^t} \cdot N_K^t = \sum_s \dot{N}_{e^-}^{t,s} + \dot{N}_\gamma^t = \left( \sum_s \alpha^{t,s} + 1 \right) \dot{N}_\gamma^t. \quad (3.3)$$

It should be mentioned here that since the krypton-83m is already produced in a decay, the law for a chain of two decays should be expected for the krypton-83m conversion electron rate. This adds a time dependency, which either has to be considered in the total krypton amount in the source, or with a separate intensity parameter  $I$  (see discussion in section 4.2.3).

Using equation 3.3 for the  $t, s$ -electron production rate per krypton-83m atom, one obtains

$$A^{t,s} = \frac{\ln 2}{T_{1/2}^t} \frac{\alpha^{t,s}}{\sum_s \alpha^{t,s} + 1}. \quad (3.4)$$

Due to Heisenberg's uncertainty principle the lines of the spectrum are not completely monochromatic, but have a finite width  $\Gamma^{t,s}$ , with mean energy  $E_{\text{mean}}^{t,s}$  and an energy distribution function  $F(E, E_{\text{mean}}^{t,s}, \Gamma^{t,s})$ , which will be specified in equation 3.8. Summing up, the total electron conversion rate per krypton-83m atom and energy (i.e. the differential spectrum) is obtained as

$$\left( \frac{d\dot{N}}{dE} \right)_K (E) = I \sum_{t,s}^{\text{transitions shells}} A^{t,s} F(E, E_{\text{mean}}^{t,s}, \Gamma^{t,s}). \quad (3.5)$$

Thus, a krypton-83m conversion line is characterised by its conversion coefficient (or intensity), the line mean position and the line width.

There is a huge amount of experimental values available, stemming from different experimental techniques, for example in [Sev79; BB67; Des+03]. The values used in this work can be found in table 3.2. Furthermore, a probability  $p$  for shake up/off effects to occur is shown, which leads to a correction of the line intensities. This is discussed in the next paragraph.

The 9.4 keV transition is of secondary relevance for the KATRIN krypton-83m mode, since the corresponding conversion electron energies are much smaller than the tritium endpoint energy, resulting in a huge background due to tritium  $\beta$  electrons in combined measurements. Furthermore, the primary 32 keV transition can lead to an ionised state of krypton, while the low density conditions inside the WGTS lead to long neutralisation times. The secondary 9.4 keV transition is then sensitive to the electronic state of the krypton, resulting in multiple line structures [DS90]. Therefore the analysis of this work was restricted to the lines of the 32 keV transition. This eliminates the sum over the transitions in equation 3.5. Consequently, from here on the 32 in the nomenclature is left out for clarity.

### Shake up/off Effect

A way of describing the deexcitation of the krypton-83m atom under electron emission in the inner conversion process is the *sudden approximation*. Thereby the emission process is stated to be separable from the resulting change of the potential of the atom [War+91]. In this picture the emission of an electron can lead to an excitation of the electrons in the outer shells, either to a higher state (shake up) or to the continuum (shake off). In the first process the energy of the primary particles will be reduced by the excitation energy of the shake up electron, leading to a low-energy satellite line with the same shape as the main line. The second process, however, produces a low-energy tail of the satellite, since the excitation can be continuous in energy. For a correct modelling of these processes all the excitations in different shells have to be considered. This is not necessary for the KATRIN krypton-83m mode measurements, since all the satellite lines are separated from the main lines by more than 20 eV to lower energies, which means, that their shape does not contribute to an integrated measurement of the main lines [Hua10]. However, the amplitude of the main lines has to be corrected for the existence of the satellites, with the corresponding transition probabilities and mean energies shown in table 3.3. The satellites have been included with the same line shape  $F(E, E_{\text{mean}}^{t,s}, \Gamma^{t,s})$  as the main lines, which is discussed in the next paragraph.

Table 3.2.:  $^{83\text{m}}\text{Kr}$  conversion spectrum - main lines

The total energy of the transition, where the here considered conversion electrons originate from, is  $\approx 32$  keV. However, since they are emitted from different shells, which are denoted with the character in the symbol, their energy is not equal. This is the reason why there are different lines. The probability is used to correct for shake up/off effects. From here on, the identifier is left out for the sake of readability (values from [Wu01; Bam+72; Rös+78; CN73]).

Symbol	$E_{\text{mean}}/\text{eV}$	$\Gamma/\text{eV}$	$\alpha$	probability p in percent
$K32$	17824.2	2.71	475.99	79.5
$L_132$	30228.8	3.75	31.68	100.0
$L_232$	30422.6	1.25	494.16	82.2
$L_332$	30474.9	1.19	764.94	82.3
$M_132$	31871.5	3.50	5.20	100.0
$M_232$	31927.1	1.60	84.19	100.0
$M_332$	31936.0	1.10	130.15	100.0
$M_432$	32060.9	0.07	1.31	100.0
$M_532$	32060.9	0.07	1.84	100.0
$N_132$	32125.8	0.40	0.64	100.0

Table 3.3.:  $^{83\text{m}}\text{Kr}$  conversion spectrum - effective satellite lines

There is the probability of further electrons to be emitted in the process of internal conversion, due to the shake up/off effect. This leads to satellite lines, which are modelled to have the same width, conversion coefficient and line shape, as the original lines. A sum in the probability column indicates that there are in fact two separate transitions, which cannot be distinguished in a KATRIN krypton-83m mode measurement. The denotation with  $S1$ ,  $S2$ ,  $S3$  is purely phenomenological (values from [CN73]).

Symbol	$E_{\text{mean}}/\text{eV}$	probability p in percent
$K^{S1}$	17664.18	1.43 + 2.13
$K^{S2}$	17781.00	1.80
$K^{S3}$	17805.12	4.39 + 9.06
$L_2^{S1}$	30262.58	1.42 + 2.14
$L_2^{S2}$	30379.40	1.53
$L_2^{S3}$	30403.52	3.86 + 8.13
$L_3^{S1}$	30314.88	1.41 + 2.12
$L_3^{S2}$	30431.70	1.52
$L_3^{S3}$	30455.82	3.84 + 8.10

### Line Shape Modelling

Krypton conversion electrons have a Lorentzian energy distribution  $L(E, E_{\text{mean}}, \Gamma)$ , corresponding to a modelling as a driven, damped oscillator [BW36; WW30]

$$L(E, E_{\text{mean}}, \Gamma) = \frac{1}{\pi} \frac{\Gamma/2}{(\Gamma/2)^2 + (E - E_{\text{mean}})^2}. \quad (3.6)$$

Here  $E_{\text{mean}}$  is the line mean position and  $\Gamma$  the line width. When dealing with Gaussian fluctuations of the potential and Gaussian broadenings due to Doppler effect, it is common to introduce the convolution of the Lorentzian with a Gaussian kernel  $G(E, E_{\text{mean}}, \sigma_g)$  of width  $\sigma_g$  [Bel+08]

$$G(E, E_{\text{mean}}, \sigma_g) = \frac{1}{\sqrt{2\pi}\sigma_g} e^{-\frac{(E-E_{\text{mean}})^2}{2\sigma_g^2}}. \quad (3.7)$$

The resulting profile is the so-called Voigt profile

$$V(E, E_{\text{mean}}, \Gamma, \sigma_g) = \int_{-\infty}^{\infty} G(\tau, E_{\text{mean}}, \sigma_g) L(E - \tau, E_{\text{mean}}, \Gamma) d\tau. \quad (3.8)$$

### Implementation in This Work

Summing up the previous paragraphs, the following representation of the differential krypton-83m conversion spectrum has been implemented in this work:

$$\left(\frac{dN}{dE}\right)_K(E) = I \cdot A^{32} \sum_l^{\text{satellites}} \frac{\alpha^l}{\sum_s \alpha^{32,s} + 1} \frac{p^l}{100} V(E, E_{\text{mean}}^l + E_{\text{shift}}, \Gamma^l, \sigma_g). \quad (3.9)$$

Here  $I$  is a fit parameter for the intensity, which by default is set to 1.

The total rate of the 32 keV-transition is  $A^{32} = \frac{\ln 2}{1.83\text{h}} = 1.05 \cdot 10^{-4} \frac{1}{\text{s}}$  per krypton atom.

The values for the  $\alpha^l$ ,  $p^l$ ,  $E_{\text{mean}}^l$  and  $\Gamma^l$  can be found in tables 3.2 and 3.3.

For the sum of the conversion coefficients, the value  $\sum_s \alpha^{32,s} = 2011$  [Rös+78] is taken. This does not correspond exactly to the sum in tables mentioned above: the difference is due to unaccounted lines and measurement uncertainties. It should be stressed that this only affects the measured intensity, which is a free fit parameter. Furthermore, for systematic studies of the WGTS plasma the line parameters have to be determined in pre-tritium measurements, when no plasma effects are expected. Thus, the corresponding estimates replace the above literature values.

To account for line shifts, an energy offset  $E_{\text{shift}}$  is added, which by default is set to 0. The same holds for the Gaussian width  $\sigma_g$ , which accounts for line broadenings. These parameters are used in section 4.1.1 to model source plasma potential-induced effects.

Since  $\sigma_g$  enters the Gaussian convolution kernel quadratically (with exception of the normalisation), it is expected, that  $\sigma_g^2$  is a normal-distributed fit parameter. A continuation to the regime of negative squares is performed, using the method of [Bel+08].

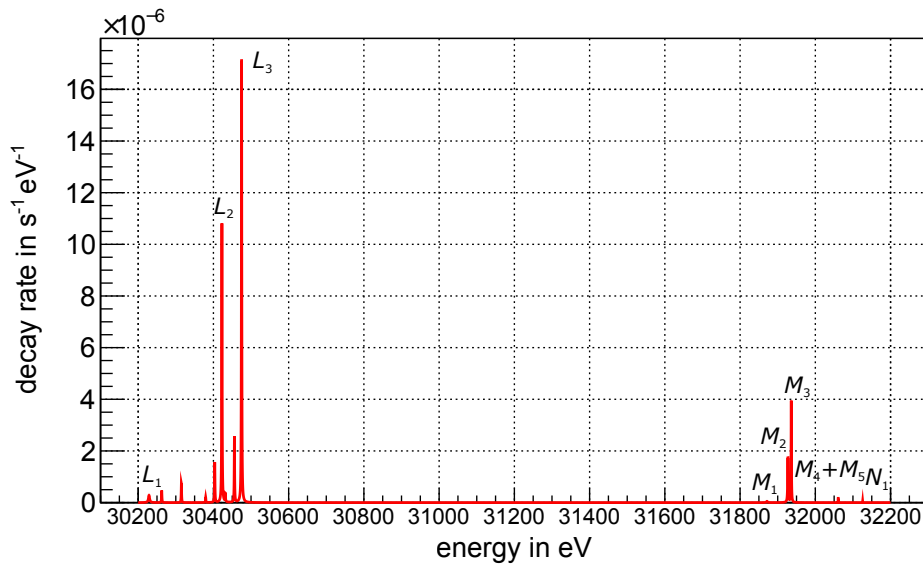


Figure 3.2.: Differential krypton-83m conversion electron spectrum:  $L$ ,  $M$  and  $N$  conversion lines and the corresponding shake off/up lines are shown, which were calculated using equation 3.9 and the values in tables 3.2 and 3.3. The shown rate is per atom.

Figure 3.2 shows the implemented conversion lines, with the exception of the  $K$  line. Figure 3.3 shows the corresponding integrated spectrum.

In figure 3.4 a close-up on the  $L_2$  and the  $L_3$  line region of interest can be seen. Due to energy loss by inelastic scattering of the electrons off the gas inside the WGTS extra steps can be observed in the spectrum. This has important implications for the krypton-83m measurements, which is discussed in chapter 4.

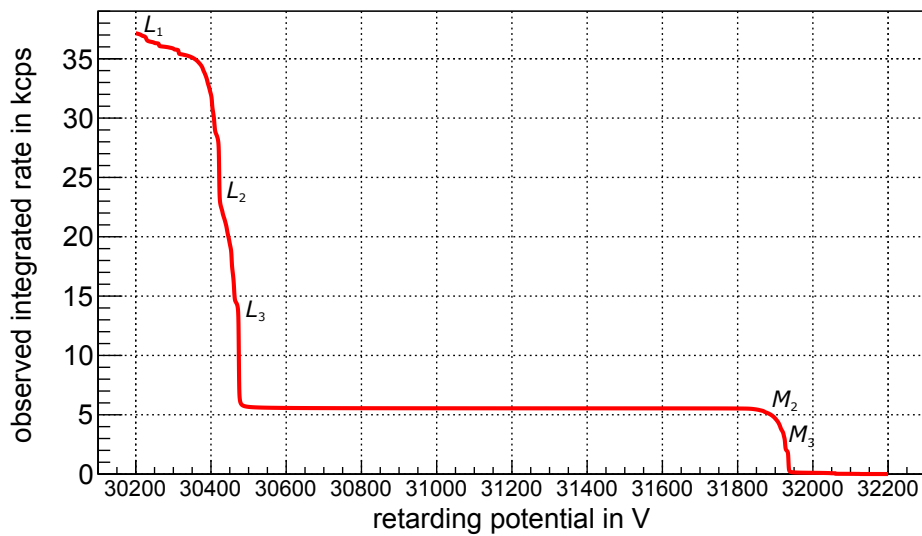


Figure 3.3.: Integrated krypton-83m conversion electron spectrum: The krypton column density is  $5.5 \cdot 10^{11} \frac{1}{\text{m}^2}$ , corresponding to an injection concentration of  $10^{-10}$ . The  $M_1$ ,  $M_4$ ,  $M_5$  and  $N_1$  krypton-83m conversion lines are not visible for this configuration and scale and the tiny additional steps are due to shake up/off effects.

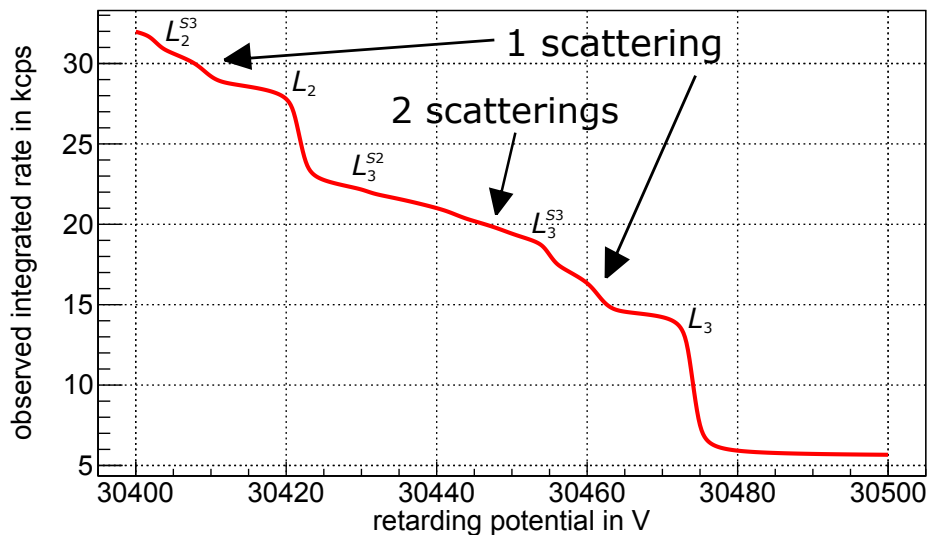


Figure 3.4.: Close-up on a region of interest around the integrated krypton-83m  $L_2$  and  $L_3$  conversion electron lines: On this scale, the steps due to shake up/off lines are clearly visible. Due to energy loss by inelastic scattering off the gas inside the WGTS, several additional steps can be observed, which are also indicated.

### 3.2.2. <sup>83m</sup>Kr Gas Dynamics

#### Density Profile

Most of the theoretical work for the WGTS krypton density profile has been done in [KS10], which describes the calculation for several gas mixtures inside the WGTS. The procedure is reviewed here briefly.

As for the tritium gas dynamics, the basic procedure is solving the linearised Boltzmann equation. This is necessary since inside the WGTS a transition from the hydrodynamic to the molecular flow regime occurs, which prohibits the usage of common approximate equations for gas dynamics. Hence, the following equation for the dimensionless gas throughput  $J_\alpha$  of gas species  $\alpha$  has to be solved numerically:

$$J_\alpha \propto \sum_{\beta=1}^s G_{\alpha\beta}(z) \frac{n_\alpha(z)}{n_\beta(z)} \frac{dn_\beta}{dz}(z). \quad (3.10)$$

$J_\alpha$  is proportional to the gas throughput of species  $\alpha$ , which is a constant of the respective vacuum system (here the WGTS). The  $G_{\alpha\beta}(z)$  are coefficients from the collision integral, describing the actual interactions between the particles. These have been calculated in [KS10], where interpolating formulas are given.  $n_\alpha(z)$  denotes the number density profile of species  $\alpha$ .  $z$  is taken to be the coordinate along the WGTS axis (0 is the point of injection). In general, also the interactions between walls and particles and temperature gradients could be taken into account, which is actually the case for the tritium gas profile.

The density gradients of all the gas species affect each other mutually. For krypton, however, a major simplification can be made: the concentration of krypton inside the WGTS will always be very small compared to the other gases considered<sup>2</sup>. In the case of a tritium-krypton mixture this means that the influence of krypton (K) on tritium (T) is negligible in terms of particle interactions. Hence,  $G_{TK}$  is set to zero. This also justifies disregarding krypton-wall interactions and temperature gradient-driven influences on the krypton profile, since it is strongly dominated by krypton-tritium interactions. Consequently, the tritium density profile  $n_T(z)$  can be calculated in a first step, which has mainly been implemented by [Höt12].

Secondly, the krypton density profile is obtained by numerically integrating the following differential equation:

$$\frac{dn_K^*}{dz} = -\frac{1}{G_{KK}(z)} \left( \frac{1}{L_{WGTS}} + G_{KT} \frac{n_K^*}{n_T} \frac{dn_T}{dz} \right). \quad (3.11)$$

Here  $n_2^*$  is proportional to the krypton number density and  $L_{WGTS} \approx 10$  m is the length of the WGTS. As can be noticed, there is no dependency on the total krypton amount at all. This is due to the low krypton density limit. The amount of krypton only enters by

<sup>2</sup>The actual krypton concentration during krypton-83m measurement runs can only be predicted within several orders of magnitude (see chapter 4.2.3) at this point. Even in the most generous case the ratio of krypton atoms to tritium molecules does not exceed  $10^{-6}$ , which satisfies the low density limit.

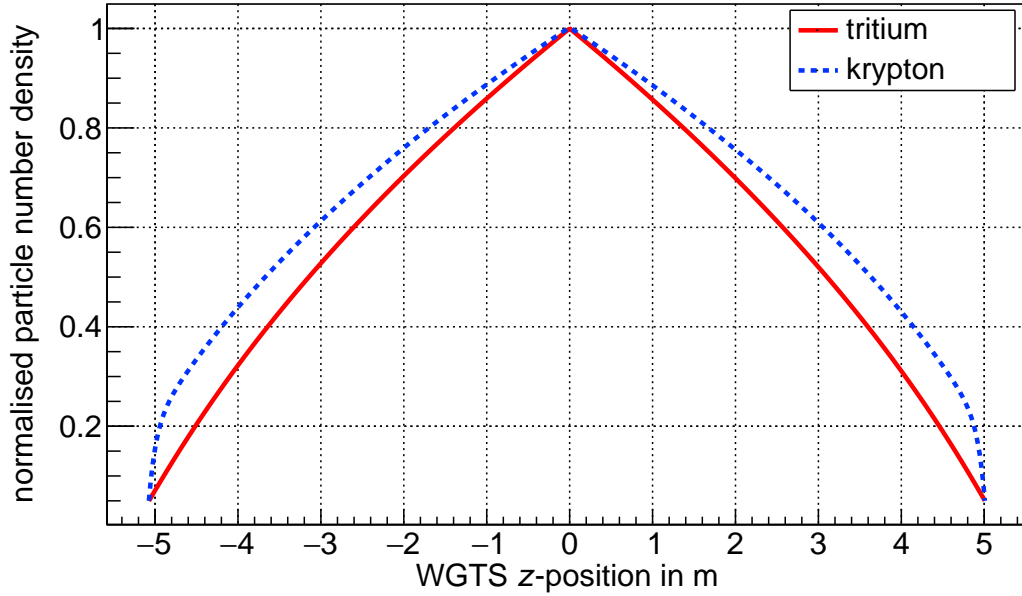


Figure 3.5.: Tritium and krypton gas profiles for  $T = 110$  K, normalised to injection density: Due to the mass difference, the relative krypton concentration is enhanced towards the WGTS ends.

scaling the resulting gas profile in the following way:

$$n_{\text{K}}(z) = n_{\text{K}}(0) \frac{n_{\text{K}}^*(z)}{n_{\text{K}}^*(0)}. \quad (3.12)$$

### Implementation in This Work

Since the front and rear parts of the WGTS are not of equal length, the calculation is carried out for every part separately. Equation 3.11 is numerically integrated by a *RungeKutta4* algorithm with fixed step width. For the boundary condition a reduction factor  $r_p := \frac{p_{\text{out}}^*}{p_{\text{in}}^*}$  of the krypton partial pressures is introduced, which is determined by the pumping system. This affects the krypton gas profile only at the WGTS ends, since for the most part it is dominated by the tritium density profile. Since  $r_p$  depends on the first integration step  $n_{\text{K}}^*(L_{\text{WGTS}})$  and the last step  $n_{\text{K}}^*(0)$  the integration has to be carried out several times to match the given ratio of those two values.

The tritium viscosity  $\mu_{\text{Tr}}$  has to be adjusted for the higher temperatures. Since no experimental data for tritium is available, it is obtained according to the procedure detailed in [Sha03]. Consequently, the value for hydrogen<sup>3</sup> can be scaled with the tritium mass, yielding

$$\mu_{\text{Tr}} = \sqrt{\frac{m_{\text{Tr}}}{m_{\text{H}}}} \cdot \mu_{\text{H}} = \sqrt{3} \cdot 4.313 \cdot 10^{-6} \frac{\text{kg}}{\text{m} \cdot \text{s}} = 7.47 \cdot 10^{-6} \frac{\text{kg}}{\text{m} \cdot \text{s}}. \quad (3.13)$$

<sup>3</sup>Taken from [AMW86], hydrogen, 110 K

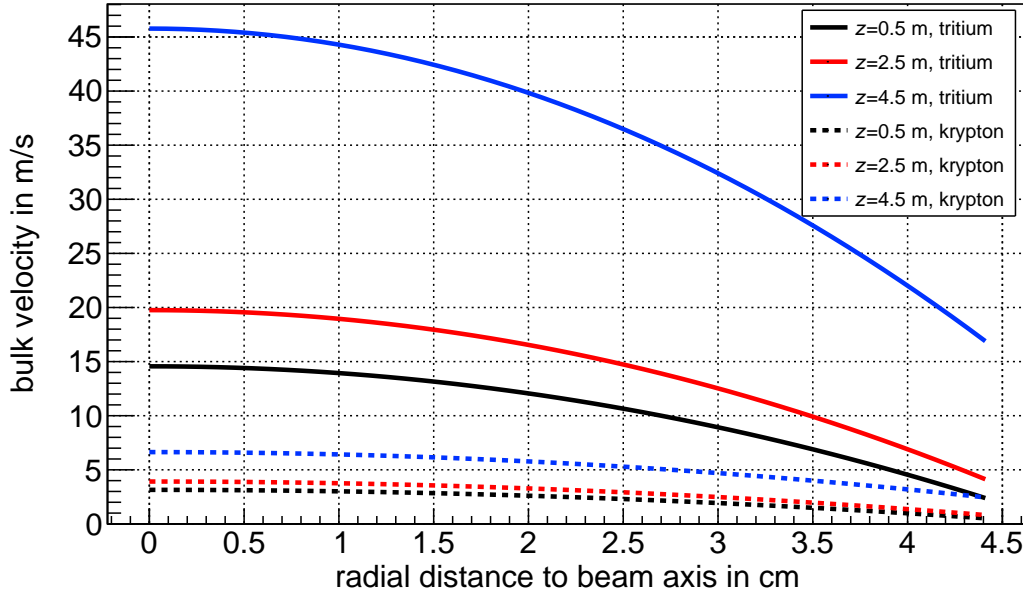


Figure 3.6.: Tritium and krypton bulk velocity profiles for  $T = 110$  K: Due to the  $\approx 14$  times larger mass, the bulk velocity of krypton is approximately  $\sqrt{14}$  times lower than that of tritium molecules. A further influence is the difference of the gas profiles.

Thus, the rotation spectrum is assumed to be the same for  $H_2$  and  $T_2$  at 110 K.

As a result of numerical integration discrete densities are obtained, which are linearly interpolated. The total amount of krypton can be specified in two ways: either the total krypton column density, or the krypton injection concentration can be given (at  $\vec{r} = \vec{0}$ ). This should not be mistaken for the overall krypton concentration (i.e. the ratio of krypton and tritium column densities), which is a slightly different number, due the different shape of the density profiles. This can be seen in figure 3.5, where a tritium and a krypton gas profile are compared. Here, the well-known demixing due to difference in masses is observed.

For the krypton bulk velocity  $v_z$  the following equation is used [Höt12]:

$$v_z = -v_0 \cdot \frac{R}{n_K} \frac{dn_K}{dz} \left( A - C \frac{r^2}{R^2} \right). \quad (3.14)$$

Here,  $v_0$  is the thermal velocity of krypton,  $R$  the radius of WGTS and  $r$  the radial coordinate.  $A$  and  $C$  are pressure dependent parameters from theory already implemented for tritium, which are independent of the gas species. The resulting bulk velocity profiles can be seen in figure 3.6.

The integration of equation 3.11 only depends on the used tritium density profile and is also valid for non-zero radii  $r \neq 0$ . Hence, 3D calculations of the krypton density can be carried out for all the positions inside the WGTS where a tritium profile is available. The procedure for tritium is described in [Höt12]. It involves the construction of the 3D

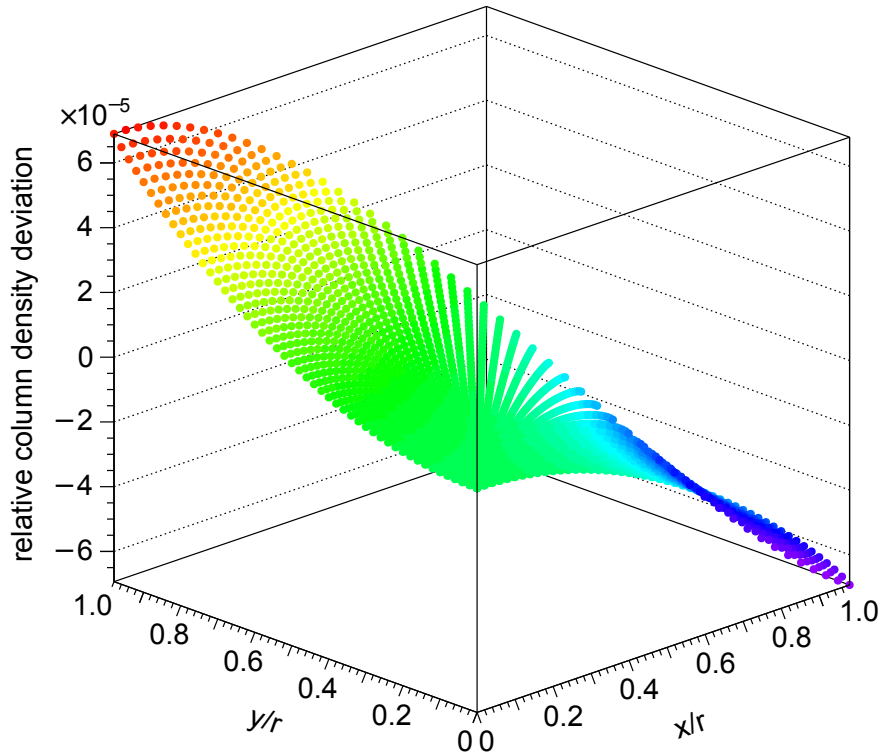


Figure 3.7.: Relative column density deviation of krypton  $\frac{\Delta\rho d_{\text{Kr}}}{\rho d_{\text{Kr}}(r=0)}$  in radial direction: A temperature profile was used along the  $z$ -axis of the WGTS, which is based on a test measurement described in [Höt12]. The maximum temperature difference is  $\Delta T_{\text{max}} = 0.5 \text{ K}$  and the central temperature is  $T = 110 \text{ K}$ . This leads to a maximum deviation of the total krypton column density of  $7 \cdot 10^{-5}$  compared to the central value.  $r = 45 \text{ mm}$  is the radius of the WGTS beam tube.

tritium profiles out of pre-calculated 2D slices for different parts inside the WGTS beam tube, which are related to various pressures.

If the standard tritium column density of  $5.0 \cdot 10^{21} \frac{1}{\text{m}^2}$  is assumed in krypton mode ( $T = 110 \text{ K}$ ), an approximately 4 times larger mean pressure inside the WGTS has to be achievable. For such high pressures additional 2D slices had to be calculated and added. This enables 3D calculations both for tritium and krypton densities. The radial deviations of the total column density of krypton from the central value at  $r = 0$  are shown in figure 3.7.

Summing up, a full implementation of krypton gas dynamics has been realised in this work which can handle two-dimensional as well as three-dimensional profiles both for density and velocity. This enables the data analysis of systematic studies performed in krypton mode, which are discussed in the next section.

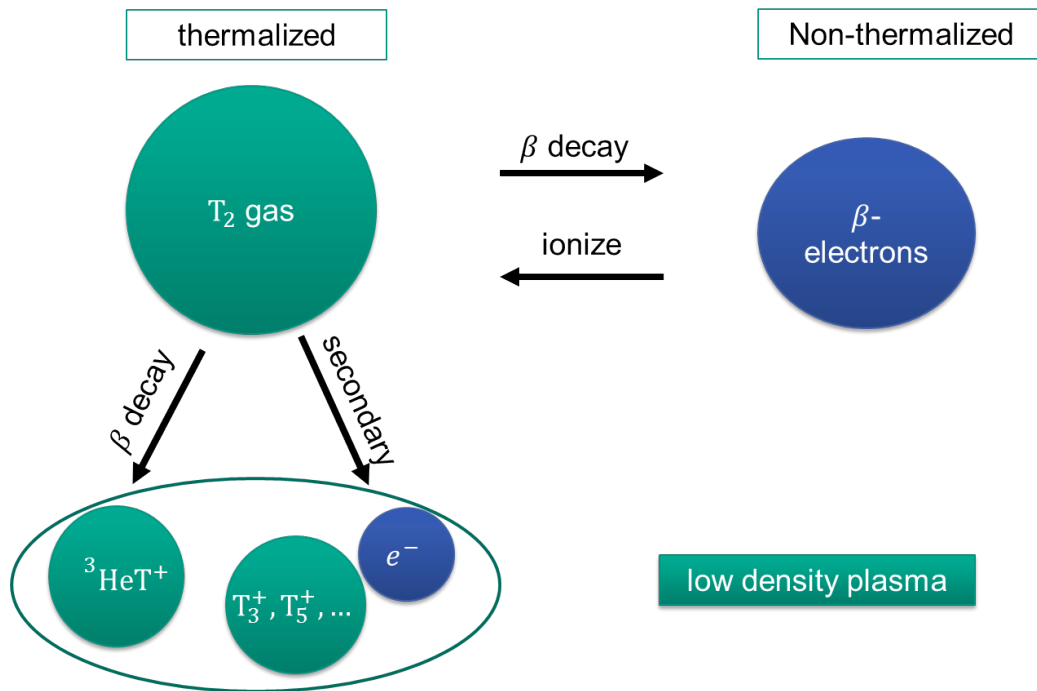


Figure 3.8.: Plasma formation inside the WGTS: Due to scattering off gas molecules every  $\beta$  electron on average creates 15 pairs of ions and secondary electrons. Since all charged particles are confined to magnetic field lines, neutralisation at the walls is strongly suppressed. With the exception of the fast  $\beta$  electrons, all charged particles are partially thermalised and leave the WGTS only with the pumping speed. This leads to a comparatively long mean pump out time of  $\approx 1$  s and to the formation of a low density-plasma.

### 3.3. Systematic Studies with the $^{83m}\text{Kr}$ Mode

#### Plasma Potential of the Source

It is expected that the conditions inside the WGTS during tritium measurements produce a low-density plasma [KAT04]. The contributing particles and processes can be seen in figure 3.8:  $\beta$  decay creates  $10^{11}$  electrons and  $^3\text{HeT}^+$  molecules per second. Most of the electrons are reflected at the retarding potential of the spectrometer section, therefore traversing the WGTS two times while scattering off gas molecules. The scattering on average creates 15 pairs of secondary electrons and ions. Together with the primary particles emitted in  $\beta$  decay, this makes for  $\text{T}^+$ ,  $\text{He}^+$ ,  $^3\text{HeT}^+$  and  $\text{T}_2^+$  ions, while due to chemical reactions and clustering further ions ( $\text{T}_3^+$ ,  $\text{T}_5^+$  and higher) are created. Due to the confinement of charged particles to the magnetic field lines they cannot neutralise at the walls, but only leave the WGTS source tube at its ends. Hence, for all charged particles with the exception of the high-energy  $\beta$  electrons a partial thermalisation is expected, leading to a pump out time of  $\approx 1$  s, strongly influenced by the gas dynamics. It has been estimated in simulations that the secondary electrons for the most part neutralise the

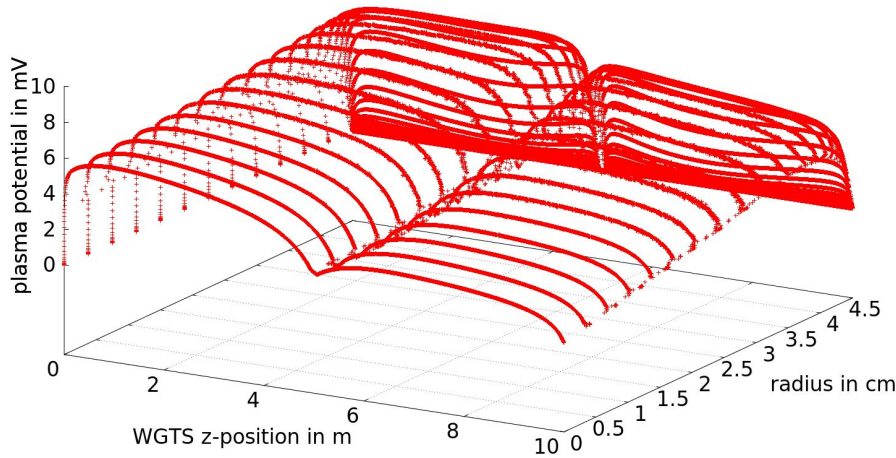


Figure 3.9.: Simulated plasma potential inside the WGTS for 30 K: Rear and tube walls are set to zero potential, which is visible as a steep drop of the plasma potential in the corresponding regions. The dip at  $z = 5$  m can be attributed to the gas injection point of the WGTS (data from [Kuc16]).

positive charges, leading to a quasi-neutral plasma with a small positive space charge. This neutralisation can only occur if no additional heating mechanism prevents the cooling of the secondary electrons. In the latter case, or if the number of low-energy electrons is not sufficient to neutralise the positive charges, additional electrons can be provided by photo emission from the rear wall. The absolute value of the potential depends on the boundary conditions, hence the potential of the rear wall or the tube walls. It is expected, however, that the tube walls have a minor influence, since they are parallel to the magnetic field lines and thus lateral charge transport is strongly suppressed. The potential of the rear wall can be set independently to compensate for work function differences of the rear wall (gold) and tube walls (stainless steel) and to test for the influence of the wall on the plasma potential.

A detailed understanding of the plasma formation and its properties requires a simulation of the energy distributions of the particles, neutralisation and scattering processes and gas dynamics. This work has been carried out in [Kuc16]. A resulting potential with the approximation of axial symmetry can be seen in figure 3.9. As expected, the potential is related to the gas profile inside the WGTS, while at the centre a dip due to the outgoing gas flux at the gas injection can be seen. The rear wall of the WGTS ( $z = 0$  m) as well as the side tube walls ( $r = 4.5$  cm) have been set to zero potential. Due to the higher mobility of the electrons compared to the positive charges, the formation of positive charged regions in front of the walls is expected, which leads to a step increase of the potential. Since the source is windowless at the front side ( $z = 10$  m) no grounding is observed. It should be noted that the research of the behaviour of ions in the front side transport system is still ongoing and might reveal additional effects [KAT04].

Due to the partition of the detector into 148 pixels, radial inhomogeneities in the beam line can be observed and taken into account during analysis. The outmost parts of the magnetic flux can even be excluded from the analysis in order to avoid boundary effects. However, even the measurement of an individual pixel always represents an average over one magnetic field line, in particular over the electron spectra of the 10 m long WGTS  $z$ -profile. Due to the non-vanishing potential, the spectra at different  $z$ -positions are shifted with respect to each other in energy, leading to a shape distortion of the  $z$ -integrated spectrum. If the plasma potential is not taken into account, it is expected that the estimate on the tritium endpoint is shifted according to the mean of the potential, while the inhomogeneity dominantly produces a systematic error of the neutrino mass measurement, which is taken into account with  $|\sigma_{\text{syst}}(m_\nu^2)| < 0.2 \cdot 10^{-3} \text{ eV}^2$  in the KATRIN systematics budget (table 2.1).

For the 30 K simulation of the potential shown in figure 3.10 the resulting neutrino mass shift is  $\sigma_{\text{syst}}(m_\nu^2) = -0.3 \cdot 10^{-3} \text{ eV}^2$ , which does not stay in the projected limit. Thus, a quantification of the size of the WGTS plasma potential is imperative and can be provided by the krypton-83m mode. This has been successfully demonstrated by the Troitzk neutrino mass experiment, which also uses a gaseous source [Bel+08]. Since the plasma formation inside the source is driven by  $\beta$  decay, a krypton-83m conversion spectrum measurement of pure krypton compared to a mixture of krypton and tritium reveals plasma-related effects on the krypton-83m conversion electron energy spectrum. In particular, the krypton-83m lines are shifted and broadened according to mean and inhomogeneity of the potential. It is assumed, that shift and broadening can be related to a systematic shift of the tritium endpoint and neutrino mass.

To do so, one has to respect the scaling of the WGTS potential with temperature, since the krypton-83m mode measurements have to be carried out using a significantly higher temperature than the tritium  $\beta$  endpoint measurements (see section 3.1).

A simulation for the potential for tritium and krypton-83m mode temperature (30 K and 110 K, respectively) in the centre of the WGTS can be seen in figure 3.10. The inhomogeneities measured minimum to maximum increase by a factor of  $\approx 4$ , which coincides with the expectation of a linear temperature behaviour. The effect of the expected plasma in krypton-83m mode on the krypton-83m  $L_3$  conversion line can be seen in figure 3.11. To produce effects visible by eye it has been scaled with a factor of 100, such that a clear line broadening is observed. The line mean has been corrected for the potential-induced overall shift of  $E_{\text{shift}} = 1.9 \text{ eV}$ .

The actual plasma effects are expected to be much smaller, which requires for an efficient and accurate modelling and analysis of the krypton-83m line shape distortion and shift. This is the main topic of this work and the subject of chapter 4. Beyond that it should be stressed that not only plasma effects, but every external systematic affecting the  $\beta$  electron energy is ultimately visible in the krypton-83m spectrum, such that the krypton-83m mode provides a unique tool of understanding the experimental setup.

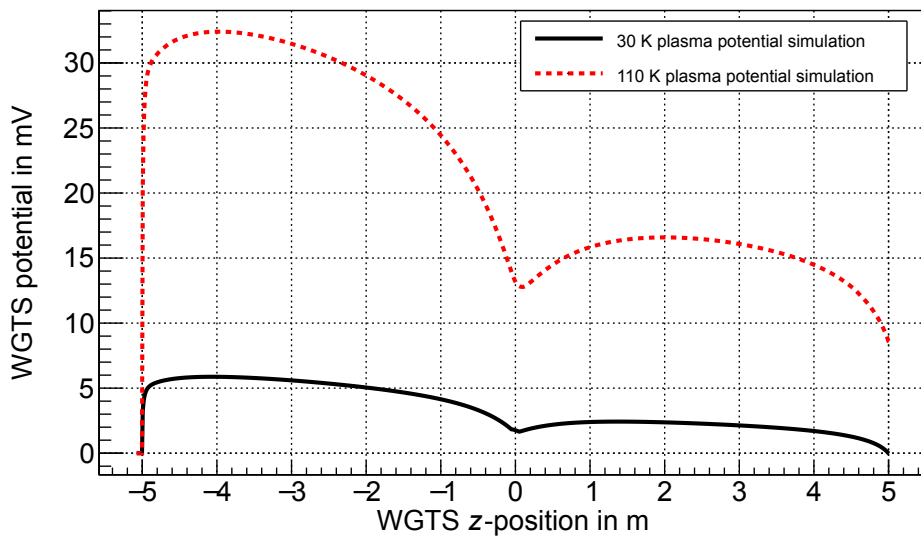


Figure 3.10.: Simulated  $z$ -profile of the central plasma potential inside the WGTS for 30 K (black) and 110 K (red). The total differences are  $\approx 5$  mV and  $\approx 20$  mV. This is in agreement with the expectation from the KATRIN design report, which states a linear scaling of the inhomogeneity with temperature (data from [Kuc16]).

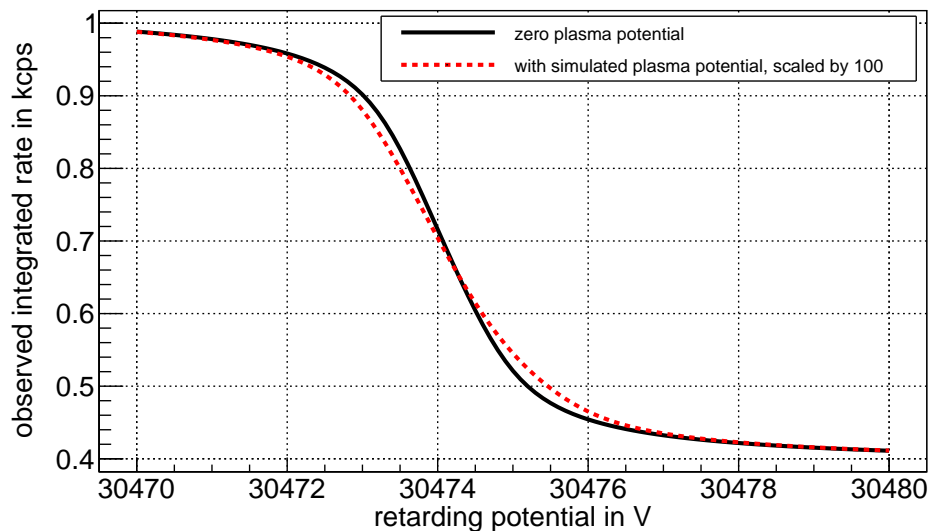


Figure 3.11.: Effect of the WGTS plasma potential on the krypton-83m  $L_3$  line: When including the simulated plasma potential an artificial line broadening can be observed. The potential is scaled by a factor of 100 for better visibility by eye. This leads to a shift of the line mean of  $E_{\text{shift}} = 1.9$  eV, which has been corrected.

## 4. Simulation Studies of the $^{83\text{m}}\text{Kr}$ -Mode Sensitivity on the Tritium Source Plasma Potential

As motivated in chapter 3, the krypton-83m mode of the WGTS offers the possibility of the analysis of systematic effects on the KATRIN neutrino mass measurement. In particular it is the only proposed way to study plasma potential inhomogeneities of the WGTS, discussed in section 3.3. The corresponding limit of the induced neutrino mass shift is required to be  $\Delta m \leq 2 \cdot 10^{-4} \text{ eV}^2$  [KAT04], which corresponds to a maximum of 10 mV inhomogeneities, in the case where they can be assumed to be Gaussian (table 2.1).

The objective of this work is to perform sensitivity studies of the krypton-83m mode on the WGTS plasma potential under expected KATRIN measurement conditions. This is done utilising the KATRIN software packages SSC and KaFit which are described in section 2.2.2 (general introduction) and in section 3.2, respectively (add-ons required for this work).

Since the potential is not a constant scalar but an unknown scalar function of the WGTS coordinate  $\vec{r}$ , it has to be described by parameterised models, which can be subjected to the sensitivity analysis. The modelling of the potential and its influence on the measured integrated krypton-83m conversion electron spectrum is discussed in section 4.1.

This is followed by the identification of reasonable operational parameter settings in section 4.2, which for example includes the discussion of the choice of available krypton-83m conversion lines, the measurement time distribution and the tritium column density that is used during these specific measurements.

An important process, which grants basic access to the axial position of an electron's origin within the  $\approx 10$  m long beam tube of the WGTS, is inelastic scattering. The underlying principle is the relation of certain parts of the integrated spectrum to certain origins of the electrons inside the WGTS, by exploiting the  $z$  dependency of the scattering probabilities. This is discussed in section 4.3.

The studies are divided into two parts, reflecting the two general influences on the sensitivity: a statistical and a systematic analysis. This follows the discussion presented in section 2.2. For both cases a minimisation of the  $\chi^2$  function with respect to the free model parameters is carried out by KaFit, where both the toy measurement data  $\dot{N}_{\text{exp}}$  and the expected result  $\dot{N}_{\text{theo}}$  are generated using SSC.

- **Statistical analysis:** The exact same experimental configuration to generate the toy measurement and the expectation are provided to SSC. Consequently, the resulting

error on a model parameter can be interpreted as the mere statistical uncertainty. The results are presented in section 4.4.

- **Systematic analysis:** One of the input parameters (for example the WGTS temperature) is arbitrary varied from its nominal value, while keeping all other conditions unchanged. This will be reflected in a shift of the estimate of a free parameter, which can be interpreted as the induced systematic uncertainty. This is presented in section 4.5.

Based on the results obtained in section 4.4 and 4.5 this chapter is concluded with a discussion of the general possibilities of the krypton-83m mode and the impact of the corresponding measurements on the KATRIN neutrino mass measurement in 4.6.

## 4.1. Discussion of the Source Plasma Potential and its Modelling

A main difficulty when studying the sensitivity of the krypton-83m mode on the WGTS plasma potential  $V$  is, that the latter is an unknown function of the WGTS coordinate  $\vec{r}$ . Consequently, the sensitivity can only be studied on the parameters of phenomenological models of the potential.

In this work two different approaches for these models have been chosen: The Voigt profile, which is presented in section 4.1.1, describes the effect of the plasma potential on the krypton-83m conversion electron spectrum by introducing an effective, broadened spectrum, without making any assumptions on the actual plasma potential shape.

In contrast, in the ellipse model (section 4.1.2) and the polynomial model (section 4.1.3) a distinct shape of the plasma potential is assumed in dependency of some free model parameters, and the effect of the corresponding potentials on the krypton-83m conversion electron spectrum is calculated using SSC.

In an actual krypton-83m measurement the observables are integrated count rates at different retarding potentials, thus an integrated spectrum. However, the full information on the complex shape of the plasma potential is in general no longer contained in this spectrum and only a simplified model can be probed. As a consequence the model parameter estimates of an actual measurement are not necessarily equal to the model parameter estimates theoretically obtainable by a direct fit of the more complex input plasma potential. To quantify this effect the plasma potential simulation presented in figure 3.10 for 110 K is included in the studies as null hypothesis. This allows to compare the parameter estimates obtained in a direct fit to those obtained in a krypton-83m mode measurement. One of the findings of this work is that those values are in principal not identical, the reason of which is discussed in 4.6.2.

The parameters which are obtained in krypton-83m mode measurements have to be translated to tritium  $\beta$  measurement conditions, respecting the different potentials due to the different operating temperatures. This translation has to rely on plasma potential

simulations, presented in [Kuc16]. The present work is focused on the determination of the parameters in krypton-83m mode.

### Radial Dependency of the Potential

As it is shown in section 3.2.2 the total column density of krypton and tritium shows only minor radial variations in the range of  $10^{-5}$ , which translates to the same order of radial differences in integrated count rates. For the calculation of statistical sensitivities these differences are negligible and consequently the calculations are carried out by using one dimensional gas dynamics. For systematic studies the bulk velocity has to be considered. Since it takes its maximum values at  $r = 0$  and decreases towards the beam tube walls, calculations with  $r$  fixed at 0 are an upper limit on any possible systematic effects.

Thus, the calculations made in this work describe the WGTS as a homogeneous system in radial direction with density and bulk velocity profiles for  $r = 0$ . The integrated rates which are considered are the total rates over all 148 detector pixels. If a pixelwise analysis is favoured, it is perfectly valid to scale the integrated rates according to the sensitive areas of the pixels.

This allows for the major simplification of only considering the  $z$  dependency of the plasma potential, where the radial dependencies can be studied in a pixel- or ringwise analysis.

#### 4.1.1. Voigt Profile of the $^{83\text{m}}\text{Kr}$ Conversion Electron Lines

One way of modelling the influence of the plasma potential on the krypton-83m conversion spectrum is the Voigt profile (see implementation presented in chapter 3.2.1). It is described by a Gaussian broadening parameter  $\sigma_g$  and a line shift  $E_{\text{shift}}$ . The influence of this parameters on the krypton-83m  $L_3$  line is pictured in figure 4.1 and figure 4.2, respectively.

The basic idea in using the Voigt profile, which is stated in the design report [KAT04], is to relate the obtained  $E_{\text{shift}}$  to a shift of the tritium  $\beta$  spectrum endpoint  $E_0$  and the normal broadening  $\sigma_g$  to a systematic shift of the neutrino mass  $m_\nu$ . However, this procedure involves four major assumptions:

First, the potential induced line shift  $E_{\text{shift}}$  has to be interpretable as a mean potential  $\langle V \rangle$  and  $\sigma_g$  as a measure of the inhomogeneity of the potential  $\sigma(V)$ :

$$e \langle V \rangle \propto E_{\text{shift}} \quad \text{and} \quad e \sigma(V) \propto \sigma_g . \quad (4.1)$$

$e$  is the elementary electric charge. Naively, the constants of proportionality are one and the mean potential is just the integral with respect to  $z$  over the length  $L_{\text{WGTS}}$  of the WGTS. The latter leads to the following form of the standard deviation

$$\sigma^2(V) = \langle V^2 \rangle - \langle V \rangle^2 = \int \frac{dz}{L_{\text{WGTS}}} V(z)^2 - \left( \int \frac{dz}{L_{\text{WGTS}}} V(z) \right)^2 . \quad (4.2)$$

Values for mean and standard deviation following the above definition can be found in figure 4.3.

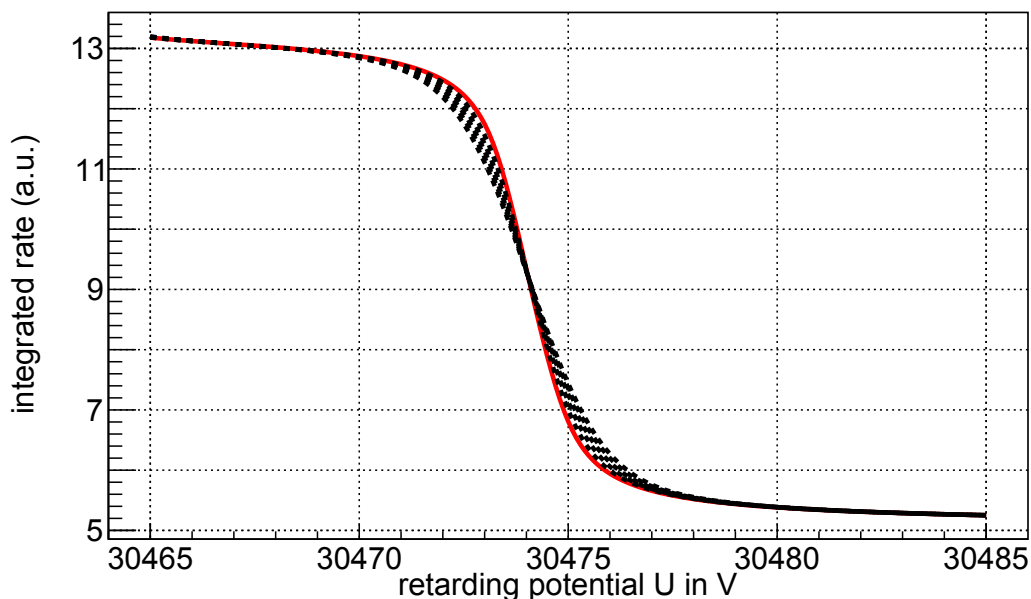


Figure 4.1.: Effect of a Gaussian broadening of the krypton-83m  $L_3$  conversion line with standard deviation  $\sigma_g$ : The original line width is  $\Gamma = 1.19$  eV (red, continuous line) and an interval of  $\sigma_g = 0 - 1.0$  eV has been used (dashed lines), for illustration. This is larger than the expected inhomogeneity of the plasma potential, which is in the 10 mV range.

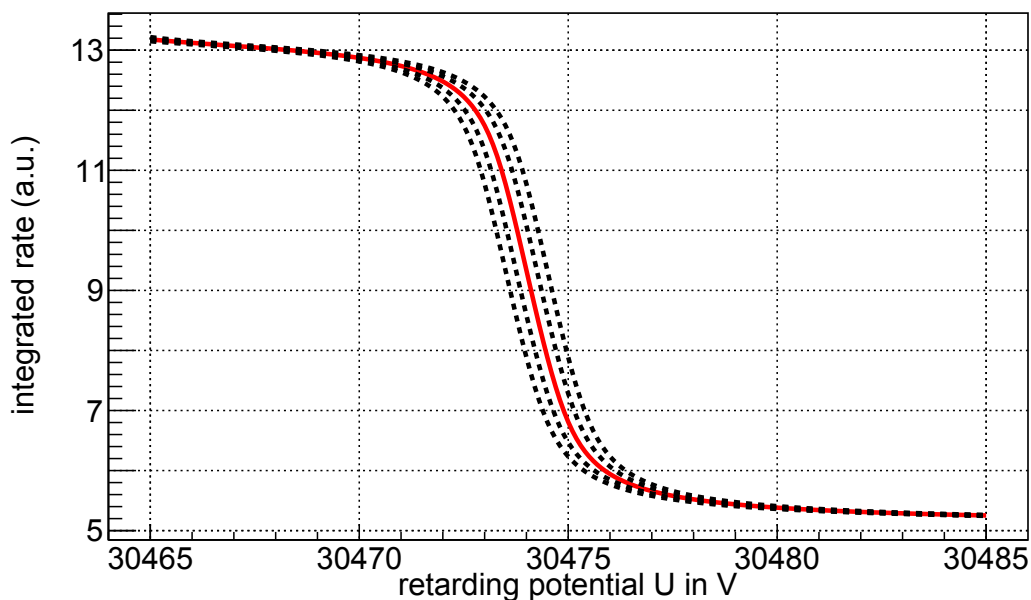


Figure 4.2.: Shift of the krypton-83m  $L_3$  conversion line with  $E_{\text{shift}}$ : An exaggerated range of  $E_{\text{shift}} = -0.5 - 0.5$  eV is shown, where for a realistic plasma potential some 10 meV are expected.

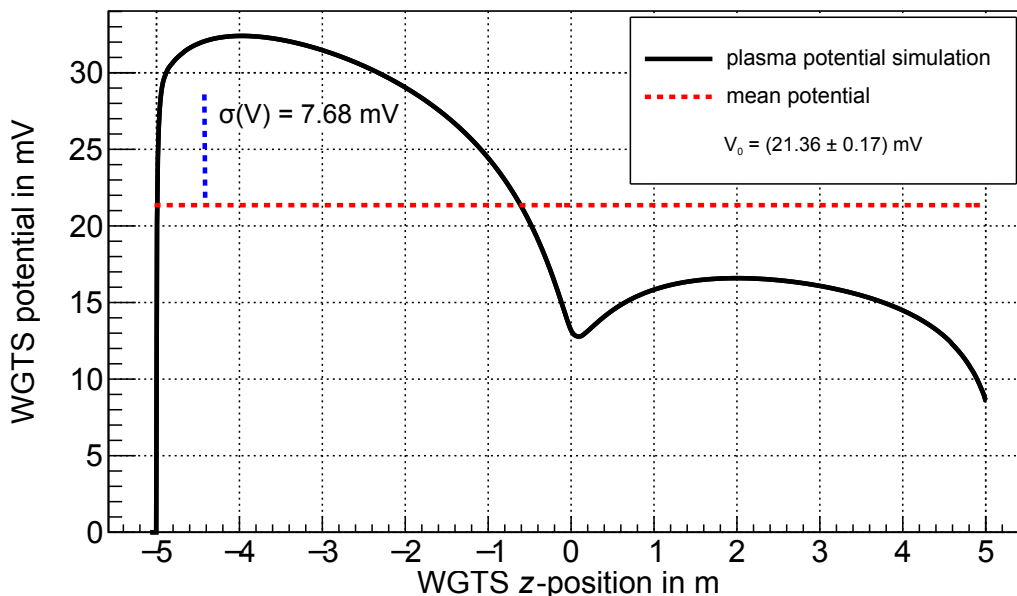


Figure 4.3.: Fit of the 110 K plasma potential simulation with a single mean  $V_0$ : the value of  $V_0$  is related to the value of  $E_{\text{shift}}$  in krypton-83 mode measurements. The standard deviation  $\sigma(V)$  has been calculated following the definition in equation 4.2.

Second, to use the values of  $E_{\text{shift}}$  and  $\sigma_g$  obtained from krypton-83m measurements to correct or quantify systematic effects in tritium  $\beta$  measurements, they will have to be translated to tritium conditions, respecting the scaling of the WGTS potential with temperature.

Third, it has to be assumed that the effect of the plasma potential on the tritium  $\beta$  spectrum and the krypton-83m conversion spectrum is equivalent. If this is not the case at least the differences have to be known, thus, relations corresponding to those in equation 4.1 have to hold for the endpoint  $E_0$  and the broadening  $\sigma_\beta$  of the  $\beta$  spectrum.

Fourth, the broadening of the spectra as consequence of the plasma potential has to be the dominant effect. In this case it can be analytically calculated that for the induced neutrino mass shift it holds [RK88]

$$\Delta m_\nu^2 = -2\sigma_\beta^2. \quad (4.3)$$

Since it is expected that  $\sigma(V)$  decreases with temperature,  $\sigma_g$  should present an upper limit on  $\sigma_\beta$  and thus on the neutrino mass shift.

However, the major finding of this work is that assumption three and most dominantly assumption four are not correct for standard (krypton-83m and tritium) operation of KATRIN, the consequence of which will be discussed in section 4.6.

Table 4.1.: **Ellipse model: table of simulation parameters.**

The free fit parameters are the tilt to the axis  $\alpha$ , the semi-minor axis  $b$  and the potential offset  $V_0$ . When fitting to plasma potential simulations the semi-major axis  $a$  and the  $z$  centre  $z_0$  always yielded values very much compatible with their values in the table, therefore those values were fixed to facilitate the description. The model can be further simplified by fixing either of the free parameters, while respecting the different form of the potential for front and rear side.

parameter	rear	front
$\alpha$	free	free
$b$	free	free
$V_0$	free	free
$a$	2.5 m	2.5 m
$z_0$	-2.5 m	2.5 m

#### 4.1.2. Ellipse Potential Model

The ellipse model is suitable for accurate fits of the simulated plasma potentials using 6 free parameters. A general, physically motivated feature of the model is, that it is divided into independent functions for the front and the rear part of the WGTS.

In the most general form these functions are taken as two half ellipses, each of which are calculated using the following parameterisation:

$$\begin{pmatrix} V(t) \\ z(t) \end{pmatrix} = \begin{pmatrix} V_0 + a \cos t \sin \alpha + b \sin t \cos \alpha \\ z_0 + a \cos t \cos \alpha - b \sin t \sin \alpha \end{pmatrix}, \quad t_0 < t < t_1. \quad (4.4)$$

The parameter bounds are chosen in such a way, that the path length is always smaller than that of a half ellipse, which corresponds to a well defined function (with exactly one  $V$  for every  $z$ ):  $t_0 = \arctan(-\frac{b}{a} \tan \alpha)$ ,  $t_1 = t_0 + \pi$ .

Accordingly every ellipse is completely described by its centre  $(V_0, z_0)^T$ , the semi-major respectively semi-minor axis  $a$  and  $b$ , and the tilt  $\alpha$  with respect to the  $z$  axis. This makes for 10 parameters in total for the most general description. The curves are calculated for discrete  $t$  with  $\Delta t = 0.01$  and the corresponding points are linearly interpolated to get the path.

To simplify the parameter space, some of the parameters were fixed. This leads to a slight deterioration of the goodness of the fits to plasma simulations in the mV range, which becomes more prominent with increasing the tilt to the  $z$  axis. However, the overall description is correct to the mV level, which can be seen in figure 4.4. An overview over the standard values can be found in table 4.1.

The model can be further simplified by fixing the tilt or the semi minor axis to zero, which leads to a description of the plasma potential of the corresponding WGTS side as an upright half ellipse or a line, respectively. If both  $\alpha$  and  $b$  are fixed, the description only contains the mean of the potential on the respective side, corresponding to a fit with a rectangular function.

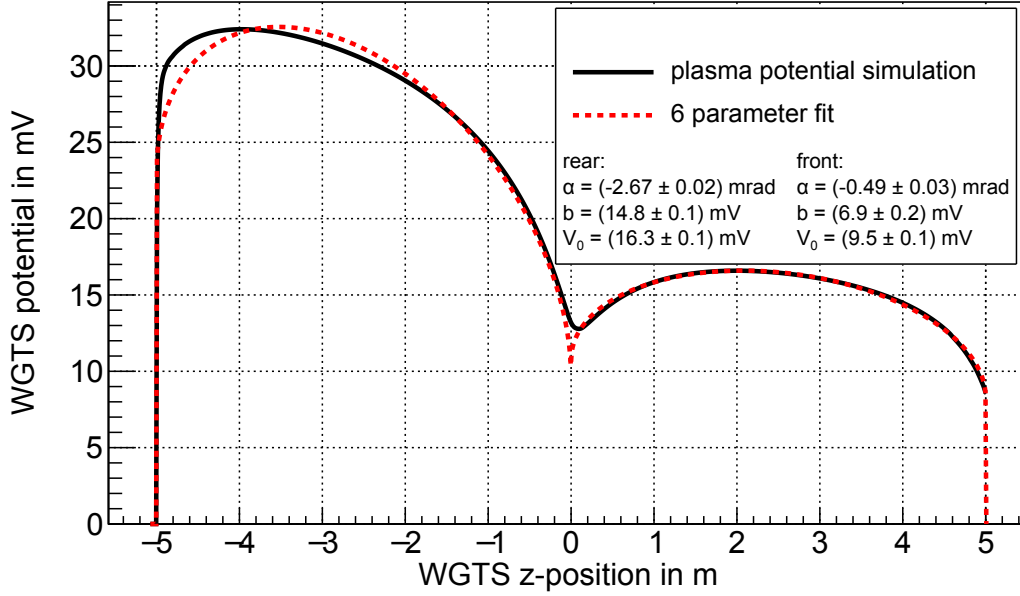


Figure 4.4.: Fit of the 110 K plasma potential simulation with the 6 parameter ellipse model: Slight deviations in the few mV range appear in the rear part, which could be removed by unfixing the corresponding semi major axis. However, the overall agreement is sufficient for the physical description.

### Rectangular model

The rectangular model proved to be a very efficient way of describing the potential in this work. It leads to the description of the potential as sum of  $\Theta$  distributions

$$V(z) = V_0^r \Theta(-z) + V_0^f \Theta(z), \quad (4.5)$$

with the mean potentials for rear and front  $V_0^r$  and  $V_0^f$ , respectively. The corresponding fit can be seen in figure 4.5.

### 4.1.3. Polynomial Potential Model

A simplified description of the simulated plasma potential can be given by a polynomial model, which was implemented in the following form:

$$V(z) = \sum_i a_i \cdot z^i. \quad (4.6)$$

For this work the description is restricted to linear order. In this case it consists of a constant shift  $a_0$  and the slope  $a_1$ , which carries some information about the inhomogeneity of the potential. Figure 4.6 shows a fit of the plasma potential simulation.

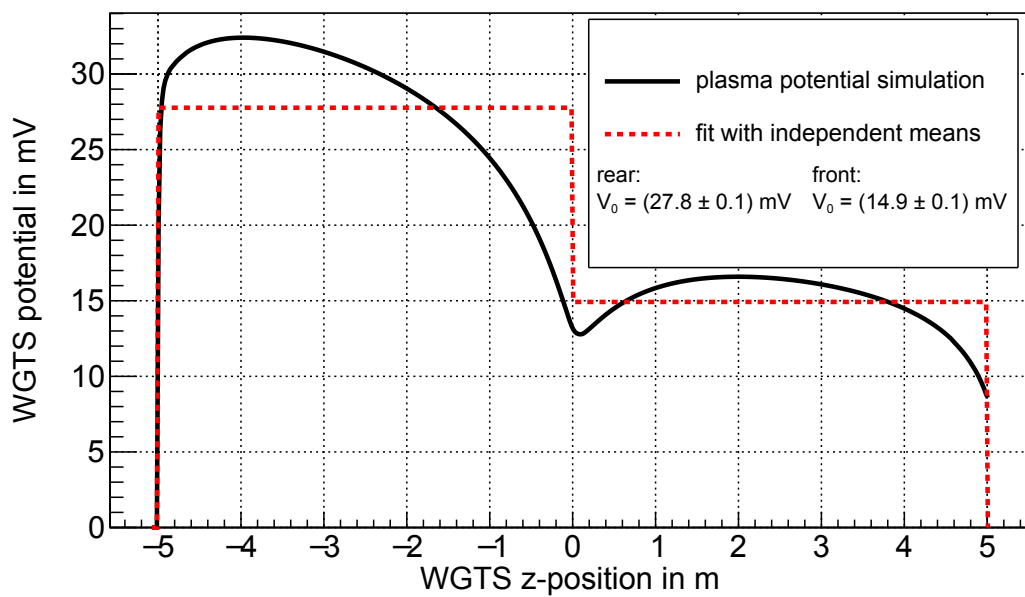


Figure 4.5.: Fit of the 110 K plasma potential simulation with a simplified, 2 parameter ellipse model: Since the minor axis and tilts of the ellipses are set to zero, rectangles are obtained, corresponding to a fit of the potential simulation with independent means for rear and front part of the WGTS.

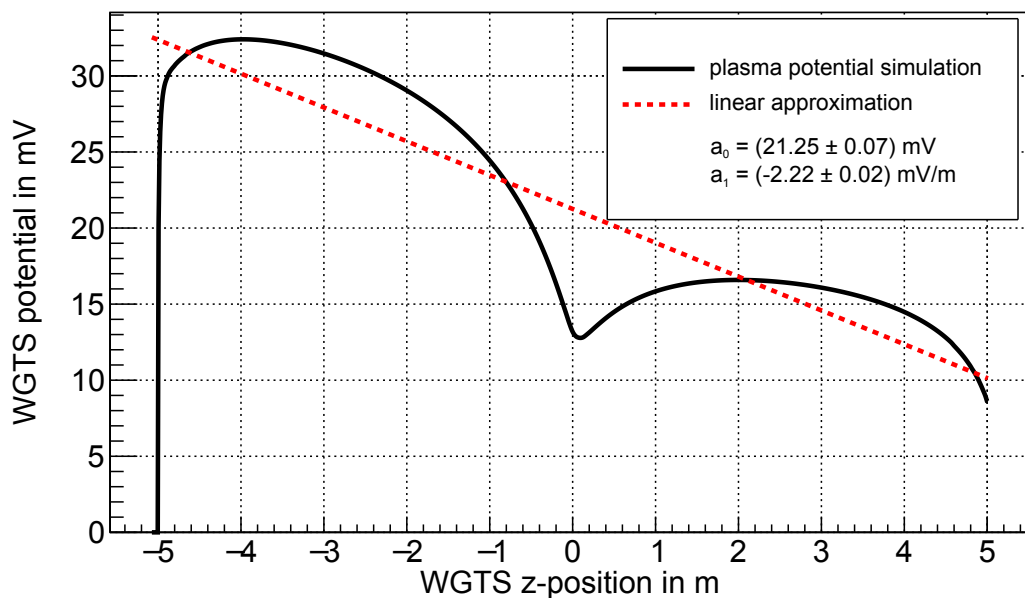


Figure 4.6.: Linear fit of the 110 K plasma potential simulation: Clearly this is only a loose approximation of the actual shape, but it qualitatively covers the total inhomogeneity as well as the overall slope of the potential.

Table 4.2.: **Simulation parameters and their corresponding ranges**

Identified influences on the krypton-83m mode simulation studies which differ from nominal tritium runs and the corresponding chosen values/ranges. In addition systematic uncertainties are projected, whose influence on the measurement is the subject of systematic studies.

The large value for the measurement time reflects the fact that the krypton concentration is not fixed yet and has been estimated conservatively low.

parameter	value
total measurement time (h)	$0.1 - 10^6$
tritium column density ( $\text{m}^{-2}$ )	5 and $50 \cdot 10^{20}$
krypton column density ( $\text{m}^{-2}$ )	$3.83 \cdot 10^{10}$
null hypothesis	110 K in figure 3.10 and $V \equiv 0$
central temperature (K)	$110 \pm 2$
inelastic cross section at $\approx 30$ keV ( $\text{m}^2$ )	$2.106 \cdot 10^{-22} \pm 2.5\%$
tritium viscosity at 110 K ( $\frac{\text{kg}}{\text{m}\cdot\text{s}}$ )	$7.47 \cdot 10^{-6}$
transmission width at $\approx 30$ keV (eV)	1.5

## 4.2. Input Parameters for the Simulation Studies

A comprehensive list of all the parameters which differ in krypton-83m mode from those in tritium mode can be found in table 4.2<sup>1</sup>. A detailed explanation is given in the following sections.

### 4.2.1. The Inelastic Scattering Cross Section

The energy loss of the electrons inside the WGTS is described by an energy loss function (shown in figure 2.8) which includes a detailed modelling of different scattering processes, each of which is energy dependent. Consequently, compared to measurements at the tritium endpoint it has to be adjusted for simulations of  $E \approx 30.5$  keV measurements. This was calculated using the KATRIN software package KELoss, which shows no qualitative changes to the energy loss function of  $E \approx 18.6$  keV shown in figure 2.8.

However, the accuracy of the calculated energy loss functions will not suffice for an actual neutrino mass measurement. Consequently, a precise measurement of the energy loss function will have to be performed using the Rear Section electron gun.

The energy loss function is scaled with the total inelastic scattering cross section  $\sigma_{\text{tot}}$ , which is also energy dependent.  $\sigma_{\text{tot}}$  is adjusted by assuming an inverse proportionality with the electron energy according to [Liu73], where the stated logarithmic dependency is negligible. This leads to a about 1.6 times smaller cross section for electrons in the 30 keV

<sup>1</sup>It should be noted that (small) uncertainties on these parameters do not lead to major changes of the results of the simulation studies: since they are present both in the toy measurement data as well as in the theoretical expectation, they will cancel.

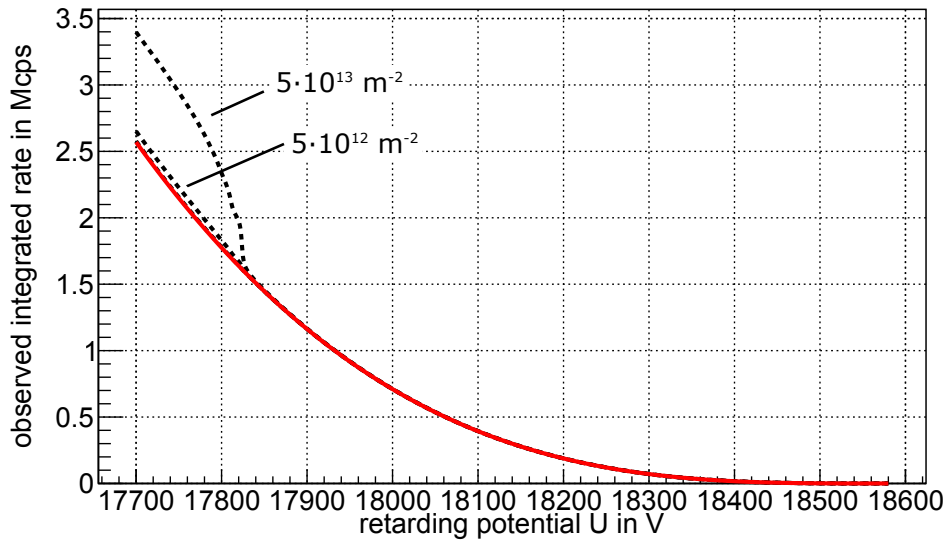


Figure 4.7.: Krypton-83m  $K$  conversion line measured on a tritium  $\beta$  background (continuous line) with nominal tritium column density  $\rho d_{\text{Tr}} = 5 \cdot 10^{21} \frac{1}{\text{m}^2}$ ; krypton-83m column densities in the range of  $\rho d_{\text{Kr}} = 5 \cdot (10^{10} - 10^{13}) \frac{1}{\text{m}^2}$  are included, where only for the highest two the step at  $E_{\text{mean}}^K = 17824 \text{ eV}$  can be seen (dashed lines). The count rates at the  $K$  line are in the order of the current limit of the FPD of  $\approx 3.3 \text{ Mcps}$  integrated over all pixels.

range compared to the value at the tritium endpoint (taken from [Ase+00]):

$$\sigma_{\text{tot}}(E = 30475 \text{ eV}) = \frac{18575}{30475} \cdot 3.456 \cdot 10^{-22} \text{ m}^2 = 2.106 \cdot 10^{-22} \text{ m}^2. \quad (4.7)$$

Since the need for an accurate energy loss function for  $E > 30 \text{ keV}$  for krypton-83m measurements would imply a second, time consuming electron gun measurement, the uncertainty of the cross section is subjected to a systematic analysis. The uncertainty is projected equally as for 18.6 keV to  $\sigma_{\text{syst}}(\sigma_{\text{tot}}) = 2.5 \%$ .

#### 4.2.2. Influence of the Tritium Column Density on $^{83\text{m}}\text{Kr}$ -Mode Studies

The tritium column density  $\rho d_{\text{Tr}}$  plays a major role in WGTS plasma formation, which is discussed in 3.3. Thus, for studying of systematic effects on tritium  $\beta$  spectrum measurements related to the WGTS plasma with the krypton-83m mode, it is advantageous to choose the same tritium column density. The nominal value is  $\rho d_{\text{Tr}} = 5 \cdot 10^{21} \frac{1}{\text{m}^2}$ .

However, there are two arguments in favour of a reduced  $\rho d_{\text{Tr}}$  in krypton-83m mode:

- When measuring at energies around the krypton-83m  $K$  conversion line, the tritium  $\beta$  spectrum contributes a background rate in the order of 1.6 Mcps at nominal  $\rho d_{\text{Tr}}$  (shown in figure 4.7). Since this is of the order of the current rate limit of the Focal Plane Detector (3.3 Mcps integrated over all pixels [Sch14]), it has been proposed to

reduce the tritium column density. This could be achieved without changing the total column density, by replacing some of the tritium with deuterium, thus lowering the tritium purity  $\epsilon$ .

- As stated in section 3.1 the achievable tritium column density might be limited due to the higher temperatures in krypton-83m mode. This would lead to a reduction of the overall gas column density, without the necessity to change  $\epsilon$ .

The following influence of varying column density on the outcome of the krypton-83m measurements should be considered:

- Plasma formation: This is a major influence on the WGTS potential, discussed in [Kuc16]. If the total column density is drastically reduced, the description as a low density plasma becomes inaccurate. Accordingly, the maximum reduction factor of the column density considered in this work is 0.1. If only the tritium purity is reduced, it will still be possible to simulate the plasma and to translate results from krypton-83m measurements to tritium mode measurement conditions. Most of the simulations presented in this work include the plasma potential simulation shown in figure 3.10 for 110 K in the toy measurement, which was calculated using the nominal tritium column density, even if a smaller total column density is used in the simulation. This is justified, since the sensitivities which are presented in this work are independent of the actual potential.
- Statistical uncertainty: The total column density has a large influence on the scattering probability and consequently on the observed integrated rates of the electrons, which can be seen in figure 4.8. Since mainly unscattered and one time scattered electrons are taken into account in the krypton-83m measurement time distributions used in this work, the statistical error is expected to decrease with the reduction of total column density. In case of a reduction of the tritium purity and  $K$ -conversion line measurements, this effect is enhanced due to the background reduction.
- Systematic uncertainty: Besides the up to now poorly determined plasma potential, scattering is the only included physical process which fundamentally breaks the homogeneity of the energy scale along the  $z$  axis of the WGTS<sup>2</sup>. Since the krypton-83m mode aims to reveal  $z$  inhomogeneities, the observables will depend on the scattering probabilities and correspondingly on the total column density.

For the simulations, which are carried out in this work, only the effects related to a total column density reduction are important. As an input parameter for the analysis, two values have been considered:

$$\rho d_{\text{Tr}} = 5 \cdot 10^{20} \frac{1}{\text{m}^2} \quad \text{and} \quad \rho d_{\text{Tr}} = 50 \cdot 10^{20} \frac{1}{\text{m}^2} . \quad (4.8)$$

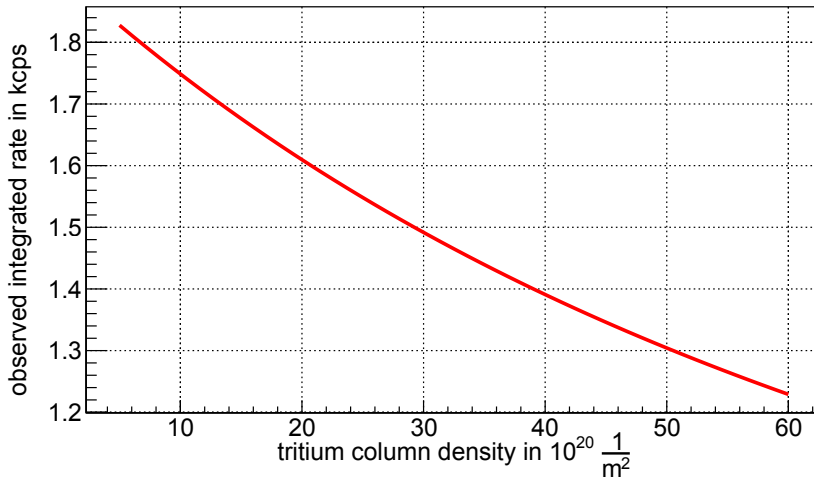


Figure 4.8.: Integrated rate on the plateau of unscattered electrons of the krypton-83m  $L_3$  conversion line as function of the tritium column density: Due to inelastic scattering changes of the total column density by one order of magnitude lead to changes in the unscattered rate of about 40 %. The krypton-83m amount in the source can directly be read off at nominal column density to be  $c_K = 1.3$  in this example.

#### 4.2.3. The Amount of $^{83m}\text{Kr}$ inside the Source

Evidently the amount of krypton-83m released into the WGTS determines the observed integrated rate of conversion electrons. Thus, a high krypton column density  $\rho d_{\text{Kr}}$  is desirable in order to reach a low statistical uncertainty.

The krypton-83m will be continuously supplied by a rubidium-83 generator of initial activity  $A_{\text{Rb}}(0)$ , with a branching ratio of 0.74 [McC15]. Consequently, the number of krypton-83m conversion electrons follows a decay chain, with the rubidium-83 decay rate  $\lambda_{\text{Rb}} = 9.3 \cdot 10^{-8} \frac{1}{\text{s}}$  and the krypton-83m decay rate  $\lambda_{\text{Kr}} = 1.1 \cdot 10^{-4} \frac{1}{\text{s}}$ . The total amount of mesomeric krypton-83m  $N_{\text{Kr}}$  which is generated can be written as:

$$N_{\text{Kr}}(t) = 0.74 \frac{A_{\text{Rb}}(0)}{\lambda_{\text{Rb}}} \frac{\lambda_{\text{Rb}}}{\lambda_{\text{Kr}} - \lambda_{\text{Rb}}} \cdot (e^{-\lambda_{\text{Rb}}t} - e^{-\lambda_{\text{Kr}}t}) \stackrel{t > 10^4 \text{s}}{\approx} 0.74 \frac{A_{\text{Rb}}(0)}{\lambda_{\text{Kr}}} \cdot e^{-\lambda_{\text{Rb}}t} . \quad (4.9)$$

The last step is valid as soon as the decay reaches the transient equilibrium after a few hours.

The number of krypton-83m atoms inside the WGTS is further reduced by the emanation efficiency  $F_E = 0.8$  [Vén+14] of krypton-83m from the rubidium-83 source, adsorption on the walls  $F_A = 0.3$ , and the ratio of krypton-83m atoms inside the WGTS to those inside the supplying loop system:  $F_V = 0.1 - 0.001$  [Ker04]. Obviously the latter is a major source

<sup>2</sup>The gas profile provides another violation, but it is (nearly) symmetric to the injection point, hence this symmetry is left over without scattering. Furthermore, it does not affect the energy of the electrons, but only the rate.

of uncertainty, since a calculation has to take into account the pressure profiles of every krypton-83m containing pipe. Therefore this calculation is taken as an order of magnitude estimate.

Assuming a homogeneous distribution, the total number of krypton-83m atoms inside the WGTS beam tube is obtained as a product of the krypton-83m column density and the cross section  $\mathcal{A}_{\text{source}} = 64 \text{ cm}^2$  [KAT04]. Consequently, for the total number of krypton-83m atoms inside the WGTS beam tube one obtains

$$N_{\text{Kr}}^{\text{WGTS}} = \rho d_{\text{Kr}} \cdot \mathcal{A}_{\text{source}} = 0.74 F_E F_A F_V \frac{A_{\text{Rb}}(0)}{\lambda_{\text{Kr}}} \cdot e^{-\lambda_{\text{Rb}} t} . \quad (4.10)$$

In transient equilibrium the time dependence of the number of krypton-83m atoms inside the WGTS is dominated by the rubidium-83 decay rate, which is comparably slow. Over a measurement time of 10 h this would lead to a relative change of the krypton-83m column density of 0.3 %, which is neglected in this study<sup>3</sup>. Consequently, this effect has to be compensated for in data analysis or in the measurement procedure<sup>4</sup>. For the purpose of this analysis, the exponential factor in equation 4.10 is set to 1.

Considering the quantities given, the following range of the krypton-83m column density is obtained:

$$\frac{\rho d_{\text{Kr}}}{1/\text{m}^2} \propto (10^{11} - 10^{13}) \cdot \frac{A_{\text{Rb}}(0)}{\text{GBq}} . \quad (4.11)$$

For the foreseen rubidium-83 source activity in the 1 GBq range [Vén+14] a krypton concentration in the range of  $10^{-11} - 10^{-8}$  is obtained.

This justifies the lower density limit which is used in the gas dynamics simulation presented in section 3.2.2<sup>5</sup>. As a direct consequence the amount of krypton-83m inside the WGTS beam tube only scales the krypton-83m conversion electron spectrum without any secondary effects. Thus, it is fixed to the value of  $c_{\text{K}} = 1$  with the following definition:

$$c_{\text{K}} \equiv \frac{\rho d_{\text{K}}}{3.83 \cdot 10^{10} \frac{1}{\text{m}^2}} . \quad (4.12)$$

$c_{\text{K}}$  is very descriptive, since it is equivalent to the integrated  $L_3$  count rate in kcps on the plateau. This only holds in the case of nominal tritium column density, where the change due to scattering can be seen in figure 4.8.

According to the above discussion  $c_{\text{K}} = 1$  can be taken as an absolute lower limit on the krypton-83m amount inside the source. For all but the  $K$  line it is valid to model higher concentrations of krypton-83m by choosing exceedingly high measurement times, which will be discussed in the following section.

<sup>3</sup>Including time dependent effects is currently not supported in SSC and would require major changes in the software structure.

<sup>4</sup>The measurement procedure used at the predecessor Mainz neutrino experiment is discussed in [Thü07]. For total measurement times less than an hour, the change of krypton-83m conversion electron rate has been found to be approximately linear. Thus, a mirrored ramping from low to high retarding voltages and back has been used to eliminate the effect.

<sup>5</sup>Even in the most generous case where the factors in equation 4.10 are set to 1, the concentration will not exceed  $10^{-6}$ .

#### 4.2.4. Measured Conversion Lines and Measurement Time Distribution

The 32 keV transition of the krypton-83m conversion electron spectrum generates several lines which can be used for systematic studies at KATRIN. The lines included for the studies in this work are listed in table 3.2.

Naturally, favourable characteristics of the lines are high relative intensity, low background and a small intrinsic width<sup>6</sup>. Thus, the following section aims to identify the line with the best compromise in combining these quantities, an effect which is chosen for the simulation studies.

Table 4.3 shows integrated rates for different krypton-83m conversion lines to be observed in a realistic KATRIN measurement. The values are taken at retarding potentials  $U = \pm 7\text{ V}$  with respect to the line means, thus the upper value lies on the plateau of unscattered electrons. The difference of  $\dot{N}^+$  and  $\dot{N}^-$  can be interpreted as the signal rate. The background component  $\dot{N}^-$  is induced by conversion lines at larger energies, which contribute to the count rate due to the integral measurement. Given the Poissonian statistic of the counts the square root of  $\dot{N}^+$  is used as a measure of statistical uncertainty, respecting the contribution of both the signal and the background. This leads to the following definition of the Signal to Noise Ratio (SNR) after a given measurement time  $t$ :

$$\text{SNR} = \frac{\text{signal}}{\sqrt{\text{signal} + \text{background}}} = \frac{\dot{N}^+ - \dot{N}^-}{\sqrt{\dot{N}^+}}. \quad (4.13)$$

The  $K$  line merits a dedicated discussion, since its mean energy of  $E_{\text{mean}}^K = 17824\text{ eV}$  is smaller than the tritium  $\beta$  spectrum endpoint  $E_0 = 18575\text{ eV}$  and it is well separated from the  $\approx 30\text{ keV}$  lines. This has two implications:

- In measurements without tritium (rest tritium column density  $\lesssim 10^{16} \frac{1}{\text{m}^2}$ ) the  $K$  line can be measured quasi background free, since the energy resolution of the focal plane detector is sufficient to subtract the background of the higher energetic lines.
- In measurements with a mixture of krypton-83m and tritium the  $\beta$  spectrum contributes a strong background.

The values for the count rates and SNRs for two different tritium column densities can be found in table 4.4. Even in the case when the tritium background is completely neglected, as would be justified for a mixture of krypton-83m and deuterium, the SNR of the  $L_3$  line is slightly larger. Moreover the  $L_3$  line offers a comparably small intrinsic width  $\Gamma$  (table 3.2). It therefore has been selected for the simulation studies. In addition, it is also instructive to study the  $K$  line: Due to the large energy separation of the 30 keV lines and the  $K$  line, the transmission width of the MAC-E filter and the inelastic scattering cross section are significantly different. Thus, the  $K$  line bears further physical relevance.

<sup>6</sup>This is intuitively expected. However, krypton-83m measurements of the Mainz neutrino experiment showed shifting line means with changes of the transmission width for some lines [Thü07]. It was concluded that the line width should possibly always be larger than the transmission width. The simulations of this work do not reproduce this effect. Thus, another explanation could be the loss of electrons with high surplus energies due to non-adiabaticity, which is much smaller for the KATRIN main spectrometer.

Table 4.3.: **Signal to Noise Ratio for the krypton-83m conversion lines in the  $E \approx 30$  keV range**

The integrated rates  $\dot{N}^+$  and  $\dot{N}^-$  are evaluated 7 V above and below the mean line position, respectively. The Signal to Noise Ratio (SNR) is calculated following the definition in the text. The  $L_3$  line shows the highest SNR and a small width  $\Gamma$  at the same time and is consequently chosen for the krypton mode studies.

The values are normalised such that  $\dot{N}^+(L_3) = 1$  kcps, corresponding to  $c_K = 1$ . The total column density has an influence on the presented values due to inelastic scattering and is taken to be at the nominal value of  $\rho d_{\text{Tr}} = 5 \cdot 10^{21} \frac{1}{\text{m}^2}$ .

a) Values are too small, since higher lines have been neglected.

Line	$\dot{N}^+$ /cps	$\dot{N}^-$ /cps	$\text{SNR}/\sqrt{t}/s \cdot c_K$
$L_1$	2561.3	2531.5	0.6
$L_2$	1978.3	1539.1	9.9
$L_3$	1000.0	405.8	18.8
$M_1$	371.0	357.6	0.7
$M_2$	246.6	118.5	8.1
$M_3$	141.6	12.0	10.9
$M_4 + M_5$	5.0	1.8	1.4
$N_1^{\text{a)}}$	1.2	0.5	0.6

 Table 4.4.: **Signal to Noise Ratio of the krypton-83m  $K$  conversion line for different tritium column densities**

Since the tritium  $\beta$  spectrum contributes a mean background rate  $\langle \dot{N}_{\text{Tr}} \rangle$ , the krypton amount  $c_K$  does not cancel in the SNR. Even for a very large  $c_K = 10000$  the SNR of the  $K$  line is much smaller than that of  $L_3$  for nominal tritium column density. Only by reducing the latter, the  $K$  line becomes competitive.

The background of the 30 keV lines is of the order of  $3000 \text{ cps} \cdot c_K$  (if adiabatic guidance of the corresponding electrons is assumed) and has been subtracted.

$\rho d_{\text{Tr}}/10^{20} \frac{1}{\text{m}^2}$	$\dot{N}^+$ /kcps	$\dot{N}^-$ /kcps	$\langle \dot{N}_{\text{Tr}} \rangle$ /kcps	$\text{SNR}/\sqrt{t}/s \cdot c_K$
5	0.567	0.038	178	$16.7 \cdot (0.567 + 178 \cdot c_K^{-1})^{-0.5}$
50	0.277	0.023	1612	$8.0 \cdot (0.277 + 1612 \cdot c_K^{-1})^{-0.5}$

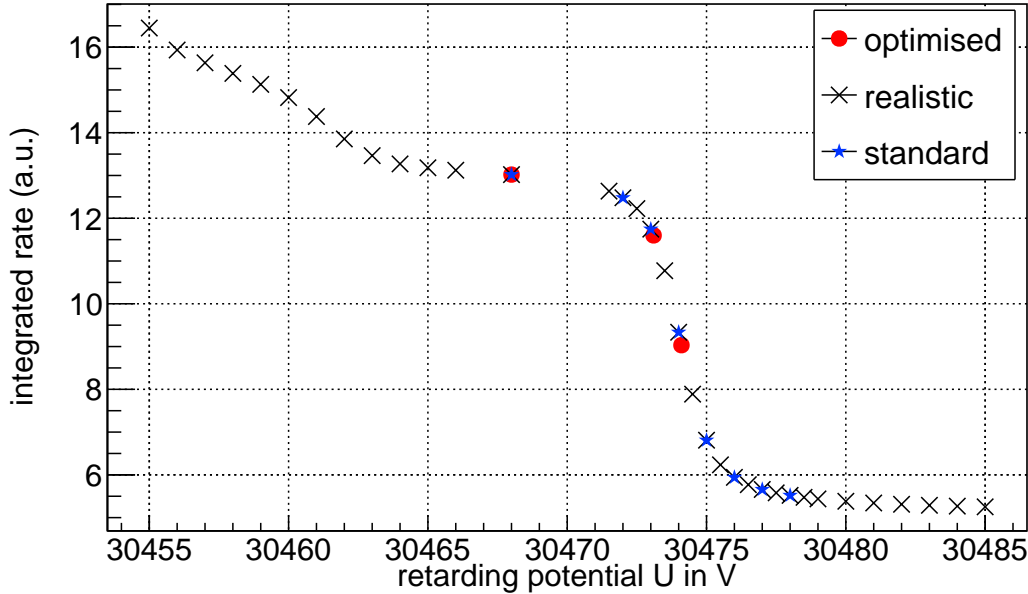


Figure 4.9.: Retarding potentials in different MTDs for the  $L_3$  conversion line: the optimised distribution has exactly one point for every free parameter of the Voigt profile, at retarding potentials where both large statistical sensitivity and low systematics are expected. However, the physical potential produces more complex changes of the spectrum, therefore a denser set of potential set-points should be chosen. A major finding of this work is the fact, that including the scattering step ("realistic" scenario) has an influence on the measurable results in krypton-83m mode, compared to a standard distribution.

The amount of krypton-83m and the total measurement time do only scale the spectra. In the case where no other than the krypton-83m conversion spectrum have to be considered, which is true for the  $L_3$  line, both are a mere measure of the total counts and will only enter the statistical uncertainty as a product.

### Measurement Time Distribution

The dedicated measurement times  $t_i$  at retarding potentials  $U_i$  are referred to as the *Measurement Time Distribution* MTD. The choice of the MTD has an impact in four regards:

- **Maximal sensitivity:** Depending on the model which is fitted to the measured data specific retarding potential settings yield a maximal sensitivity (maximum first derivative of the count rate) to changes of the free model parameters and allow to break correlations between individual parameters.
- **Maximal statistics:** To reduce the relative statistical error of the counts, the retarding potentials should be set to points of high absolute rate.

- **Minimal systematics:** Certain parts of the spectrum may be affected more strongly by the presence of systematic effects. In case of the integrated krypton-83m conversion electron spectrum, the modelling of the steps which evolve due to multiple scattering of the electrons continuously deteriorates with the number of scatterings, due to the uncertainty of the inelastic cross section and the energy loss function. Also, the steps evolving due to the shake up/off effects are not suitable for sensitivity studies on the plasma potential, since their shape is not accurately modelled.
- **Effects of simplified model assumptions:** In the case of phenomenological models the MTD has a significant influence on the parameter estimates, since it determines how a more complex input model is condensed into a smaller set of parameters. For the krypton-83m mode this is of major importance, since the choice of MTD will determine the part of the potential which is actually measured. This is further discussed in section 4.6.

For the Voigt profile a set of optimised retarding potentials is illustrated by the red circles in figure 4.9. It consists of one point at the expected line mean to fix  $E_{\text{shift}}$ , one point on the unscattered plateau to fix  $I$  and one point in between, to fix  $\sigma_g$ . The retarding potential of the latter which yields the maximum sensitivity can be numerically calculated as the maximal first derivative of the (integrated) Voigt profile.

However, for the phenomenological models of the WGTS potential the choice of those potentials is not as obvious. In addition, sensitivity on a potential model should not be mistaken for sensitivity on the physical potential, since all tested models are of phenomenological nature and the shape of the actual potential is not known a priori.

Different distributions were tested in this work, with most of them yielding qualitatively similar results. However, large differences could be observed between distributions which include the step of first scattering ("realistic" scenario in figure 4.9) and those which only measure at the unscattered step ("standard" scenario in figure 4.9). This is not due to systematic effects, but due to the impact of simplified model assumptions and is discussed in section 4.6.1.

In the sets of retarding potentials shown in figure 4.9 the measurement time per retarding potential is equally distributed. Thus, some optimisation could possibly be made at this point. A further discussion towards an optimised distribution, which should be guided by the findings of this work, can be found in appendix A.2.

Table 4.5.:  **$z$ -averaged scattering probabilities for electrons in the 30 keV range**

The  $z$ -averaged scattering probabilities for  $n$  time scattering  $\langle p_n \rangle$  are shown for nominal and reduced column density. An inelastic cross section of  $\sigma_{\text{tot}} = 2.106 \cdot 10^{-22} \text{m}^2$  is assumed, as deduced in section 4.2.1.

$\rho d$ in $10^{20} \frac{1}{\text{m}^2}$	$\langle p_0 \rangle$	$\langle p_1 \rangle$	$\langle p_2 \rangle$	$\langle p_3 \rangle$	$\langle p_4 \rangle$ and higher
5	93.7 %	6.0 %	0.3 %	<0.1 %	<0.1 %
50	55.9 %	28.6 %	11.0 %	3.4 %	<1.0 %

### 4.3. Sensitivity on Axial Effects in the WGTS in the Presence of Inelastic Scattering

Due to inelastic scattering on the gas inside the WGTS the signal electrons can lose energy, while traversing the WGTS. The probability for this process to occur  $i$  times can be calculated [Ase+00] via

$$p_i(z, \theta) = \frac{(\lambda(z, \theta) \cdot \sigma_{\text{tot}})^i}{i!} e^{-\lambda(z, \theta) \cdot \sigma_{\text{tot}}}, \quad (4.14)$$

where the effective column density in front is obtained as

$$\lambda(z, \theta) = \frac{1}{\cos \theta} \int_z^{L_{\text{WGTS},f}} \rho(z') dz'. \quad (4.15)$$

$\theta$  is the emission angle of the electron with respect to the  $z$ -axis,  $L_{\text{WGTS},f}$  the length of the front side of the WGTS and  $\sigma_{\text{tot}}$  the total inelastic cross section. Thus, the probability that a measured electron has been scattered  $i$  times is related to the position inside the WGTS where it originated from.  $z$  averaged values for the scattering probabilities  $p_i$  can be found in table 4.5.

The fraction of energy that the electrons lose is described by the energy loss function, which is presented in figure 2.8. A dominant feature of this function is a peak at  $\approx 13$  eV, which is the minimal possible inelastic energy loss. Consequently, the energy scale can roughly be divided into 13 eV intervals, indicating the number of energy loss processes an electron was subjected to.

In the case of a continuous tritium  $\beta$  spectrum, of course, this effect gets washed out.

In the krypton-83m  $L_3$  conversion electron spectrum, however, the effect of inelastic scattering is clearly visible, since it produces an additional step centred 13 eV below the unscattered main step. Due to the  $z$  dependency of the scattering probabilities, electrons originating from different parts of the WGTS do not contribute equally to these steps, which can be seen in figure 4.10. Here the scattering probabilities for zero, single and two-fold scattering ( $p_0, p_1, p_2$ ) of the electrons are shown as function of  $z$  for nominal tritium column density. Due to inelastic scattering measuring different parts of the electron spectrum is related to measuring electrons originating from different regions of the WGTS.

Notably, this mechanism strongly depends on the column density. In figure 4.11 the scattering probabilities for the column density reduced by a factor 0.1 are shown. Clearly, the possibility of discriminating the origin of the electrons is drastically lowered, and the energy scale of the WGTS evolves to be nearly homogeneous in axial direction.

4. Simulation Studies of the  $^{83m}\text{Kr}$ -Mode Sensitivity on the Tritium Source Plasma Potential

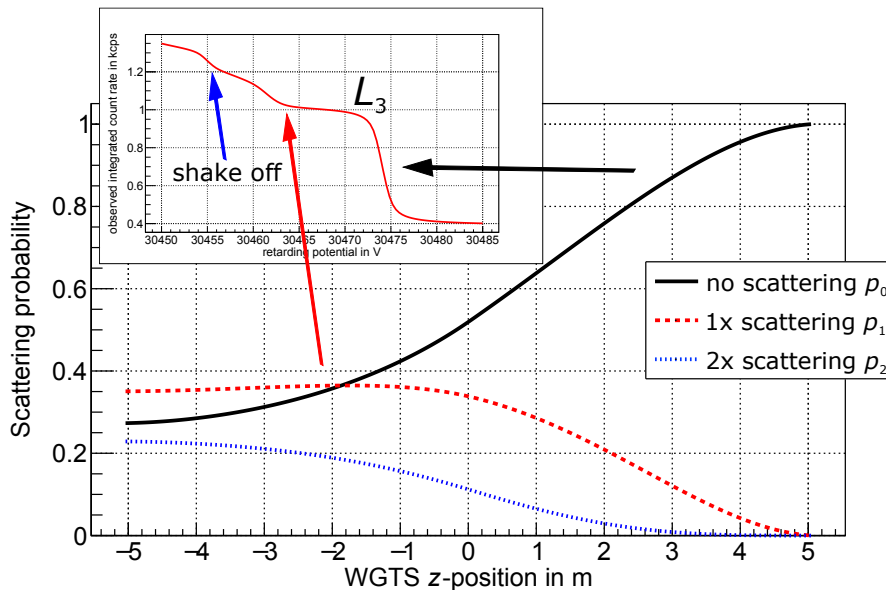


Figure 4.10.: Scattering probabilities for nominal column density of  $\rho d_{\text{Tr}} = 50 \cdot 10^{20} \frac{1}{\text{m}^2}$ : Inelastic scattering relates the origin of the electrons inside the WGTS to regions in the integrated spectrum. In the case of the krypton-83m  $L_3$  conversion electron spectrum, shown in the inset, this is visible at a distinct step of singly scattered electrons. The step at  $E_{\text{mean}} \approx 30455$  eV is due to shake off, which is superimposed with the second scattering.

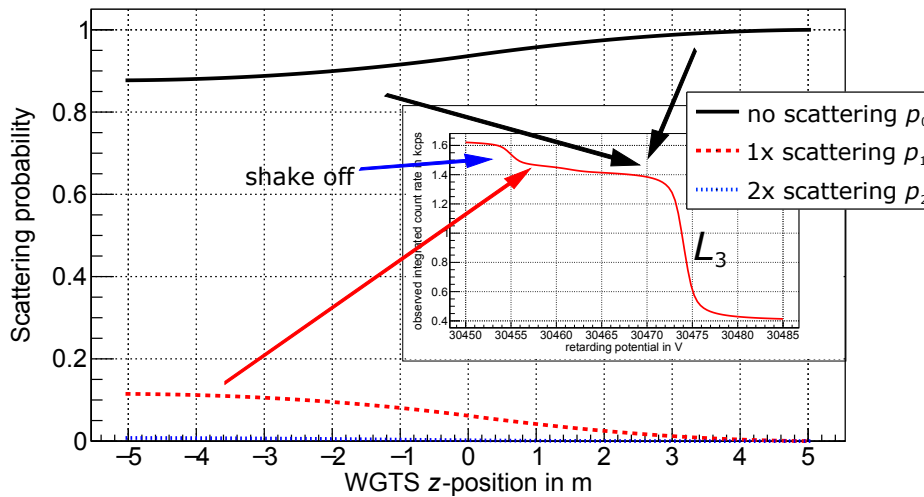


Figure 4.11.: Scattering probabilities for reduced column density of  $\rho d_{\text{Tr}} = 5 \cdot 10^{20} \frac{1}{\text{m}^2}$ : Even in the rear part only 10 % of the electrons lose energy due to inelastic scattering. Consequently the energy scale of the electrons inside the WGTS is nearly homogeneous. In the krypton-83m conversion electron spectrum, shown in the inset, the step due to singly scattered  $L_3$  electrons almost vanishes.

## 4.4. Statistical Sensitivities of the Parameters of Different Potential Models

In this section the statistical sensitivities  $\sigma_{\text{stat}}(X)$  of the parameters  $X$  of different potential models are shown. According to the discussion on statistical sensitivities in section 2.2.1 it is expected that  $\sigma_{\text{stat}}$  is inversely proportional to the square root of the total measurement time  $t$  in case of Gaussian distributed, uncorrelated parameters. Thus, the following form of the sensitivities is expected:

$$\sigma_{\text{stat}}(X) = a^* \cdot t^{-n^*}, \quad (4.16)$$

with  $0 < n^* < 0.5$ . Only in case of non-Gaussian distributed (corresponding to non-linear formulated problems) or highly correlated parameters,  $n^*$  will be smaller than 0.5.

The dimension of  $a^*$  and thus the dimension of  $\sigma_{\text{stat}}$  depends on the used model. Ultimately the quantity of interest is a measure of the magnitude of WGTS plasma potential. Therefore, for every parameter statistical sensitivities  $S_{\text{stat}}$  as functions of  $\sigma_{\text{stat}}$  are defined that have dimension of potential.

Furthermore, for the krypton-83m  $L_3$  conversion line measurement time and integrated count rate are simply a measure of the total number of counts and do only enter the statistical sensitivity as product <sup>7</sup>. Thus, equation 4.16 is replaced by

$$\frac{S_{\text{stat}}(\sigma_{\text{stat}}(X))}{\text{mV}} = \frac{a}{(t/h \cdot \dot{N}_{\text{unsc}}/\text{kcps})^n}, \quad (4.17)$$

with dimensionless parameters  $a$  and  $n$  and the unscattered integrated count rate  $\dot{N}_{\text{unsc}}$ , measured 7 V below the mean. The values of  $a$  and  $n$  for the different models can be found in the tables 4.6, 4.7, 4.8, 4.9 and 4.10.

A description of the models is given in 4.1. The full ellipse model only converged after unrealistically long measurement times. Thus, the following discussion is restricted to the simplified rectangular model using the independent fit for front and rear plasma potential of the WGTS. The definitions of the statistical sensitivities are

$$\begin{aligned} S_{\text{stat}}(E_{\text{shift}}) &= \frac{1}{e} \sigma_{\text{stat}}(E_{\text{shift}}), \\ S_{\text{stat}}(\sigma_g) &= \frac{1}{e} \sqrt{\sigma_{\text{stat}}(\sigma_g^2)}, \\ S_{\text{stat}}(V_0) &= \sigma_{\text{stat}}(V_0), \\ S_{\text{stat}}(a_0) &= \sigma_{\text{stat}}(a_0), \\ S_{\text{stat}}(a_1) &= \sigma_{\text{stat}}(a_1) \cdot L_{\text{WGTS}}. \end{aligned} \quad (4.18)$$

$e$  is the elementary electric charge and  $L_{\text{WGTS}}$  the length of the WGTS. These definitions ensure that the plots showing the statistical sensitivities which are presented on the following pages are directly comparable.

<sup>7</sup>For the simulation the krypton column density of  $\rho d_{\text{Kr}} = 3.84 \cdot 10^{10} \frac{1}{\text{m}^2}$  ( $\dot{N}_{\text{unsc}} = 1 \text{ kcps}$ ) was used and only the total measurement time was varied.

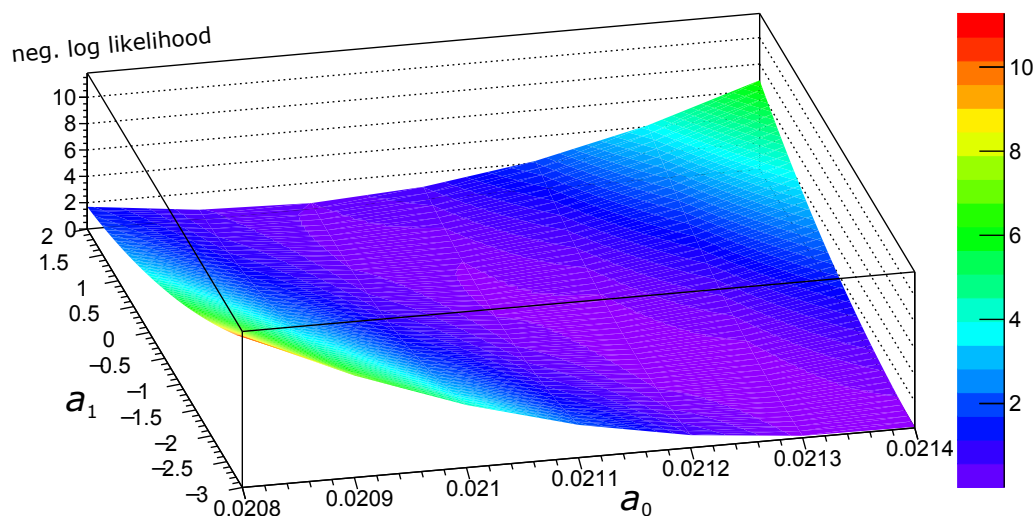


Figure 4.12.: Two dimensional negative log-likelihood of the linear model for tritium column density of  $5 \cdot 10^{20} \frac{1}{\text{m}^2}$  and null hypothesis of the 110 K plasma potential simulation: The minimum of the surface is a line which is perfectly diagonal in the plane of the constant part  $a_0$  and the slope  $a_1$  of the potential. Hence, the parameters are almost completely anti correlated. This is exemplary for all simulations using WGTS plasma potential models and a reduced tritium column density.

### Null Hypothesis and Measurement Time Distribution

Three different measurement time distributions are used, which are shown in figure 4.9. The optimised distribution is only tested for the Voigt profile.

Since the null hypothesis of the 110 K WGTS plasma simulation was used, the fitted parameter estimates are also given. If the fit algorithm finds the correct minimum, they are not affected by the total measurement time, thus it is sufficient to state only one value. In the case where the estimates were not stable, indicating highly correlated model parameters or ill set models, a ' $\approx$ ' is put in front. In the case where they were smaller than or in the order of the statistical uncertainty, ' $\lesssim$ ' is prepended.

For all models also the null hypothesis of vanishing potential was tested, which had minor influence on the resulting sensitivities. Therefore, only the results including the 110 K plasma potential simulation are shown. However, in case of the Voigt profile no valid minima could be found when combining the realistic measurement time distribution and the 110 K plasma potential null hypothesis. Therefore, for the Voigt profile also the results for the null hypothesis of vanishing potential are presented.

### Tritium Column Density

Most of the presented results use the nominal tritium column density of  $\rho d_{\text{Tr}} = 5 \cdot 10^{21} \frac{1}{\text{m}^2}$ , since for a tritium column density reduced by a factor of 0.1, the WGTS plasma potential models did not converge. The reason for this are strongly correlated parameters, which is exemplarily shown in figure 4.12. Only for the Voigt profile results for the reduced column density are given.

### Results

The results are presented in the following order:

- **Voigt profile**

- 110 K plasma potential - nominal tritium column density

- vanishing plasma potential - nominal tritium column density

- 110 K plasma potential - reduced tritium column density

- **Rectangular model (simplified ellipse model)**

- 110 K plasma potential - nominal tritium column density

- **Linear model**

- 110 K plasma potential - nominal tritium column density

## Voigt profile - 110 K plasma potential - nominal tritium column density

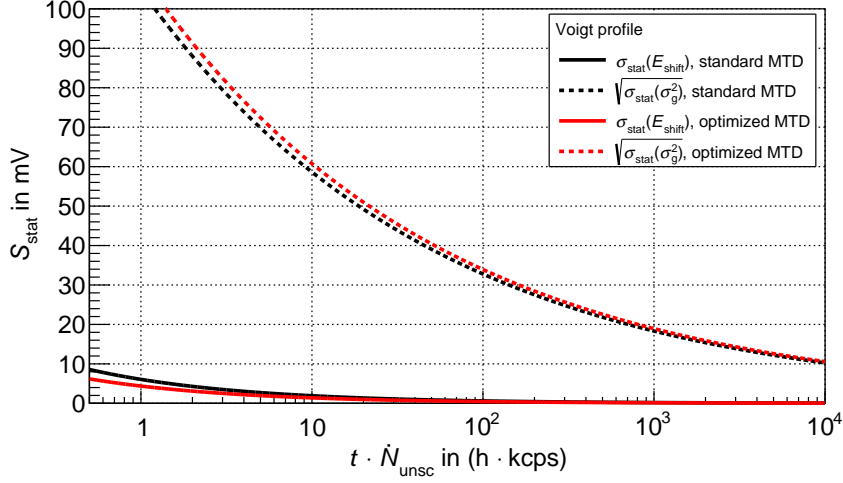


Figure 4.13.: Statistical sensitivity for the parameters of the Voigt profile with null hypothesis of 110 K plasma simulation: The different measurement time distributions lead only to minor changes in the statistical sensitivity on the parameters. For the standard MTD, the line shift, averaged over all detector pixels, is measurable to the 10 mV level at 1 kcps in 22 minutes. Measuring  $\sigma_g$  to this level in a feasible time  $t$  of 10 hours however requires a very strong krypton-83m source, delivering  $\dot{N}_{\text{unsc}} = 1$  Mcps on the unscattered plateau of the  $L_3$  line.

Table 4.6.: **Voigt profile: statistical sensitivities -  $L_3$  - 110 K potential**

The parameter estimate of  $\sigma_g$  decreases with total measurement time in a way, that it is always smaller than the statistical uncertainty. Consequently the lowest value is given, which is much smaller than the standard deviation of the potential of  $\sigma(V) = 7.68$  mV. The parameter estimate on  $E_{\text{Shift}}$  is 13 % smaller than the mean potential  $\langle V \rangle = 21.36$  mV. For the realistic MTD the fitter could only find a minimum for the shortest measurement time, corresponding to a large statistical uncertainty.

The values of  $n$  indicate that  $E_{\text{Shift}}$  and  $\sigma_g^2$  linearly enter the  $\chi^2$  function and that the corresponding likelihood is Gaussian.

MTD	estimates	$a$	$n$
Standard	$E_{\text{Shift}} = 18.86$ meV	$6.067 \pm 0.006$	$0.4992 \pm 0.0005$
	$\sigma_g^2 \lesssim (3.36 \text{ meV})^2$	$104.85 \pm 0.08$	$0.2525 \pm 0.0004$
Optimized	$E_{\text{Shift}} = 18.85$ meV	$4.378 \pm 0.002$	$0.4996 \pm 0.0002$
	$\sigma_g^2 \lesssim (1.5 \text{ meV})^2$	$108.9 \pm 0.5$	$0.2530 \pm 0.0030$
Realistic	No valid minimum		

## Voigt profile - vanishing plasma potential - nominal tritium column density

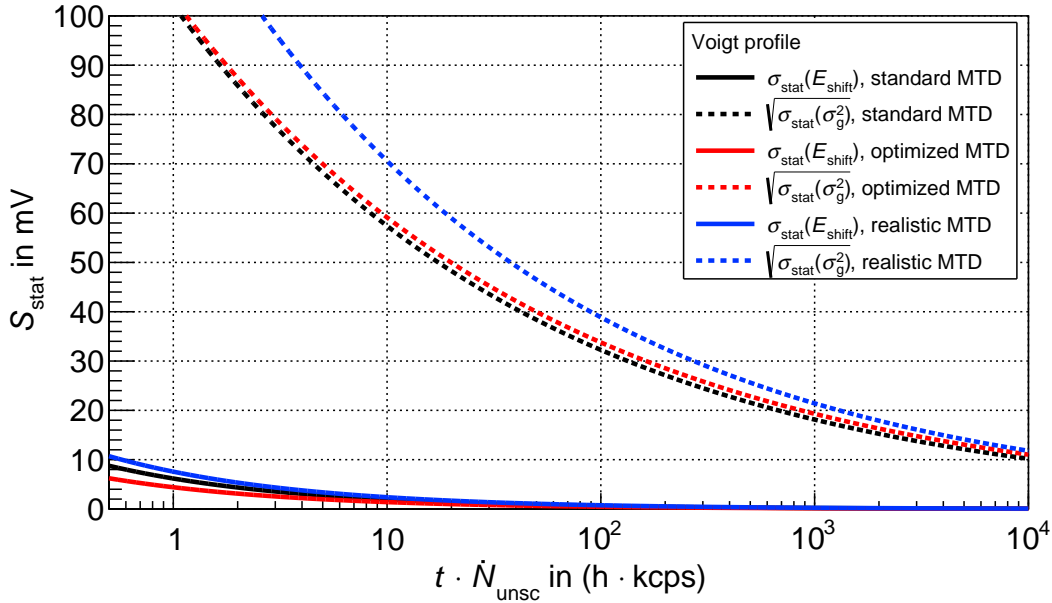


Figure 4.14.: Statistical sensitivity for the parameters of the Voigt profile with null hypotheses of vanishing potential: The changes on the sensitivities due to the different null hypothesis are below 5%. The fits now also converge for measurement time distributions which include the step of singly scattered electrons. However, the sensitivity on  $\sigma_g$  reduces by about 25% compared to the other MTDs. The changes in sensitivity on  $E_{\text{shift}}$  are only significant for very short measurement times.

Table 4.7.: **Voigt profile: statistical sensitivities -  $L_3$  - vanishing potential**

As expected for the null hypothesis of vanishing potential, the parameter estimates on  $E_{\text{shift}}$  and  $\sigma_g$  were in complete accordance with zero for all statistical uncertainties.

MTD	estimate	$a$	$n$
Standard	$E_{\text{shift}} \approx 0$	$6.177 \pm 0.005$	$0.5047 \pm 0.0009$
	$\sigma_g^2 \approx 0$	$102.1 \pm 0.8$	$0.250 \pm 0.004$
Optimized	$E_{\text{shift}} \approx 0$	$4.405 \pm 0.002$	$0.4999 \pm 0.0005$
	$\sigma_g^2 \approx 0$	$103.5 \pm 0.6$	$0.243 \pm 0.002$
Realistic	$E_{\text{shift}} \approx 0$	$7.5654 \pm 0.0002$	$0.50174 \pm 0.00006$
	$\sigma_g^2 \approx 0$	$128.1 \pm 0.3$	$0.259 \pm 0.001$

## Voigt profile - 110 K plasma potential - reduced tritium column density

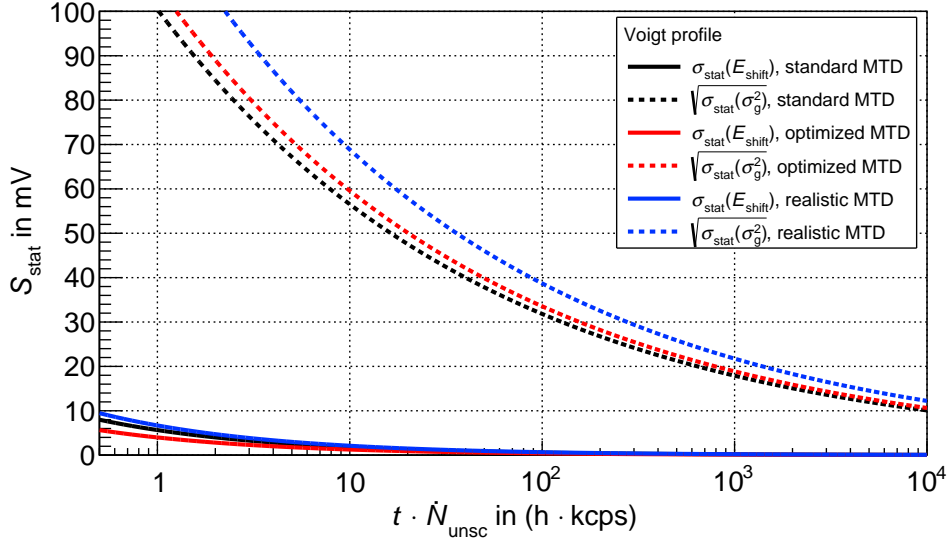


Figure 4.15.: Statistical sensitivity for the parameters of the Voigt profile with null hypothesis of 110 K plasma simulation and column density  $\rho d_{\text{Tr}} = 5 \cdot 10^{20} \frac{1}{\text{m}^2}$ : Due to the normalisation to  $\dot{N}_{\text{unsc}} = 1$  kcps the differences in sensitivities compared to those for the higher tritium column density are marginal. However, the normalisation implies a lower krypton column density, which can be read off figure 4.8 to be  $c_K = 0.71$ .

Table 4.8.: **Voigt profile: statistical sensitivities -  $L_3$  - 110 K potential - reduced column density**

In the case of reduced tritium column density, the fits for the realistic measurement time converge, but the parameter estimate on  $\sigma_g$  is unstable. However, reducing the tritium column density and including the step of singly scattered electrons into the MTD leads to a better accordance with the expectation of  $\sigma(V) = 7.68$  mV and  $\langle V \rangle = 21.36$  mV.

The values of  $n$  indicate that  $E_{\text{shift}}$  and  $\sigma_g^2$  linearly enter the  $\chi^2$  function and that the corresponding likelihood is Gaussian.

MTD	estimates	$a$	$n$
Standard	$E_{\text{shift}} = 20.92$ meV	$5.653 \pm 0.003$	$0.4982 \pm 0.0004$
	$\sigma_g^2 = (4.87$ meV) $^2$	$100.4 \pm 0.3$	$0.250 \pm 0.002$
Optimized	$E_{\text{shift}} = 20.91$ meV	$3.9924 \pm 0.0009$	$0.4993 \pm 0.0002$
	$\sigma_g^2 = (5.13$ meV) $^2$	$105.8 \pm 0.3$	$0.250 \pm 0.001$
Realistic	$E_{\text{shift}} = 20.90$ meV	$6.692 \pm 0.006$	$0.5002 \pm 0.0006$
	$\sigma_g^2 \approx (6.56$ meV) $^2$	$122.51 \pm 0.08$	$0.2502 \pm 0.0004$

## Rectangular model - 110 K plasma potential - nominal tritium column density

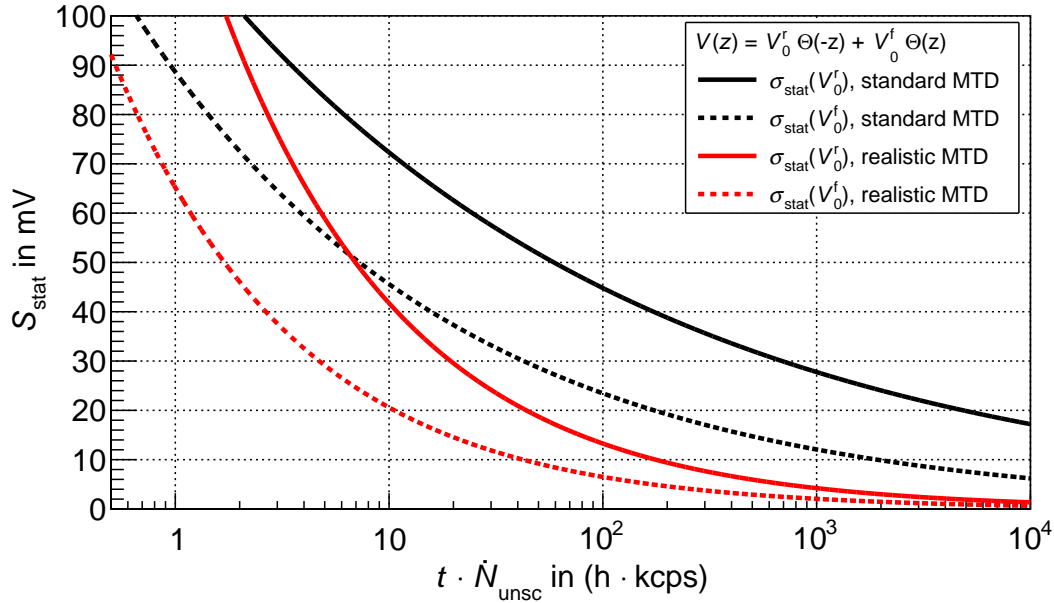


Figure 4.16.: Statistical sensitivity on the parameters of the rectangular model with the null hypothesis of 110 K plasma potential simulation: For both shown measurement time distributions, the front part of the WGTS plasma potential is measurable with a higher sensitivity. Including the step of one time scattered electrons into the MTD drastically increases the overall sensitivity (red compared to black). In this case the sensitivity on both parameters is below 10 mV within a 10 h measurement with  $\dot{N}_{\text{unsc}} = 0.1$  Mcps unscattered rate.

Table 4.9.: **Rectangular model: statistical sensitivities -  $L_3$  - 110 K potential**

For the standard MTD, the parameter estimates on the front and rear part potential showed arbitrary results in the range of 20 mV. The values of  $n$  indicate, that either the likelihood is not Gaussian or that the model parameters are highly correlated. By including the step of singly scattered electrons, the mean potential estimate for front and rear obey values, which are  $\approx 2\%$  smaller than the true values of  $V_0^r = 27.8$  mV and  $V_0^f = 14.9$  mV. The values obtained for  $n$  indicate a perfect linear formulation of the problem.

MTD	estimate	$a/\text{mV}$	$n$
Standard	$V_0^r \approx 20$ mV	$116.7 \pm 5.9$	$0.21 \pm 0.01$
	$V_0^f \approx 18$ mV	$89 \pm 4$	$0.29 \pm 0.01$
Realistic	$V_0^r = 27.3$ mV	$131.3 \pm 1.5$	$0.498 \pm 0.004$
	$V_0^f = 14.7$ mV	$65.2 \pm 0.3$	$0.501 \pm 0.001$

Linear model - 110 K plasma potential - nominal tritium column density

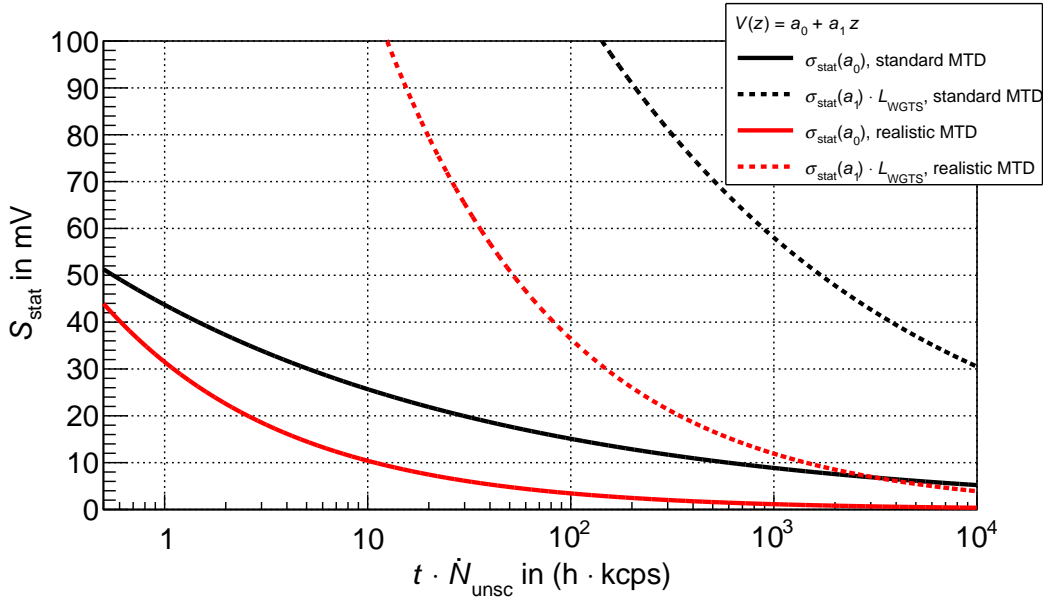


Figure 4.17.: Statistical sensitivity on the parameters of the linear model with the null hypothesis of 110 K plasma potential: When the step of scattered electrons is not included, the sensitivity on the slope  $a_1$  falls below 10 mV only for an experimentally unachievable large number of total counts. The constant part of the potential  $a_0$  will be measurable only with an unscattered rate in the order of  $\dot{N}_{\text{unsc}} = 0.1$  Mcps. Including the step of singly scattered electrons into the measurement time distribution drastically enhances the sensitivities. However, even in this case measuring the slope in a feasible time of 10 h will require a rate of  $\dot{N}_{\text{unsc}} = 1$  Mcps electrons.

Table 4.10.: **Linear model: statistical sensitivities -  $L_3$  - 110 K potential**

In the case of the standard measurement time distribution, the parameter estimates on the linear model are not stable for different measurement times. The values of  $n$  indicate that the problem is not linearly formulated. Including the step of one time scattered electrons into the measurement time distribution yields parameter estimates, which differ about  $\approx 2\%$  from the true values of  $a_0 = 21.25$  mV and  $a_1 = -2.22$  mV. The values of  $n$  indicate a perfectly Gaussian shape of the likelihood.

MTD	observable	$a$	$n$
Standard	$a_0 \approx 21$ mV	$44 \pm 1$	$0.23 \pm 0.01$
	$a_1 \approx -2$ mV/m	$399.4 \pm 12.9$	$0.28 \pm 0.02$
Realistic	$a_0 = 20.88$ mV	$31.49 \pm 0.09$	$0.481 \pm 0.003$
	$a_1 = -2.256$ mV/m	$340 \pm 1$	$0.485 \pm 0.003$

## 4.5. Systematic Uncertainties

Naturally systematic errors represent a fundamental limit on the overall obtainable sensitivity. In table 4.2 the relevant operational parameters for the krypton-83m mode are listed along with their projected uncertainties. The influence of these uncertainties on the krypton-83m mode measurements shall be discussed in the following.

### 4.5.1. Uncertainty of the WGTS Cryostat Temperature

Due to experimental limitations at  $T \approx 110$  K the temperature sensors can not be individually calibrated. This might lead to a temperature uncertainty in the few K range. Naturally the question arises if the strict requirements on the temperature accuracy of tritium mode ( $\Delta T/T < 2 \cdot 10^{-3}$ , see table 2.1) have to be met also in krypton mode. This is analysed in the following.

The projected dominant influence of the temperature on the krypton-83 mode measurement is due to Doppler effect. Correspondingly, only the Voigt profile has been chosen for the systematic study, since it is directly related to a broadening of the spectrum. As it is discussed in section 4.6.2 broadening effects are found to be of little relevance for the investigation of WGTS potential models, justifying this restriction.

The temperature uncertainty is modelled as a constant shift of the total WGTS temperature (no effects due to different temperature profiles are considered). The krypton-83m spectrum is measured with the standard measurement time distribution shown in figure 4.9. The temperatures in the toy measurements are deflected in a large range of  $\pm 20$  K around central temperature of  $T = 110$  K, which is taken to be the assumed temperature in the theoretical spectrum simulation.

The simulation and a linear fit can be found in figure 4.18 for the Gaussian broadening  $\sigma_g^2$  of the Voigt profile, showing a perfect linear scaling over a large temperature range. The same can be found for  $E_{\text{shift}}$ , where the resulting fits of the slope yield

$$\frac{\sigma_{\text{syst}}(\sigma_g^2)}{(\text{meV})^2} = 33.9 \cdot \frac{\Delta T}{\text{K}} \quad \text{and} \quad \frac{\sigma_{\text{syst}}(E_{\text{shift}})}{\text{meV}} = 1.7 \cdot 10^{-2} \frac{\Delta T}{\text{K}}. \quad (4.19)$$

For  $\Delta T = 2.94$  K one obtains a systematic uncertainty of  $\sqrt{\sigma_{\text{syst}}(\sigma_g^2)} = 10$  meV, which is equal to the demanded sensitivity.

### Discussion

Following the discussion in section 2.2.1 statistical and systematic error can be summed quadratically

$$\sigma_{\text{tot}}(\sigma_g^2) = \sqrt{\sigma_{\text{stat}}^2(\sigma_g^2) + \sigma_{\text{syst}}^2(\sigma_g^2)}. \quad (4.20)$$

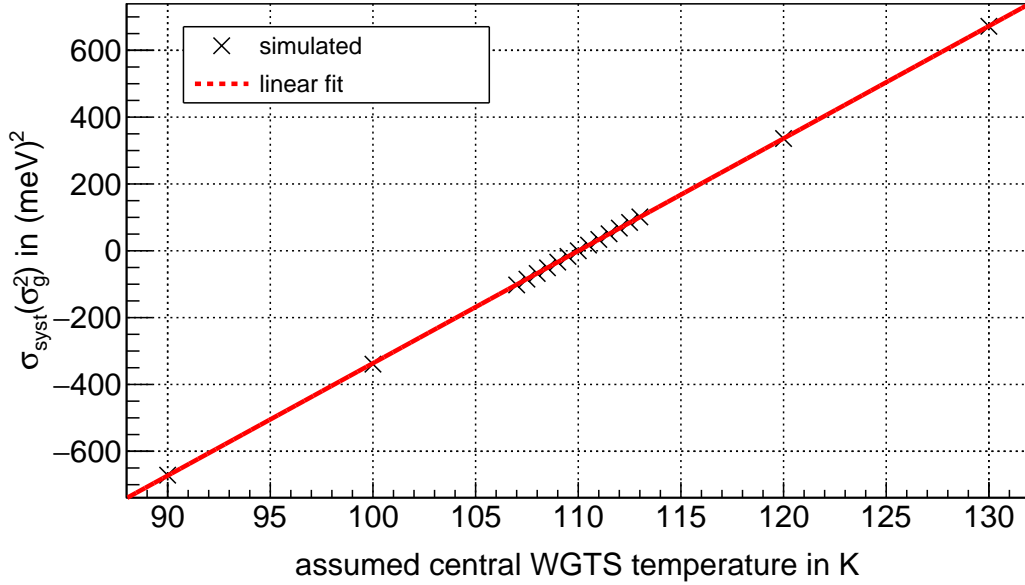


Figure 4.18.: Systematic shift of the Gaussian broadening parameter squared  $\sigma_g^2$  with an uncertainty in the temperature of the WGTS cryostat: The dependency is perfectly linear over a broad interval of temperatures. The true temperature present in the toy measurement is 110 K.

If both are taken equal to  $\sqrt{\sigma_{\text{stat}}(\sigma_g^2)} = \sqrt{\sigma_{\text{syst}}(\sigma_g^2)} = 10 \text{ meV}$  one obtains a deterioration of the total uncertainty by a factor  $\sqrt[4]{2}$  to  $\sqrt{\sigma_{\text{tot}}(\sigma_g^2)} = 12 \text{ meV}$ . Clearly this deterioration is only of minor importance. It can be concluded, that the systematic effect of an unknown central WGTS temperature play a minor role, if the uncertainty does not exceed 3 K.

### Theoretical Expectation

The resulting temperature dependence of the broadening parameter  $\sigma_g$  can fully be explained by an unaccounted Doppler effect. To understand this it is important to consider that the broadening function of the electron spectrum is no Maxwellian distribution like the thermal velocity of the gas, since only the components in forward direction are important. It has been shown in [Höt12] that the broadening function, which has to be convoluted with the spectrum in non relativistic approximation, can be written as

$$g(\Delta E) = \frac{1}{\sqrt{2\pi}\sigma_D} \exp\left[-\frac{1}{2}\left(\frac{\Delta E}{\sigma_D}\right)^2\right]. \quad (4.21)$$

Since this is a Gaussian distribution, the Doppler effect completely mimics the potential inhomogeneities, if the latter are described to be Gaussian like in this particular analysis.

The Doppler width is found to be

$$\sigma_D = \sqrt{2 \frac{m_e}{M_{\text{Kr}}} E k_B T} . \quad (4.22)$$

Here  $m_e$  is the electron mass,  $M_{\text{Kr}}$  the mass of the emitter (here taken to be krypton),  $E$  the electron energy and  $k_B$  the Boltzmann constant. The linear scaling of  $\sigma_D^2$  with temperature can instantly be seen and the constant  $k$  of  $d\sigma_D^2 = k dT$  is easily found to be  $k = 34.8 \cdot \frac{(\text{meV})^2}{\text{K}}$  for a mean energy of  $E_{L3} \approx 30475$  eV. This is in good agreement with equation 4.19, where the deviations should be attributed to secondary effects also included in the simulation (bulk velocity, changes of the gas profile and also relativistic effects). It is worth mentioning that the broadening depends on the electron energy, therefore it will be smaller for the  $K$  line if no additional effects occur.

The shift of the mean is more difficult to understand. To first order the mean energy of the electrons is thought to be unchanged by the Doppler effect, since the above Gaussian equation 4.21 is centred at zero. This is due to the isotropic motion of the gas, which has no effect on the mean energy of the electrons. A possible explanation, however, might be an asymmetric change of the spectral shape due to the bulk velocities of front and rear part of the WGTS: If the measured number of electrons stemming from those parts was equal, the bulk velocity would only lead to an additional broadening of the spectrum. However, since more electrons of the front part are included in the measurement time distribution due to inelastic scattering, the broadening will be asymmetric, leading to a shift of the line mean to higher energies.

It can be concluded that the uncertainty of temperature in krypton-83m mode plays a minor role in this analysis. In contrast to tritium measurements, where the excited final state distribution of the  $\beta$  emitter strongly depend on the temperature and modify the spectrum shape, here only the Doppler effect is relevant.

#### 4.5.2. Uncertainty of the Inelastic Cross Section

The impact of an uncertainty of the inelastic cross section  $\sigma_{\text{tot}}$  on the krypton-83m mode measurements was analysed using the rectangle model presented in section 4.1.2. The analysis was restricted to a plasma potential model, since inelastic scattering is a key ingredient for measurements of the WGTS plasma potential with axial resolution, as it is discussed in section 4.6.1.

The total number of counts is chosen in a way, that a statistical sensitivity on the model parameters of 5 mV for the mean rear potential  $V_0^r$  and 10 mV on the mean front potential  $V_0^f$  is obtained (following the results shown in table 4.9) in the case were the true cross section is used.

However, even for a small fixed deflection of  $\sigma_{\text{tot}}$  of 0.5 % compared to the true value of  $\sigma_{\text{tot}} = 2.106 \cdot 10^{-22} \text{m}^2$  in simulations no valid minimum could be reliably found by the fit algorithm, indicating, that the model does not describe the toy measurement data.

The scattering cross section was chosen as additional free parameter of the model, which turned out to be very successful, as can be seen in figure 4.19. The overall sensitivity on

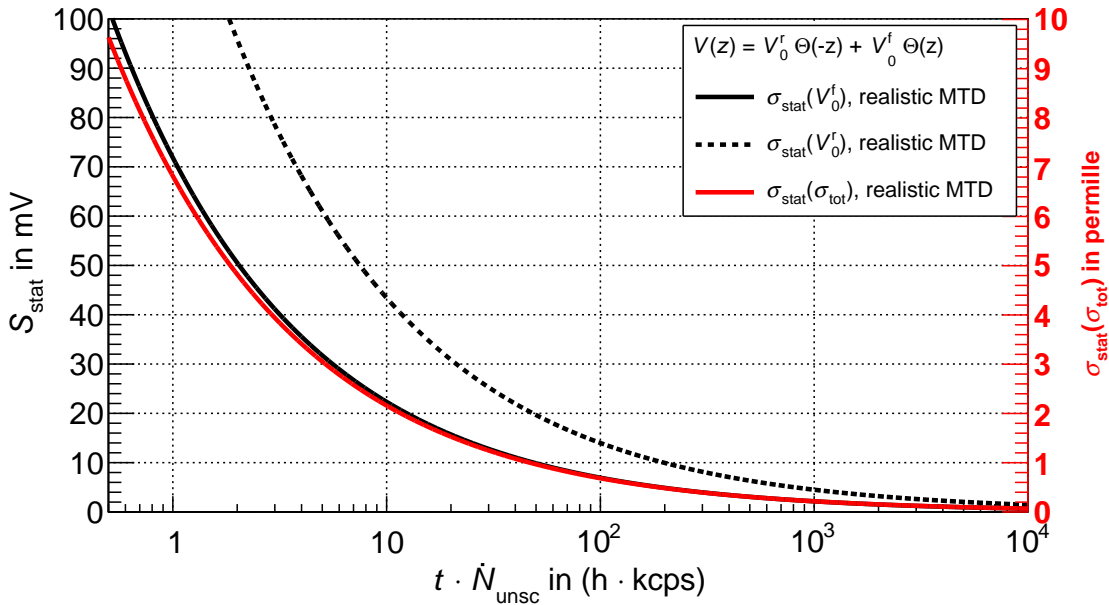


Figure 4.19.: Sensitivity on the 110 K plasma potential simulation with the rectangular model and the inelastic cross section as additional free parameter: as explained in the text, the sensitivity on  $\sigma_{\text{tot}}$  should be read as the sensitivity on the product of  $\sigma_{\text{tot}}$  and the tritium column density  $\rho d_{\text{Tr}}$ .

the parameters of the plasma potential model do not strongly decrease, while the statistical uncertainty of the cross section parameter is on the permille level with only half an hour of measurement time at unscattered rate  $\dot{N}_{\text{unsc}} = 1$  kcps.

This simulation uses a fixed and known tritium column density and profile. Since  $\sigma_{\text{tot}}$  and  $\rho d_{\text{Tr}}$  do enter as a product in the scattering probabilities (visible in equation 4.14) it is likely, that not the statistical uncertainty of  $\sigma_{\text{tot}}$  can be determined to this level, but the statistical uncertainty of this product. This is very much comparable to electron gun measurements (section 2.1).

Thus, this simulation shows, that measurements with krypton-83m mode do not necessarily require separate electron gun measurements to determine the product of column density and inelastic cross section, given that the  $z$ -dependency of the gas profile is well understood.

## 4.6. Discussion

Initially, the analysis carried out in this work was focused on the determination of the WGTS plasma potential inhomogeneity by measuring a line shape distortion of krypton-83m conversion lines, a procedure frequently proposed and used in other experiments ([KAT04; Hua10; Bel+08]).

However, in the case of KATRIN, this approach was revealed not to deliver a useful measure for the potential inhomogeneity, but produces ambiguous results, as presented in section 4.4. In particular, there are large influences of the tritium column density and the measurement time distribution on the sensitivity and, most importantly, on the estimates of the parameters of the used models. The parameter estimates and the true values are contrasted in table 4.11 for the potential models and in table 4.12 for the Voigt profile. In general, the findings can be summarised as follows:

- **Tritium column density:** For nominal column density the Voigt profile does not describe the plasma potential according to expectation, since the parameter estimates are too small and the model fits do not converge for measurement time distributions which include the step of singly scattered electrons. On the other hand, lowering the total column density is beneficial for the Voigt profile, since it raises the statistical sensitivity and at the same time the parameter estimates approach the expectation. On the other hand, though, it drastically lowers the sensitivity of the plasma potential models to a point where the fits do not converge any more.
- **Measurement time distribution:** If the step of singly scattered electrons is not included in the measured retarding potential interval large deviations appear between the parameter estimates of the potential models and the true values. By including the singly scattered electrons, the differences fall below 2%. However, in this case the description with the Voigt profile is only possible for a reduced column density.

All of these observations can be explained by inelastic electron scattering, which leads to an additional modification of the spectrum shape. Thereby it enforces a position resolved measurement of the WGTS plasma potential, while prohibiting the measurement of the total inhomogeneity through the broadening of a single krypton-83m conversion line. Thus, in addition to this broadening, it is a second process which provides sensitivity on the WGTS potential, and it is dominant for nominal tritium column density.

When the effect of inelastic scattering is taken into account, the results of the sensitivity studies on the krypton-83m mode measurements presented in this work become easily explainable, which is provided in section 4.6.1.

Furthermore it is possible to calculate the results for the parameter estimates of the plasma potential models even on a quantitative basis using a simple analytical model, which is reduced to the essential physics. It substantiates the importance of inelastic electron scattering for krypton-83m measurements, while simultaneously providing a possible explanation for the smallness of the estimates on the broadening parameter  $\sigma_g$ . This analytical model, the *Minimal Scattering Potential Model* MSPM is presented in section 4.6.2.

#### 4. Simulation Studies of the $^{83m}\text{Kr}$ -Mode Sensitivity on the Tritium Source Plasma Potential

Finally, it is concluded that the dominance of inelastic scattering for providing sensitivity on the WGTS plasma potential is not restricted to krypton-83m mode, but that it will also be strongly relevant in neutrino mass measurements, which is discussed in section 4.6.3.

Table 4.11.: **Potential model parameter estimates and true values for the 110 K plasma potential simulation**

The true values are derived from the direct fits, shown in section 4.1. The estimates, to be obtained in an actual krypton-83m mode measurement, depend on the tritium column density (shown only for  $\rho d_{\text{Tr}} = 5 \cdot 10^{21} \frac{1}{\text{m}^2}$ ) and on the measurement time distribution (shown in figure 4.9).

For the standard MTD, differences up to 40 % appear. In case of the realistic MTD, the differences are reduced to 2 %. These remaining differences are of principle nature for this kind of measurements due to a physical weighting of the potential, which is discussed in section 4.6.2.

model parameter	true value	estimate	
		standard MTD	realistic MTD
$V_0^r$	27.8 mV	$\approx 20$ mV	27.3 mV
$V_0^f$	14.9 mV	$\approx 18$ mV	14.7 mV
$a_0$	21.25 mV	$\approx 21$ mV	20.88 mV
$a_1$	-2.22 mV/m	$\approx -2$ mV/m	-2.256 mV/m

Table 4.12.: **Voigt profile parameter estimates and true values for the 110 K plasma potential simulation**

For nominal tritium column density the Voigt profile does not sufficiently characterise the total plasma potential: The parameter estimates are significantly smaller than expected. However, a reduction of the total column density is strongly beneficial.

model parameter	expected value in meV	$\rho d_{\text{Tr}}$ in $10^{20} \frac{1}{\text{m}^2}$	estimate in meV		
			standard MTD	optimised MTD	realistic MTD
$E_{\text{shift}}$	21.36	50	18.86	18.85	-
		5	20.92	20.91	20.90
$\sigma_g$	7.68	50	$\lesssim 3.36$	$\lesssim 1.5$	-
		5	4.87	5.13	$\approx 6.56$

#### 4.6.1. Impact of Inelastic Scattering on Krypton-83m Measurements

The impact of inelastic scattering on the krypton-83m mode measurements is revealed in figure 4.16. The mean plasma potential in the front part of the WGTS  $V_0^f$  can in general be measured with a higher sensitivity than that in the rear part  $V_0^r$  and the inclusion of the step of singly scattered  $L_3$  electrons into the measurement interval drastically increases the sensitivity on both model parameters.

Inelastic scattering provides axial sensitivity according to the process described in section 4.3. This process basically entails two effects, which are of major relevance for the krypton-83m mode measurements:

- **Potential model sensitivity:** Since the contributions of electrons from different parts of the WGTS to the step of unscattered and singly scattered electrons are not equal, it is possible to measure any two parameter plasma potential model only by determining the position of the means of these two steps. Thus, the differing deviation of the means to their intrinsic values contains information on the inhomogeneity of the plasma potential.
- **Shadowing of certain parts of the WGTS:** In the case where only one step is included in the measurement time distribution, only a constrained window of the WGTS is actually observed. Thus, the broadening of a single step does not contain the information on the total inhomogeneity of the plasma potential.

All measurements at nominal column density are dominated by this process, which is evident by the following observations:

- The Voigt profile model fit does not converge if both steps are included, since they are not shifted by the same energy values. Thus, the modelling of the spectrum with only one shift is already wrong in leading order.
- The parameter estimates obtained by measurements including only the step of unscattered electrons are wrong, since mainly the front part of the WGTS is actually visible.
- The parameter estimates obtained by measurements including both spectrum steps approach the expectation for the two-parameter potential models. In case of more free parameters like in the full ellipse model, additional information using both line broadenings has to be exploited, which is only possible for very long measurement times.
- The sensitivity to the front part of the WGTS is higher, since the step of unscattered electrons has the larger signal to noise ratio. In addition, the step of singly scattered electrons is broader, due to the spread of the energy loss function.
- When including singly scattered electrons, the scaling of the sensitivities with the total number of counts is as expected for linear formulated problems (visible in the exponents  $n$ ). This implies a dominant measurement of the line means which linearly enter the  $\chi^2$  statistic, in contrast to the line widths which enter quadratically. The linearity is also the reason why measurements including the singly scattered electrons are in general more sensitive.

As column density is reduced, the dominance of inelastic scattering related axial sensitivity vanishes, due to the lower scattering probabilities. The WGTS becomes a homogeneous system:

- The Voigt profile now reflects more accurately the mean and inhomogeneity of the total plasma potential.
- Plasma potentials models can not be distinguished, since no information on the actual shape of the potential is visible in the resulting integrated spectrum<sup>8</sup>.

Thus, it is evident that krypton-83m mode measurements aiming to analyse the WGTS potential in a position-resolved matter rely on the measurement of electron inelastic scattering. On the other hand, it is also evident that a measurement of the total inhomogeneity of the plasma potential using a broadening of a single mono-energetic electron line will require the absence of inelastic scattering. Hence, both methods are complimentary and it depends on the column density experimentally available in krypton-83m mode measurements, which one can be used.

It should be stressed that the quantities related to the WGTS plasma potential which can actually be measured at krypton-83m conversion lines, to first order are the shift of the means. To second order, also the Gaussian broadenings of the lines are accessible. However, according to the results presented in section 4.4 even a measurement of the Gaussian broadenings requires a very large number of total counts. As a consequence, the measurements of third order effects like asymmetric broadenings is out of reach for realistic KATRIN krypton-83m mode measurements. Thus, the measurement of both the step of unscattered and singly scattered conversion electrons in principle enables a maximal four parameter description of the plasma potential.

Inelastic scattering qualitatively explains the dominant process for providing sensitivity on the plasma potential models. However, in all measurements the parameter estimates showed deviations from the true values. This is related to the way the physical potential is averaged in krypton-83m mode measurements, reflected in equations 4.1 and the corresponding discussion. In the case where the electron spectrum is quasi-monoenergetic the effect of this averaging can be analytically quantified, which is done in the following discussion.

#### 4.6.2. Minimal Scattering Potential Model

The *Minimal Scattering Potential Model* MSPM, developed in the context of this thesis, gives a quantitative description of the change of the observed integrated count rate as a function of the WGTS potential near the mean of the krypton-83m conversion line steps and the corresponding steps of singly scattered electrons. Following equation 3.1 for retarding energies above the tritium  $\beta$  spectrum endpoint, the integrated count rate can be written

---

<sup>8</sup>To give an explicit example: In case of vanishing inelastic scattering the WGTS can be described as symmetric to the injection point. Thus, it is impossible to distinguish potentials  $V(z)$  from  $V(-z)$  in the electron spectrum.

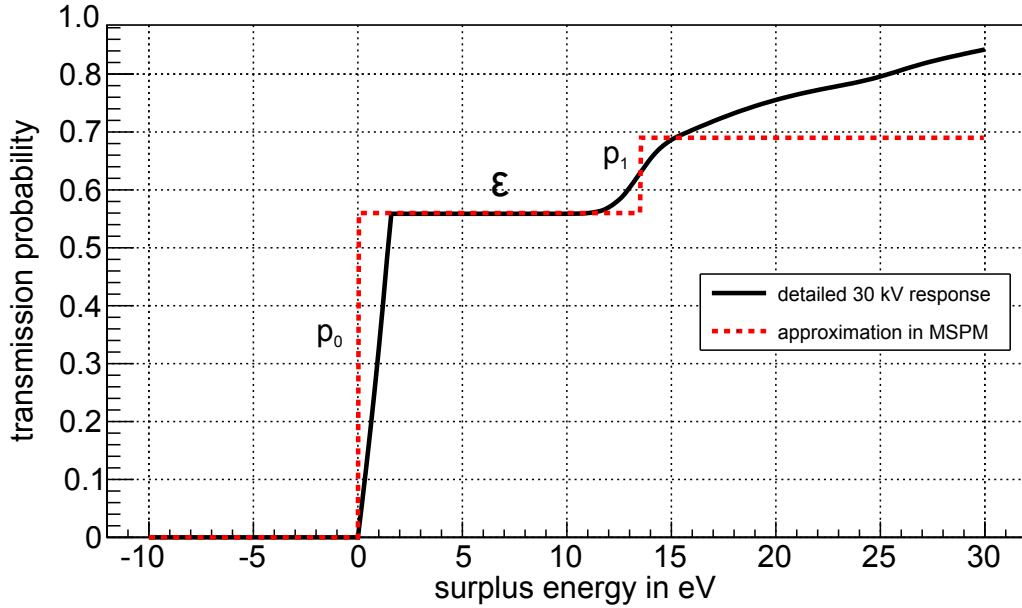


Figure 4.20.: Response as function of the surplus energy  $E - qU$  for the retarding potential of  $U = 30475$  kV: In the detailed response model the transmission edge at  $E - qU = 0$  and the edge due to single scattering at  $E - qU = \epsilon$  exhibit a finite width. Both are approximated with zero in the MSPM and the continuous energy loss for larger surplus energies is neglected, such that a description as sum of  $\Theta$  distributions is obtained. The transmission probabilities  $p_0$  and  $p_1$  are  $z$  dependent, where mean values averaged over the length of the WGTS are shown here.

as

$$\dot{N}(qU) = \epsilon_{\text{det}} \int_z \frac{dz}{L_{\text{WGTS}}} \frac{\Omega(z)}{4\pi} N^K(z) \int_{-\infty}^{\infty} dE \left( \frac{d\dot{N}}{dE} \right)_K R(E, qU_{\text{tot}}(z)), \quad (4.23)$$

where the sum over WGTS slices was replaced with an integral over the length of the WGTS  $L_{\text{WGTS}}$  and  $U_{\text{tot}}(z) \equiv U + V(z)$  was defined. Here  $U$  is the retarding potential of the spectrometer and  $V$  the plasma potential inside the WGTS.

As pointed out in section 4.6.1 the dominant process in the simulated krypton-83m mode measurements was the measurement of line means, which is a first-order process. Thus the analytical description can also be limited to first order, implying that any broadening effects can be neglected. This corresponds to the approximation of the response function as a sum of  $\Theta$  distributions (figure 4.20). Accordingly it is written as

$$R(E, qU_{\text{tot}}(z)) = p_0(z) \cdot \Theta(E - qU_{\text{tot}}(z)) + p_1(z) \cdot \Theta(E - qU_{\text{tot}}(z) - \epsilon), \quad (4.24)$$

with the probability of no scattering  $p_0$ , single scattering  $p_1$  and minimal energy loss  $\epsilon$ .

The integrated rate  $\dot{N}$  then reads

$$\dot{N}(qU) = A^K \epsilon_{\text{det}} \int_z \frac{dz}{L_{\text{WGTS}}} \frac{\Omega(z)}{4\pi} N^K(z) [p_0(z) B(qU_{\text{tot}}(z)) + p_1(z) B(qU_{\text{tot}}(z) + \epsilon)] , \quad (4.25)$$

with the definition

$$B(X) \equiv \int_X^\infty \left( \frac{d\dot{N}}{dE} \right)^K dE , \quad (4.26)$$

which corresponds to the integral rate with filter energy  $X$ . If the  $z$  dependency of  $X$  is taken into account, it is the integrated rate produced at the axial position  $z$ .  $A^K$  is the total activity of the measured line.

Two further approximations are made in considering only one krypton-83m conversion line, which will only influence the signal to noise ratio, and in neglecting the Doppler effect which is of second order.

Thus, the spectrum is described as a Lorentzian (equation 3.6) with line mean  $E_{\text{mean}}$  and width  $\Gamma$ . To compensate for the approximations of infinitesimal width of the response function steps and Doppler effect,  $\Gamma$  can be replaced by an effective width  $\hat{\Gamma}_i$  combining all broadening effects. The latter are different for  $i = 0$  scattering and  $i = 1$  scattering. This procedure contains the approximation that the line shape is still Lorentzian after undergoing broadening. However, the knowledge of  $\hat{\Gamma}_i$  is only necessary for the calculation of higher order effects.

The Lorentzian Profile can be integrated analytically, yielding

$$B(X) = \frac{1}{2} - \frac{1}{\pi} \arctan \left[ \frac{2}{\hat{\Gamma}} (X - E_{\text{mean}}) \right] . \quad (4.27)$$

In the following, equation 4.25 shall be evaluated at retarding potentials near the line mean  $qU - q\Delta U = E_{\text{mean}}$  and the scattered line mean  $qU - q\Delta U = E_{\text{mean}} - \epsilon$ , with  $|q\Delta U| \lesssim \hat{\Gamma}$ . To do so, the separation of the steps by  $\epsilon \approx 13$  eV and the smallness of  $V(z) \ll \hat{\Gamma}$  is exploited. Three terms have to be considered, which read

$$\begin{aligned} B(E_{\text{mean}} + qV(z) + q\Delta U) &= \frac{1}{2} - \frac{1}{\pi} \arctan \left[ \frac{2}{\hat{\Gamma}} (qV(z) + q\Delta U) \right] \\ B(E_{\text{mean}} + qV(z) + q\Delta U - \epsilon) &= \frac{1}{2} - \frac{1}{\pi} \arctan \left[ \frac{2}{\hat{\Gamma}} (qV(z) + q\Delta U - \epsilon) \right] \stackrel{|\epsilon - q\Delta U| \gg \hat{\Gamma}}{\approx} \frac{1}{2} + \frac{1}{2} = 1 \\ B(E_{\text{mean}} + qV(z) + q\Delta U + \epsilon) &= \frac{1}{2} - \frac{1}{\pi} \arctan \left[ \frac{2}{\hat{\Gamma}} (qV(z) + q\Delta U + \epsilon) \right] \stackrel{|\epsilon + q\Delta U| \gg \hat{\Gamma}}{\approx} \frac{1}{2} - \frac{1}{2} = 0 . \end{aligned} \quad (4.28)$$

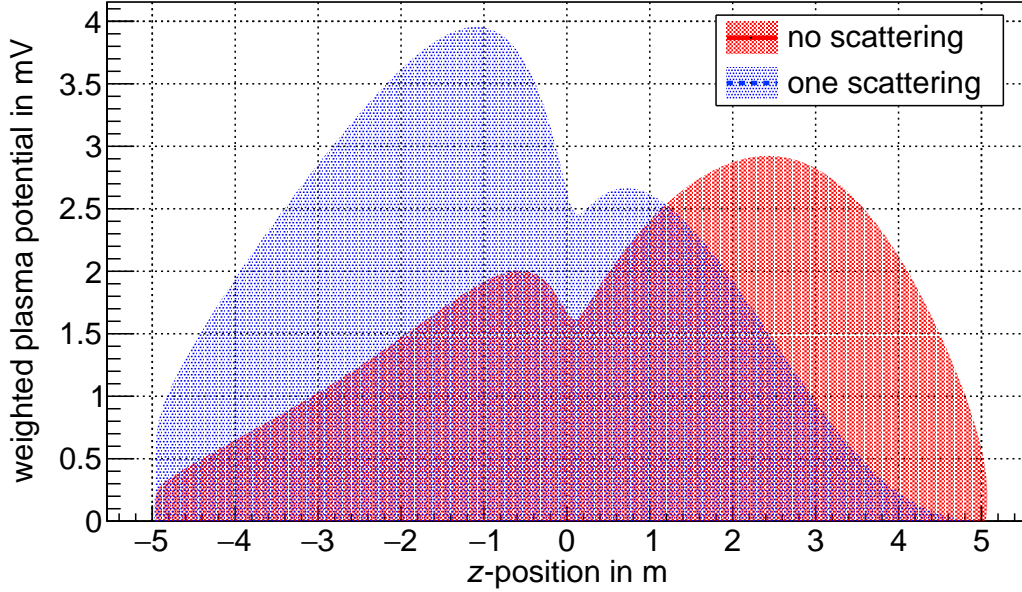


Figure 4.21.: Weighted 110 K plasma potential following equation 4.32: The observable mean potentials, which are measured at the unscattered and scattered integrated krypton-83m conversion electron steps, are the normalized integral over potential, acceptance angle, gas profile and scattering probability with respect to the  $z$  coordinate, depicted by the coloured areas.

Hence, for the integrated rates in the vicinity of the steps one obtains

$$\begin{aligned} \dot{N}(E_{\text{mean}} + q\Delta U) &= A^K \epsilon_{\text{det}} \int_z \frac{dz}{L_{\text{WGTS}}} \frac{\Omega(z)}{4\pi} N^K(z) p_0(z) \left( \frac{1}{2} - \frac{1}{\pi} \arctan \left[ \frac{2}{\hat{\Gamma}} (qV(z) + q\Delta U) \right] \right) \\ \dot{N}(E_{\text{mean}} + q\Delta U - \epsilon) &= A^K \epsilon_{\text{det}} \int_z \frac{dz}{L_{\text{WGTS}}} \frac{\Omega(z)}{4\pi} N^K(z) \left( p_0(z) \right. \\ &\quad \left. + p_1(z) \left\{ \frac{1}{2} - \frac{1}{\pi} \arctan \left[ \frac{2}{\hat{\Gamma}} (qV(z) + q\Delta U) \right] \right\} \right). \end{aligned} \quad (4.29)$$

Subtracting all quantities which are independent of the WGTS potential, one finally obtains for the change of the integrated count rate with  $V(z)$

$$\begin{aligned} \Delta \dot{N}(E_{\text{mean}} + q\Delta U) &= -A^K \epsilon_{\text{det}} \frac{1}{\pi} \int_z \frac{dz}{L_{\text{WGTS}}} \frac{\Omega(z)}{4\pi} N^K(z) p_0(z) \arctan \left[ \frac{2}{\hat{\Gamma}_0} (qV(z) + q\Delta U) \right] \\ \Delta \dot{N}(E_{\text{mean}} + q\Delta U - \epsilon) &= -A^K \epsilon_{\text{det}} \frac{1}{\pi} \int_z \frac{dz}{L_{\text{WGTS}}} \frac{\Omega(z)}{4\pi} N^K(z) p_1(z) \arctan \left[ \frac{2}{\hat{\Gamma}_1} (qV(z) + q\Delta U) \right]. \end{aligned} \quad (4.30)$$

The basic finding of the MSPM is that for the krypton-83m mode the variation of the observable (viz., the integrated count rate) is proportional to the weighted integral of the

Table 4.13.: **Measurable mean and standard deviation of the 110 K plasma potential.**

The values have been calculated following equation 4.32 using the standard  $z$ -profiles for 110 K. Thus,  $\langle V_i \rangle$  are the estimated mean potentials, when only the step of  $i$  time scattered electrons is measured. The accordance with the Voigt estimate for  $i = 0$  from a detailed simulation (table 4.6) is on the permill level. The  $\sigma_i(V)$  are just upper limits of the standard deviation, since the actual line shape has been neglected.

scatterings $i$	$\langle V \rangle_i$	$\sigma_i(V)$
0	18.83 mV	6.05 mV
1	22.72 mV	7.05 mV

arc tangent of the potential, where the weights are provided by all  $z$  dependent quantities:

$$\Delta \dot{N}(V) \propto \int_z \frac{dz}{L_{\text{WGTS}}} \frac{\Omega(z)}{4\pi} N^K(z) p_i(z) \arctan \left[ \frac{2}{\hat{\Gamma}_i} qV(z) \right]. \quad (4.31)$$

Here a measurement directly at the mean ( $q\Delta U = 0$ ) has been considered (see appendix A.1 for a more detailed discussion).

The dependency on the arc tangent is directly related to the line shape of the conversion electron spectrum. The change of the line shape will consequently depend on exponents of  $\frac{qV(z)}{\hat{\Gamma}/2}$ , which are strongly dominated by the leading order, due to the smallness of the potential.

Thus, the linear approximation of the arc tangent is completely sufficient. This leads to the finding of the observable mean potential, when measuring at the step of  $i$ -time scatterings

$$\langle V \rangle_i = \frac{\int_z dz \Omega(z) N^K(z) p_i(z) V(z)}{\int_z dz \Omega(z) N^K(z) p_i(z)}. \quad (4.32)$$

The observable standard deviation  $\sigma_i(V)$  of the potential can now be calculated as

$$\sigma_i(V) = \sqrt{\langle V^2 \rangle_i - \langle V \rangle_i^2}. \quad (4.33)$$

The weighted 110 K plasma simulation can be seen in figure 4.21 and the corresponding values are found in table 4.13.

### Parameter Estimates of the Voigt Profile

The values in table 4.13 correspond to the estimates which are measurable with the Voigt profile at the step of  $i$  scatterings. The weighted standard deviations  $\sigma_i(V)$  are smaller than the non-weighted inhomogeneity of the potential. In addition, by neglecting the arc tangent the actual shape of the Lorentzian line has been linearly approximated. Thus, the

Table 4.14.: **Measurable parameter estimates of the potential models**

The values for the  $\langle f \rangle_i$  and  $\langle g \rangle_i$  have been computed following equation 4.32, using standard KATRIN krypton-83m mode conditions. The deviations of  $a$  and  $b$  compared to detailed simulations shown in table 4.11 are on the permill level.

Model	$\langle f \rangle_0$	$\langle g \rangle_0$	$\langle f \rangle_1$	$\langle g \rangle_1$	$a$	$b$
$V(z) = a + bz$	1	0.926 m	1	-0.789 m	20.92 meV	$-2.257 \frac{\text{meV}}{\text{m}}$
$V(z) = a \Theta(-z) + b \Theta(z)$	0.332	0.668	0.638	0.362	27.32 meV	14.61 meV

$\sigma_i(V)$  are upper limits in the case, where the momenta  $\langle V^2 \rangle$  are fully included in the signal. However, in the arc tangent higher orders will be strongly suppressed with exponents of  $\frac{qV(z)}{\hat{\Gamma}/2}$ .

Consequently, the naive approach present in equation 4.2 should be discarded. The averaging of the potential will naturally have to respect all  $z$  dependent quantities, leading to loss of information on the true shape. The non-weighted averages of the potential can not be obtained in krypton-83m measurements.

When using the above form of averaging, the constant of proportionality for  $E_{\text{shift}}$  and the mean potential in equation 4.1 is one. To estimate the constant in case of the Gaussian broadening parameter, further considerations are necessary which include the actual line shape.

#### Parameter Estimates of the Potential Models

In principle the effect of plasma potentials on the spectrum steps can be characterised to first order by the means, and to second order by the broadenings measured at step  $i$ . Both can be calculated by equations 4.32 and 4.33, respectively.

The values for the chosen 110 K plasma potential simulation are shown in table 4.13. Those values are averaged with the profiles of the scattering probabilities.

For a description using  $z$  dependent functions, one has to supply a model of the expected shape of the potential which uses no more than four parameters. However, in this analysis only two-parameter models were shown to converge in the used measurement times and consequently the broadenings  $\sigma_i(V)$  were of little relevance.

Thus, this is a  $2 \times 2$  problem, which can easily be solved analytically, if the provided potential model is parametrised linearly:

$$V(z) = af(z) + bg(z) , \quad (4.34)$$

with coefficients  $a, b$ , which should be measured, and known functions  $f(z), g(z)$ . Hence, the following system of equations is obtained:

$$\begin{pmatrix} \langle V \rangle_0 \\ \langle V \rangle_1 \end{pmatrix} = \begin{pmatrix} \langle f \rangle_0 & \langle g \rangle_0 \\ \langle f \rangle_1 & \langle g \rangle_1 \end{pmatrix} \quad (4.35)$$

which is easily solved for the coefficients

$$a = \frac{\langle V \rangle_0 \langle g \rangle_1 - \langle V \rangle_1 \langle g \rangle_0}{\langle g \rangle_1 \langle f \rangle_0 - \langle g \rangle_0 \langle f \rangle_1} \quad \text{and} \quad b = \frac{\langle V \rangle_1 \langle f \rangle_0 - \langle V \rangle_0 \langle f \rangle_1}{\langle g \rangle_1 \langle f \rangle_0 - \langle g \rangle_0 \langle f \rangle_1}. \quad (4.36)$$

The expected shape of the potential has to be weighted according to equation 4.32, which has been performed using standard gas, scattering and acceptance angle profiles.

The values for the potential models used in this analysis can be found in table 4.14. The general accordance to the parameter estimates obtained from detailed simulations (table 4.11) is on the permill level. Since no broadenings were considered, this is an evidence, that for nominal column density and measurement time distributions, which include inelastic scattered electrons, the first order processes is strongly dominant.

### Concluding Remarks

- **Approximations:** Basically any experimental broadening effects of the spectrum have been completely neglected (thermal effect, bulk velocity, transmission width, response function), as well as the background of further krypton-83m lines. It is evident from the comparison of analytical model and simulation, that these approximations have a minor influence on the means of the parameter estimates and only modify the statistical sensitivity.
- **Limited model discrimination:** Clearly a two-parameter description of the physical WGTS plasma potential involves the usage of  $z$ -averaged means, which do not carry any information on the detailed shape. If for example a fast oscillating plasma potential of the form  $V(z) = \cos(kz)(a\Theta(-z) + b\Theta(z))$  was assumed, the same output on  $a$  and  $b$  could be obtained for large  $k$ , as for  $k = 0$ . The basic quantities, measurable in krypton-83m mode measurements are the mean potentials in equation 4.32.
- **Deviations of measured estimates and true values:** The findings will be transferable to all stationary potentials of an inhomogeneity that is much smaller than the effective width of the measured line. For different potential shapes the deviations of the true values to the measurable values will be different.
- **Non-stationary processes:** No time dependent effects or plasma instabilities have been considered in this work. It is conceivable, that such effects may lead to additional Gaussian fluctuations in the signal, even if scattered electrons are included.

### 4.6.3. Impact on Neutrino Mass Analysis

The sensitivity studies presented in section 4.4 along with their quantitative explanation in the framework of the minimal scattering potential model shown in section 4.6.2 evidently reveal that inelastic scattering is the dominant process of providing sensitivity on the WGTS plasma potential models for krypton-83m measurements at nominal column density.

However, there is evidence that this finding also holds in KATRIN neutrino mass measurements close to the tritium  $\beta$  spectrum endpoint.

Table 4.15.: **Means and standard deviations of the plasma simulation, simulated at 30 K, for different weights**

For the standard measurement time distribution, which includes up to two time scattered electrons, the endpoint- and neutrino mass shift induced by the 30 K plasma potential simulation are  $\Delta E_0 = 2.58$  meV and  $\Delta m_\nu = -17.87$  meV, respectively. The endpoint shift is smaller than any of the given means of the potential and the neutrino mass shift is larger than any of the given standard deviations of the potential and even larger than the total inhomogeneity of the potential, measured minimum to maximum, of about  $\Delta V = 5$  mV.

weight	$\langle V \rangle$	$\sigma(V)$
1	3.42 mV	1.69 mV
$N^{\text{Tr}}(z)$	3.38 mV	1.48 mV
$N^{\text{Tr}}(z) \cdot p_0(z)$	2.65 mV	1.16 mV
$N^{\text{Tr}}(z) \cdot p_1(z)$	3.46 mV	1.41 mV
$N^{\text{Tr}}(z) \cdot p_2(z)$	4.06 mV	1.43 mV

As the discussion provided in the last chapter shows, in a measurement of the potential an integral over all  $z$  dependent quantities will have to be taken into account. Certainly this will also hold for the influence of the potential on the  $\beta$  spectrum, with the difference, that the influence of the individual scattering probabilities is not immediately apparent by eye.

In table 4.15 means and standard deviations of the 30 K plasma potential simulation shown in figure 3.10 are presented for different weights, defined by the  $z$ -dependent scattering probabilities and the gas density. Two-fold scattering is also shown, since it is included in the standard KATRIN measurement time distribution.

The induced neutrino mass shift for this potential obtained in simulations would be  $\Delta m_\nu^2 = -0.3 \cdot 10^{-3} \text{ eV}^2$ , which implies a Gaussian broadening of the  $\beta$  spectrum in the range of  $\sigma_\beta = 13$  meV, if equation 4.3 is used. This is very much larger than any of the given standard deviations and could possibly be explained by the fact that, as for the krypton-83m mode measurements, the broadening is not the dominant effect.

Further evidence can be found by restricting the measurement time distribution to a 9 eV interval below the endpoint, which excludes scattered electrons. In this case, the resulting shift of the endpoint is  $\Delta E_0 = 2.65$  meV and of the neutrino mass  $\Delta m_\nu = -4.66$  meV, which falls into the expected range.

Clearly this effect needs further quantification. Since the neutrino mass shift induced by a realistic plasma potential is found to be larger than expected, the krypton-83 mode renders to be even more important, even if not in the way, originally designed. Concrete possibilities of measurement, respecting the findings of this work, will be given in the next section.

Table 4.16.: **Total measurement time - 10 mV sensitivity - rectangular model**

A sensitivity on both parameters  $V_0^r$  and  $V_0^f$  of the rectangular model is reached within the stated total measurement times, depending on the krypton-83m integrated spectrum rate on the plateau of  $L_3$  line.

The given values apply for the full detector surface area.

rate	time
1 kcps	176 h
10 kcps	17.6 h
100 kcps	108 min
1 Mcps	10.6 min

Table 4.17.: **Total measurement time - 30 mV sensitivity - rectangular model**

For a sensitivity of 30 mV on the model parameters  $V_0^r$  and  $V_0^f$  the necessary measurement times are significantly shorter.

The given values apply for the full detector surface area.

rate	time
1 kcps	19.4 h
10 kcps	116 min
100 kcps	11.6 min
1 Mcps	70 s

## 4.7. Recommendations for $^{83m}\text{Kr}$ Mode Measurements

As pointed out in section 4.6.1 for nominal total column density reasonable krypton-83m mode measurements have to include the steps of unscattered and single scattered  $L_3$  electrons in the measured retarding potential interval.

The proposed model for analysis is the rectangular model

$$V(z) = V_0^r \Theta(-z) + V_0^f \Theta(z) ,$$

which allows for a quantitative assessment of the mean plasma potential in the front and rear side of the WGTS.

The required total measurement time when using a measurement time distribution comparable to the "realistic scenario" in figure 4.9 is given in table 4.17 for a 10 mV and in 4.16 for a 30 mV sensitivity, respectively. In each case, the sensitivity on the model parameter  $V_0^f$  is better. Detailed results can be found in section 4.4.

Accordingly, even when using a conservative estimate of the available count rate of 10 kcps on the unscattered plateau of the  $L_3$  line a 30 mV sensitivity will be achievable on both model parameters in a less than 2 hour measurement.



## 5. Conclusion and Outlook

In this thesis the  $^{83\text{m}}\text{Kr}$  mode of the KARlsruhe TRItium Neutrino (KATRIN) experiment has been studied. The KATRIN experiment aims to perform a kinematic measurement of the neutrino mass by precision spectroscopy of the tritium  $\beta$  decay spectrum at its kinematic endpoint of 18.6 keV with an unprecedented sensitivity of 200 meV (90 % C. L.). Reaching this ambitious goal requires careful control of the systematic uncertainties. One of the systematics related to the gaseous tritium source concerns the potential variation due to the plasma. The  $^{83\text{m}}\text{Kr}$  has been proposed for the quantification of this specific systematic.

For pre-measurement sensitivity studies and data analysis, a comprehensive model of the tritium source  $^{83\text{m}}\text{Kr}$  mode was developed within the KATRIN simulation framework during this work. This involved the simulation of both the three dimensional velocity and number density profiles of the krypton gas inside the source, as well as the energy spectrum of the conversion electrons. Ultimately, these extensions allowed to simulate realistic KATRIN  $^{83\text{m}}\text{Kr}$  mode conditions and measurements.

The implemented  $^{83\text{m}}\text{Kr}$  mode simulation model was used to investigate the sensitivity of KATRIN  $^{83\text{m}}\text{Kr}$  mode measurements on the plasma potential, which was modelled using two different approaches: motivated by the findings of previous works and experiments a Gaussian broadening  $\sigma_g$  of the krypton-83m spectrum was considered, which was assumed to reflect the total inhomogeneity of the plasma potential. In a complementary approach, approximate models for the shape of the plasma potential were developed and the sensitivity with respect to the parameters of these models was analysed. The analysis was carried out using a detailed simulation of the expected plasma potential as null hypothesis.

The results were ambiguous: In contrast to the initial expectation, the estimates on the Gaussian broadening parameter  $\sigma_g$  were smaller than the total inhomogeneity of the input plasma potential for nominal KATRIN measurement conditions.

Furthermore, it was found in simulations that the neutrino mass shift induced by a realistic, simulated plasma potential is considerably larger than the inhomogeneity of the potential might naively suggest. This leads to the conclusion that, in contrast to the initial proposal the Gaussian broadening parameter  $\sigma_g$  cannot be interpreted as an upper limit on the shift of the neutrino mass for nominal KATRIN measurement conditions.

However, the observations could be fully explained by electron inelastic scattering inside the tritium source, a process which provides axial sensitivity on the tritium source plasma potential. Since the electrons which scatter inelastically with the tritium gas loose at least an energy of 13 eV, the energy spectrum of the electrons can roughly be divided into 13 eV

intervals, which are related to electrons with different scattering multiplicity. Moreover, since the probability that a detected electron has been scattered depends on its emission point in the source due to the effective column density it has to traverse, these intervals can be roughly mapped onto different regions inside the gaseous source.

Hence, due to the axial dependent scattering probabilities in a measurement of the broadening of a single krypton-83m conversion step only a limited section of the tritium source is actually observed. This kind of measurement does not deliver a reasonable estimate on the size nor the inhomogeneity of the overall tritium source plasma potential.

Based on this finding, an alternative and at the same time more sensitive way of studying the plasma potential has been identified and quantified in this work: by measuring the mean energies of the step of unscattered and of the step of one time scattered electrons a plasma potential model with up to two free parameters can be tested. It was shown that  $^{83\text{m}}\text{Kr}$  mode measurements based on this process are feasible at KATRIN conditions and an analytical theory was developed, which enabled to calculate and to confirm the parameter estimates obtained in detailed simulations of the known input plasma potential on the permil level. This raises confidence in the understanding of the interplay between the scattering and energy loss in the extended gaseous source and the recovery of the plasma potential shape.

It can be concluded, that an identification and detailed explanation of the relevant mechanisms in KATRIN  $^{83\text{m}}\text{Kr}$  mode has been provided. Furthermore, the analytical description of the  $^{83\text{m}}\text{Kr}$  mode measurements indicates that, in principle, the observed electron spectrum shape could be tested against potential models with up to a maximum of four free parameters.

**Outlook:** A full quantification of the effect leading to the recovery of an unexpectedly large systematic will be required. The analytical model developed in the present work gives clear hints on the involved mechanisms and is thus a starting point for analysing and understanding actual data.

Practical recommendations for measurements testing the results of this study have been pointed out. It will be instructive to plan and conduct such a measurement program during the further commissioning phase of KATRIN.

# Bibliography

- [Abd+94] JN Abdurashitov et al. “Results from SAGE (The Russian-American gallium solar neutrino experiment)”. In: *Physics Letters B* 328.1 (1994), pp. 234–248. ISSN: 0370-2693.
- [Ade+14] PAR Ade et al. “Planck 2013 results. XVI. Cosmological parameters”. In: *Astronomy & Astrophysics* 571 (2014), A16–. ISSN: 0004-6361.
- [AMW86] MJ Assael, S Mixafendi, and William A Wakeham. “The viscosity and thermal conductivity of normal hydrogen in the limit of zero density”. In: *Journal of physical and chemical reference data* 15.4 (1986), pp. 1315–1322. ISSN: 0047-2689.
- [Ase+00] VN Aseev et al. “Energy loss of 18 keV electrons in gaseous T and quench condensed D films”. In: *The European Physical Journal D-Atomic, Molecular, Optical and Plasma Physics* 10.1 (2000), pp. 39–52. ISSN: 1434-6060.
- [Aug+12] M Auger et al. “Search for neutrinoless double-beta decay in Xe 136 with EXO-200”. In: *Physical Review Letters* 109.3 (2012), pp. 032505–.
- [Bab14] Martin Babutzka. “Design and development for the Rearsection of the KATRIN experiment”. PhD thesis. 2014,
- [Bah64] John N Bahcall. “Solar neutrinos. i. theoretical”. In: *Physical Review Letters* 12.11 (1964), pp. 300–.
- [Bam+72] Walter Bambynek et al. “X-ray fluorescence yields, Auger, and Coster-Kronig transition probabilities”. In: *Reviews of Modern Physics* 44.4 (1972), p. 716.
- [Bar02] Roger Barlow. “Systematic errors: Facts and fictions”. In: *arXiv preprint hep-ex/0207026* (2002),
- [BB67] Jo A Bearden and AF Burr. “Reevaluation of X-ray atomic energy levels”. In: *Reviews of Modern Physics* 39.1 (1967), p. 125. URL: <http://journals.aps.org/rmp/pdf/10.1103/RevModPhys.39.125>.
- [Bel+08] AI Belesev et al. “Investigation of space-charge effects in gaseous tritium as a source of distortions of the beta spectrum observed in the Troitsk neutrino-mass experiment”. In: *Physics of atomic nuclei* 71.3 (2008), pp. 427–436. URL: <http://link.springer.com/content/pdf/10.1134/S1063778808030046.pdf>.
- [Ber+12] T. Bergmann et al. “FPGA-based multi-channel DAQ systems with external PCI express link to GPU compute servers”. In: *Real Time Conference (RT), 2012 18th IEEE-NPSS*. 2012, pp. 1–5.
- [Bon03] J. Bonn. *WG(Kr-T)S exploring systematics with  $^{83m}\text{Kr}$  in the WGTS*. Internal presentation. KATRIN 6.TB, Mainz, July 8, 2003.

- [Bor11] B Bornschein. “Between Fusion and Cosmology-The Future of the Tritium Laboratory Karlsruhe”. In: *Fusion Science and Technology* 60.3 (2011), pp. 1088–1091.
- [BW36] G. Breit and E. Wigner. “Capture of Slow Neutrons”. In: *Phys. Rev.* 49.7 (Apr. 1936), pp. 519–531. URL: <http://link.aps.org/doi/10.1103/PhysRev.49.519>.
- [Cap+16] F. Capozzi et al. “Neutrino masses and mixings: Status of known and unknown  $3\nu$  parameters”. In: *Nuclear Physics B* (2016), ISSN: 0550-3213. DOI: [doi:10.1016/j.nuclphysb.2016.02.016](https://doi.org/10.1016/j.nuclphysb.2016.02.016). URL: <http://www.sciencedirect.com/science/article/pii/S0550321316000602>.
- [Cha14] James Chadwick. “Intensitätsverteilung im magnetischen Spectrum der *beta*-Strahlen von radium B+ C”. In: *Verhandl. Dtsc. Phys. Ges.* 16 (1914), pp. 383–.
- [Cha32] James Chadwick. “Possible existence of a neutron”. In: *Nature* 129.3252 (1932), pp. 312–.
- [Cle+98] Bruce T. Cleveland et al. “Measurement of the Solar Electron Neutrino Flux with the Homestake Chlorine Detector”. In: *The Astrophysical Journal* 496.1 (1998), pp. 505–. ISSN: 0004-637X. URL: <http://stacks.iop.org/0004-637X/496/i=1/a=505>.
- [CN73] Thomas A Carlson and CW Nestor Jr. “Calculation of electron shake-off probabilities as the result of X-ray photoionization of the rare gases”. In: *Physical Review A* 8.6 (1973), pp. 2887–.
- [Cow+56] C.L. Cowan et al. “Detection of the free Neutrino: a Confirmation”. In: *Science*, vol. 124, no. 3212, pp. 103-104 (1956).
- [Dan+62] G. Danby et al. “Observation of High-Energy Neutrino Reactions and the Existence of Two Kinds of Neutrinos”. In: *Phys. Rev. Lett.* 9.1 (July 1962), pp. 36–44. URL: <http://link.aps.org/doi/10.1103/PhysRevLett.9.36>.
- [Del+16] Stefano Dell’Oro et al. “Neutrinoless double beta decay: 2015 review”. In: *arXiv preprint arXiv:1601.07512* (2016), pp. 5–.
- [Des+03] Richard D. Deslattes et al. “X-ray transition energies: new approach to a comprehensive evaluation”. In: *Rev. Mod. Phys.* 75.1 (Jan. 2003), pp. 35–99. URL: <http://link.aps.org/doi/10.1103/RevModPhys.75.35>.
- [DS90] Daniel J. Decman and Wolfgang Stoeffl. “Atomic electron binding energies of multiply charged krypton ions by internal-conversion-electron spectroscopy”. In: *Phys. Rev. Lett.* 64.23 (June 1990), pp. 2767–2770. URL: <http://link.aps.org/doi/10.1103/PhysRevLett.64.2767>.
- [Eno13] Sanshiro Enomoto. “Detector DAQ FPGA Upgrade for High-Rate Measurements (Internal presentation, KATRIN Collaboration Meeting)”. Mar. 12, 2013.
- [Fer34] E. Fermi. “Versuch einer Theorie der  $\beta$ -Strahlen. I”. In: *Zeitschrift für Physik* 88.3 (1934), pp. 161–177. ISSN: 0044-3328. URL: <http://dx.doi.org/10.1007/BF01351864>.
- [FP12] J A Formaggio and the Project 8 Collaboration. “Measuring Neutrino Masses Using Radio-Frequency Techniques”. In: *Journal of Physics: Conference Series* 375.4 (2012), pp. 042005–. ISSN: 1742-6596. URL: <http://stacks.iop.org/1742-6596/375/i=4/a=042005>.

- [Fuk+01] S Fukuda et al. “Constraints on neutrino oscillations using 1258 days of Super-Kamiokande solar neutrino data”. In: *Physical Review Letters* 86.25 (2001), pp. 5656–.
- [Gas+14] L Gastaldo et al. “The Electron Capture  $^{163}\text{Ho}$  Experiment ECHo”. In: *Journal of low temperature physics* 176.5-6 (2014), pp. 876–884. ISSN: 0022-2291.
- [GP12] Andrea Giuliani and Alfredo Poves. “Neutrinoless double-beta decay”. In: *Advances in High Energy Physics* 2012 (2012), ISSN: 1687-7357.
- [GP69] V. Gribov and B. Pontecorvo. “Neutrino astronomy and lepton charge”. In: *Physics Letters B* 28.7 (1969), pp. 493–496. ISSN: 0370-2693. URL: <http://www.sciencedirect.com/science/article/pii/0370269369905255>.
- [Gro15] Stefan Groh. “Modeling of the response function and measurement of transmission properties of the KATRIN experiment”. PhD thesis. Karlsruhe Institute of Technology, IEKP, 2015.
- [Ham+11] Jan Hamann et al. “Sterile neutrinos with eV masses in cosmology—how disfavoured exactly?” In: *Journal of Cosmology and Astroparticle Physics* 2011.09 (2011), pp. 034–. ISSN: 1475-7516.
- [Ham+99] Wolfgang Hampel et al. “GALLEX solar neutrino observations: Results for GALLEX IV”. In: *Physics Letters B* 447.1 (1999), pp. 127–133. ISSN: 0370-2693.
- [Har15] Fabian Harms. “Characterization and Minimization of Background Processes in the KATRIN Main Spectrometer”. PhD thesis. Karlsruhe Institute of Technology, Oct. 23, 2015.
- [Höt12] Markus Hötzel. “Simulation and analysis of source-related effects for KATRIN”. PhD thesis. Karlsruhe Institute of Technology, 2012.
- [Hua10] Jiayu Hua. “Simulation des Kryptonmodus der Tritiumquelle WGTS im KATRIN Experiment”. MA thesis. KIT, 2010.
- [Jam04] Fred James. *The interpretation of errors*. Cern, 2004,
- [Jan15] Alexander Jansen. “The Cryogenic Pumping Section of the KATRIN Experiment—Design Studies and Experiments for the Commissioning”. PhD thesis. Karlsruhe Institute of Technology, 2015,
- [KAT04] Collaboration KATRIN. “KATRIN design report 2004”. In: *FZKA report* 7090 (2004). URL: <http://inspirehep.net/record/680949/files/FZKA7090.pdf>.
- [Ker04] Norbert Kernert. *Production of Kr-83m for the KATRIN experiment*. Tech. rep. Forschungszentrum Karlsruhe, June 14, 2004.
- [Kle14] Marco Kleesiek. “A Data-Analysis and Sensitivity-Optimization Framework for the KATRIN Experiment”. PhD thesis. Karlsruhe Institute of Technology, 2014. URL: <http://digbib.ubka.uni-karlsruhe.de/volltexte/documents/3232293>.
- [Kod+01] K. Kodama et al. “Observation of tau neutrino interactions”. In: *Physics Letters B* 504.3 (Apr. 2001), pp. 218–224. ISSN: 0370-2693. URL: <http://www.sciencedirect.com/science/article/pii/S0370269301003070>.
- [KS10] Denize Kalempa and Felix Sharipov. *Separation phenomenon in the Windowless Gaseous Tritium Source of KATRIN experiment. Ternary mixtures*. Tech. rep. Tech. rep., Depto de Física, UFPR, 2010. URL: <http://fisica.ufpr.br/sharipov/KATRIN/report5.pdf>.

- [Kuc16] L. Kuckert. “The Windowless Gaseous Tritium Source of KATRIN - Characterisation of gas dynamical and plasma properties (in preperation)”. PhD thesis. Karlsruhe Institute of Technology, 2016.
- [LG06] The ALEPH CollaborationThe DELPHI CollaborationThe L3 CollaborationThe OPAL CollaborationThe SLD CollaborationThe LEP Electroweak Working GroupThe SLD LEP Electroweak and Heavy Flavour Groups. “Precision electroweak measurements on the Z resonance”. In: *Physics Reports* 427.5-6 (May 2006), pp. 257–454. ISSN: 0370-1573. URL: <http://www.sciencedirect.com/science/article/pii/S0370157305005119>.
- [Liu73] JW Liu. “Total Inelastic Cross Section for Collisions of H 2 with Fast Charged Particles”. In: *Physical Review A* 7.1 (1973), pp. 103–.
- [Lob+01] VM Lobashev et al. “Direct search for neutrino mass and anomaly in the tritium beta-spectrum: Status of “Troitsk neutrino mass” experiment”. In: *Nuclear Physics B-Proceedings Supplements* 91.1 (2001), pp. 280–286. ISSN: 0920-5632.
- [LUX+14] LUX LUX Collaboration et al. “First Results from the LUX Dark Matter Experiment at the Sanford Underground Research Facility”. In: *Phys. Rev. Lett.* 112.9 (Mar. 2014), pp. 091303–. URL: <http://link.aps.org/doi/10.1103/PhysRevLett.112.091303>.
- [McC15] E.A. McCutchan. “Nuclear Data Sheets for A = 83”. In: *Nuclear Data Sheets* 125 (Mar. 2015), pp. 201–394. ISSN: 0090-3752. URL: <http://www.sciencedirect.com/science/article/pii/S0090375215000034>.
- [MS86] S. P. Mikheyev and A. Yu. Smirnov. “Resonant amplification of  $\nu$  oscillations in matter and solar-neutrino spectroscopy”. In: *Il Nuovo Cimento C* 9.1 (1986), pp. 17–26. ISSN: 0390-5551. URL: <http://dx.doi.org/10.1007/BF02508049>.
- [Nob15] Nobel Media AB 2014 Nobelprize.org. *The 2015 Nobel Prize in Physics - Press Release*. 2015. URL: [http://www.nobelprize.org/nobel\\_prizes/physics/laureates/2015/press.html](http://www.nobelprize.org/nobel_prizes/physics/laureates/2015/press.html).
- [OG14] Keith A Olive and Particle Data Group. “Review of particle physics”. In: *Chinese Physics C* 38.9 (2014), pp. 090001–. ISSN: 1674-1137.
- [Ost08] Beatrix Ostrick. “Eine kondensierte  $^{83\text{m}}\text{Kr}$ -Kalibrationsquelle für das KATRIN-Experiment”. PhD thesis. Karlsruhe Institute of Technology, 2008.
- [OW08] EW Otten and Ch Weinheimer. “Neutrino mass limit from tritium  $\beta$  decay”. In: *Reports on Progress in Physics* 71.8 (2008), p. 086201. URL: <http://iopscience.iop.org/article/10.1088/0034-4885/71/8/086201/pdf>.
- [Pau30] Wolfgang Pauli. “Offener Brief an die Gruppe der Radioaktiven bei der Gauvereins-Tagung zu Tübingen”. In: *datiert* 4 (1930), pp. 1316–1317.
- [Per03] Donald H Perkins. *Particle astrophysics*. 10. Oxford University Press, USA, 2003,
- [Pfe09] Vacuum GmbH Pfeiffer. *Vacuum Technology Know How*. Mar. 2009.
- [Pic+92] A. Picard et al. “Precision measurement of the conversion electron spectrum of  $^{83\text{m}}\text{Kr}$  with a solenoid retarding spectrometer”. In: *Zeitschrift für Physik A Hadrons and Nuclei* 342.1 (1992), pp. 71–78. ISSN: 0939-7922. URL: <http://dx.doi.org/10.1007/BF01294491>.

- [Pla15] Collaboration Planck. “Planck 2015 results. XIII. Cosmological parameters”. In: *arXiv preprint arXiv:1502.01589* (2015),
- [RK88] R G H Robertson and D A Knapp. “Direct Measurements of Neutrino Mass”. In: *Annu. Rev. Nucl. Part. Sci.* 38.1 (Dec. 1988), pp. 185–215. ISSN: 0163-8998. DOI: [10.1146/annurev.ns.38.120188.001153](https://doi.org/10.1146/annurev.ns.38.120188.001153). URL: <http://dx.doi.org/10.1146/annurev.ns.38.120188.001153>.
- [Rob+91] R. G. H. Robertson et al. “Limit on  $\bar{\nu}_e$  mass from observation of the  $\beta$  decay of molecular tritium”. In: *Phys. Rev. Lett.* 67.8 (Aug. 1991), pp. 957–960. URL: <http://link.aps.org/doi/10.1103/PhysRevLett.67.957>.
- [Röl15] Marco Röllig. *Tritium analytics by beta induced X-ray spectrometry*. 2015.
- [Rös+78] F Rösler et al. “Internal conversion coefficients for all atomic shells”. In: *Atomic Data and Nuclear Data Tables* 21.2 (1978), pp. 91–289.
- [Sch14] Johannes Simon Schwarz. *The Detector System of the KATRIN Experiment-Implementation and First Measurements with the Spectrometer*. 2014.
- [SD95] Wolfgang Stoeffl and Daniel J Decman. “Anomalous structure in the beta decay of gaseous molecular tritium”. In: *Physical review letters* 75.18 (1995), p. 3237. URL: <http://journals.aps.org/prl/pdf/10.1103/PhysRevLett.75.3237>.
- [Sev79] Kenneth D. Sevier. “Atomic electron binding energies”. In: *Atomic Data and Nuclear Data Tables* 24.4 (1979), pp. 323–371. ISSN: 0092-640X. URL: <http://www.sciencedirect.com/science/article/pii/0092640X79900123>.
- [Sha03] Felix Sharipov. “Numerical Calculation of the Tritium Flow through the KATRIN Beam Line”. In: *KATRIN internal Document* (2003),
- [SNO+02] SNO et al. “Direct Evidence for Neutrino Flavor Transformation from Neutral-Current Interactions in the Sudbury Neutrino Observatory”. In: *Phys. Rev. Lett.* 89.1 (June 2002), pp. 011301–. URL: <http://link.aps.org/doi/10.1103/PhysRevLett.89.011301>.
- [Stu16] Michael Sturm. “Internal conversation.” 2016.
- [Suz95] Yoichiro Suzuki. “Kamiokande solar neutrino results”. In: *Nuclear Physics B-Proceedings Supplements* 38.1 (1995), pp. 54–59. ISSN: 0920-5632.
- [Thü07] Thomas Thümmeler. “Präzisionsüberwachung und Kalibration der Hochspannung für das KATRIN-Experiment”. PhD thesis. 2007,
- [Vén+14] D Vénos et al. “Gaseous source of  $^{83m}\text{Kr}$  conversion electrons for the neutrino experiment KATRIN”. In: *Journal of Instrumentation* 9.12 (2014), P12010–. ISSN: 1748-0221. URL: <http://stacks.iop.org/1748-0221/9/i=12/a=P12010>.
- [Vog06] Petr Vogel. “Neutrinoless double beta decay”. In: *arXiv preprint hep-ph/0611243* (2006),
- [War+91] D. L. Wark et al. “Correspondence of electron spectra from photoionization and nuclear internal conversion”. In: *Phys. Rev. Lett.* 67.17 (Oct. 1991), pp. 2291–2294. URL: <http://link.aps.org/doi/10.1103/PhysRevLett.67.2291>.
- [Wei03] Ch. Weinheimer. *Massive Neutrinos*. Ed. by G. Altarelli and K. Winter. Springer Heidelberg, 2003. Chap. Laboratory limits on neutrino masses, pp. 25–52. ISBN: 3-540-40328-0.
- [Wik06] Wikimedia. *Standard Model of Elementary Particles* visited on 29.03.2016. 2006. URL: [https://commons.wikimedia.org/wiki/File:Standard\\_Model\\_of\\_Elementary\\_Particles.svg](https://commons.wikimedia.org/wiki/File:Standard_Model_of_Elementary_Particles.svg).

- [Wil+87] John Franklin Wilkerson et al. “Limit on  $\nu^- e$  Mass from Free-Molecular-Tritium Beta Decay”. In: *Physical review letters* 58.20 (1987), p. 2023. URL: <http://journals.aps.org/prl/pdf/10.1103/PhysRevLett.58.2023>.
- [Wil+88] JF Wilkerson et al. “Limit on anti  $\nu_e$  mass from free molecular tritium beta decay”. In: (1988).
- [Wil03] J.F. Wilkerson. *Physics motivation for using a Windowless Gaseous Kr Source*. Internal presentation. KATRIN 6. TB, Mainz, July 8, 2003.
- [Wu01] S-C Wu. “Nuclear data sheets for A= 83\*”. In: *Nuclear Data Sheets* 92.4 (2001), pp. 893–1028.
- [WW30] Victor Weisskopf and Eugene Wigner. “Berechnung der natürlichen Linienbreite auf Grund der Diracschen Lichttheorie”. In: *Zeitschrift für Physik* 63.1-2 (1930), pp. 54–73. URL: <http://link.springer.com/content/pdf/10.1007/BF01336768.pdf>.
- [Zub11] Kai Zuber. *Neutrino physics*. CRC press, 2011,

# A. Appendix

## A.1. Shape Deformation of Lorentzian Lines with the WGTS Plasma Potential

This section aims to conclude the discussion in section 4.6.2. Without the linear approximation and the restriction to the measurement at the mean, the full expectancy value of the potential reads

$$\langle V \rangle_i \simeq \frac{\hat{\Gamma}}{2} \tan \left( \frac{\int_z dz \Omega(z) N^K(z) p_i(z) \arctan \left[ \frac{2}{\hat{\Gamma}} (qV(z) + q\Delta U) \right]}{\int_z dz \Omega(z) N^K(z) p_i(z)} \right) - q\Delta U. \quad (\text{A.1})$$

Here  $q\Delta U$  is the retarding voltage measured relative to the line mean.

Since the arc tangent has not been neglected, the effective line width  $\hat{\Gamma}$  can not be cancelled. Figure A.1 shows the measurable mean of the potential as function of  $q\Delta U$  for different effective line widths in the range of 0.1 – 2.3 eV. The intrinsic line width of  $L_3$   $\Gamma = 1.19$  eV is painted in red. A comparable potential to the 110 K plasma potential simulation has been included in the calculation. It can be observed, that the maximum deviation of observable means is in the range of 0.5 mV for the smallest effective width of 0.1 eV. For the intrinsic line width, it is below 0.1 mV. Naturally the effective line width in KATRIN krypton-83m mode  $L_3$  measurements will be larger and the difference in means will be even smaller.

## A.2. Towards an Optimised Measurement Time Distribution in Krypton-83m Mode

A major outcome of this work is the finding, that the easiest way to gather information on the plasma potential is to measure the relative means of the unscattered and one time scattered step. In figure A.2 the plasma potential induced relative rate deviation is shown

$$\frac{\dot{N}(V) - \dot{N}(V = 0)}{\dot{N}(V = 0)}. \quad (\text{A.2})$$

Accordingly, the deviations at the one time scattered step are less than 1/6 than the deviations at the unscattered step. This implies, that a much larger amount (presumably 6 times as much) of measurement time has to be devoted to the scattered step to get an optimal sensitivity. However, this has been tested and only minor improvements could be found.

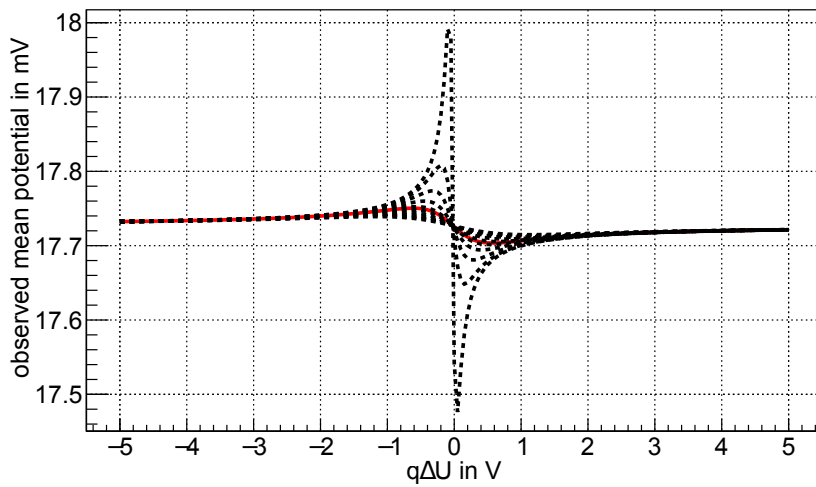


Figure A.1.: Shape deformation of Lorentzian lines with different widths  $\Gamma$  in dependency of the retarding potential measured relative to the mean: The calculation includes a plasma potential simulation, which shifts the overall line position of about 17.73 mV.

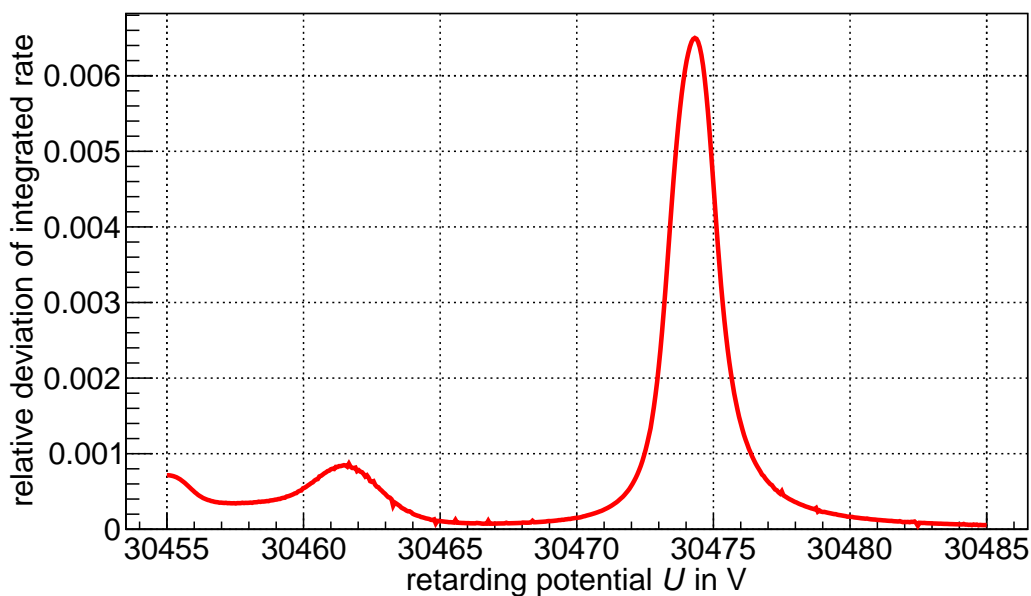


Figure A.2.: Plasma potential induced deviation of integrated  $L_3$  rates: Three peaks are visible at the unscattered line position, the scattered line position and the shake off line. The small cracks are numerical artefacts.

At high krypton rates of at least 100 kcps the sensitivity on the line shape deformation can get relevant in a feasible measurement time, according to the sensitivity plots shown in chapter 4. As it is obvious from figure A.1, the maximum information on the plasma potential can be found in a 1 V interval around the line mean. Consequently this should be a region of long measurements.



# Danksagung

Zum Schluss möchte ich mich bei allen bedanken, die meine Arbeit im letzten Jahr ermöglicht und mich in dieser Zeit und darüber hinaus unterstützt haben. Im Besonderen sind das:

- Prof. GUIDO DREXLIN und Dr. KATHRIN VALERIUS, die mir ein entspanntes und selbstständiges Arbeiten in der KATRIN Kollaboration ermöglicht haben. Besonders danken möchte ich KATHRIN VALERIUS, die mit ihrer kollegialen und motivierenden Art stets die Fäden zusammen hält und außerdem dafür sorgt, dass auch neben der Arbeit alles bei uns läuft.
- Prof. ULRICH HUSEMANN, für die Übernahme des Korreferats.
- Dr. MARCO KLEESIEK, der mich in SSC und KaFit eingearbeitet und bei allen möglichen numerischen Problemen unterstützt hat. Außerdem dafür, dass er mir jederzeit für Diskussionen zur Verfügung stand.
- HENDRIK SEITZ-MOSKALIUK, der stets kompetente Antworten auf meine Fragen fand und viele Teile der Arbeit korrigiert hat. Außerdem bei meinem Zimmerkollegen ANTON HUBER stellvertretend für die ganze KATRIN Gruppe, für das tolle Arbeitsklima am Institut.
- CARSTEN RÖTTELE, der in der Schreibphase dafür gesorgt hat, dass ich an Abenden und Wochenenden nicht alleine am Institut sein musste.
- KLAUS MEHRET, wegen dem ich mich jeden Tag aufs Neue auf halb 12 gefreut habe. Danke auch für die zahllosen Kaffees, die du mir ausgegeben hast.

Gesondert bedanken möchte ich mich beim PHYSIKER THEATER, für den Respekt und die Offenheit, die mir dort von Anfang an begegnet sind. Ohne euch wäre mein Studium nicht halb so schön gewesen. Ein besonderer Dank gilt Malin Reller, meinen Schauspielern und allen, die mich bei Astoria unterstützt haben. Eure Mitarbeit in dieser Zeit hat bei mir wertvollste Erinnerungen und Erfahrungen hinterlassen und mir den nötigen Ausgleich zur Arbeit gegeben. Ihr seid die Besten!

Mein größter Dank gilt jedoch meiner Familie und meiner Freundin BETTINA. Danke für die zahllosen Mahlzeiten, die du mir (nicht nur) in der stressigen Schreibphase zubereitet hast. Danke für deinen bewundernswerten Altruismus. Ich danke meiner Mutter LYDIA, meinem Vater KLAUS und meinem Bruder RAINHARD für ihre Unterstützung.